Measurement of $D^{*\pm}$ Production at Low Q^2 with the Beam-Pipe Calorimeter of ZEUS at HERA

Dissertation

zur

Erlangung des Doktorgrades (Dr. rer. nat.)

der

Mathematisch-Naturwissenschaftlichen Fakultät

der

Rheinischen Friedrich-Wilhelms-Universität Bonn

vorgelegt von

Peter Irrgang

aus

Bonn

Bonn 2004

Measurement of $D^{*\pm}$ Production at Low Q^2 with the Beam-Pipe Calorimeter of ZEUS at HERA

The production of D^* mesons in deep-inelastic ep-scattering has been studied using the ZEUS detector at HERA. The total D^* production cross-section and the differential cross-sections as functions of Q^2, y, $p_t(D^*)$ and $\eta(D^*)$ have been measured at low Q^2. The data sample used was collected during the period 1998–2000 and amounts to an integrated luminosity of 82.2 pb^{-1}.

The low Q^2 region could be reached using the beam-pipe calorimeter which measures the scattered electron at very small angles. Therefore special emphasis was put on the calibration of the BPC in order to reconstruct events in the kinematic range $0.05 < Q^2 < 0.7\,\mathrm{GeV}^2$ and $0.02 < y < 0.85$. The D^* mesons have been identified via the decay into lighter mesons $D^{*+} \to K^-\pi^+\pi^+$ and the charged conjugated decay in the kinematic region $1.5 < p_t(D^*) < 9.0\,\mathrm{GeV}$ and $-1.5 < \eta(D^*) < 1.5$.

The measured cross-sections are in agreement with the predictions from perturbative QCD calculations. Previous ZEUS D^* production measurements could be extended towards lower values of Q^2 in agreement with the corresponding perturbative QCD predictions.

Diese Dissertation wurde von der Mathematisch-Naturwissenschaftlichen Fakultät der Universität Bonn angenommen und ist auf dem Hochschulschriftenserver der ULB Bonn http://hss.ulb.uni-bonn.de/diss_online elektronisch publiziert.

Tag der Promotion: 07. 12. 2004

Erstgutachter:	Prof. I. Brock
Zweitgutachter:	Prof. W. Schwille

"My dear fellow," said Sherlock Holmes as we sat on either side of the fire in his lodgings at Baker Street, "Life is infinitely stranger than anything which the mind of man could invent. We would not dare to conceive the things which are really mere commonplace of existence. If we could fly out of that window hand in hand, hover over this great city, gently remove the roofs, and peep in at the queer things which are going on, the strange coincidences, the plannings, the cross-purposes, the wonderful chains of events, working through generations, and leading to most *outré* results, it would make all fiction with its unconventionalities and forseen conclusions most stale and unprofitable."

"A Case of Identity", Sir Arthur Conan Doyle

Contents

Chapter 1

Introduction

More than 2500 years ago Greek philosophers introduced and developed the basic ideas of the concepts of modern science. Pythagoras – impressed from his long travel through the orient – was the first who used numbers and the relations between them to describe the world. In his lore of the harmonics he introduced the term "cosmos" and tried to explain the nature of music using some basic relations and symmetries.

Two of his famous successors, Leukippos and his scholar Demokritos, continued to build the philosophical basis of science. Their important contributions to the ancient philosophical discussion were the principle of causality and the idea of an empty space, extended over the whole cosmos, which is filled with indivisible entities, the atoms. From their point of view the attributes of all existing things are given by the shape, position, order and dimension of these atoms.

Unlike the models of modern physics, the ancient Greek philosophers did not claim to be able to predict physics phenomena from their philosophical lore. This revolutionary idea was reserved for medieval geniuses such as Galileo or Kepler. Thus, it would take more than 2000 years before the pure philosophical ideas were identified in nature as basic principles and become scientific models.

The technology to pursue scientific investigations only became avaliable in the past centuries. In the seventeenth century, the inventions of the microscope and of the telescope allowed man to observe objects invisibly small or very far away. Those observations revealed a first glance of the structure of matter as well as our solar system. This scientific breakthrough gave rise to a philosophical and political change in the occidental part of the world that was the major cause of the downfall of many of the church's doctrines. However, the scale of the fundamental building blocks is much smaller than that which was observed by microscopes, and is still invisible to most modern light microscopes.

First indications that matter can be decomposed into a set of basic elements came therefore not from observations with the microscope but from chemistry. The composition hypothesis greatly simplified the classification of chemical elements and the understanding of chemical reactions. Finally Mendeleev introduced the periodic system in 1865, albeit with some holes for predicted but so far undiscovered elements

which were eventually filled. In 1910 Geiger and Marsden performed an experiment where a beam of "α"-particles – later identified as nuclei of helium atoms – was scattered off a gold foil target. The α-particles were scattered sometimes almost backwards which led to Rutherford's interpretation that the mass of gold atoms is concentrated in a compact object at its centre. Bohr developed an atomic model on this basis for hydrogen and later on, after the discovery of the neutron, Chadwick extended the model to heavier nuclei.

The experimental method of Geiger and Marsden, the scattering of a beam of probing particles off a target to be examined laid the foundation of all modern high energy scattering experiments. The spatial resolution of scattering experiments is defined by the wavelength of the probing particle and is inversely proportional to the momentum of the probe in the centre of mass of the probe-target system. It has increased dramatically during the past decades.

In the 1950s Hofstadter conducted an experiment to measure the charge distribution in the proton the results of which suggested a substructure. A whole series of electron-proton scattering experiments at SLAC in 1969 revealed that protons were composed of smaller objects, entities named partons. Later the partons were identified as the "quarks" which had been introduced by Murray Gell-Mann and Yuval Ne'eman in 1961 as fundamental objects. They were the first who used the quarks in a model to classify all hadrons observed in geometrical patterns given by the (approximate) symmetry properties of an $SU(3)_f$ group.

The quark model was strongly supported by the discovery of the Ω^- particle which was predicted by the model but had not discovered at that time. Originally three light quark flavour eigenstates named up (u), down (d), strange (s) were sufficient to form the known hadrons. With the later discovery of three much heavier additional quark flavours – charm (c), bottom (b), top (t) – the group had to be extended. The hadrons are subdivided into mesons and baryons. Mesons are formed by $q\bar{q}$ (with one quark in the "flavour" eigenstate q and one in the eigenstate $\bar{q}$). The D^{*+} (D^{*-}) meson, whose production in electron-proton collisions is measured in this thesis, consists of $c\bar{d}$ ($\bar{c}d$) quark–anti-quark pairs. The baryons are formed from a combination of three quarks flavours qqq, e.g. the proton has a quark content of uud.

However, the $SU(3)_f$ symmetry of the flavour model is not able to describe the interactions between the quarks as it is only a phenomenological ordering scheme.

The theory of Quantum Chromodynamics (QCD) allows the forces between quarks to be predicted. In this theory the quarks correspond to a fundamental three-dimensional representation of $SU(3)$, and each quark flavour appears in one of three colours. This $SU(3)_c$ is an exact symmetry group with 8 generators associated to the 8 "gluons". The gluons mediate the strong force between the quarks and have spin 1. Due to the non-Abelian property of the $SU(3)_c$ symmetry group the gluons can interact with themselves and the effective coupling constant of the strong force, α_s, decreases with increasing energy scale μ of the reaction. Using the Heisenberg uncertainty principle the scale variable can be interpreted as resolution, where a large

scale variable indicates a better resolution than a small one. There are some remarkable features of QCD such as asymptotic freedom, $\lim_{\mu\to\infty} \alpha_s(\mu) \to 0$, which indicates that the strong force gets weak at very high scales. Another is the quark confinement, which means that only colour neutral objects are observed as free particles. Although the colour symmetry is exact, the calculation of QCD observables, such as the cross-sections, has to be done using a perturbation series in $\alpha_s(\mu)$ which is valid for μ larger than the QCD cut-off parameter $\Lambda_{QCD} = (100 \ldots 400)\,\mathrm{MeV}$. But at scales $\mu \approx \Lambda_{QCD}$ the effective coupling constant becomes large and the approximation breaks down.

The topic of this thesis is the measurement of $D^{*\pm}$ meson production in the transition region between photoproduction (PhP) and deep-inelastic *ep*-scattering (DIS), where the calculations are difficult. PhP reactions are characterised by the exchange of a quasi-real photon between the colliding electron and the proton, whereas in DIS reactions a virtual – i.e. off shell – photon is exchanged. In the kinematic region of interest for this thesis the scale μ, used in the perturbative QCD calculation, does not only depend on the momentum carried by the photon but also on the charm quark mass and is of the same order as Λ_{QCD}. Therefore the results of this thesis allow the theoretical predictions which use the perturbative ansatz to be tested.

This thesis starts with a theoretical description of deep-inelastic scattering processes. An overview of the charm production mechanism and the formation of hadrons like the $D^{*\pm}$ meson by fragmentation is also given. Chapter 3 gives a brief overview of the Monte-Carlo generators and the theoretical calculations used in the physics simulation. The next, Chapter 4, contains an overview of the ZEUS detector. Chapter 5 is dedicated to a detailed description of the beam-pipe calorimeter (BPC), which allows the region of low four-momentum transferred squared, Q^2, to be accessed by the measurement of the energy and position of the scattered electron. The selection and the analysis of events containing $D^{*\pm}$ mesons is explained in Chapter 6. In the second part of the chapter the cross-sections are calculated. Finally, the results are compared with theoretical predictions and put in a larger context by using previous measurements in Chapter 7.

Chapter 2

Theoretical Overview

For the theoretical understanding of high-energy lepton-proton-scattering (the so-called *ep*-scattering) three out of the four fundamental forces of nature are relevant. These are the electromagnetic, weak and strong interactions. They are all believed to be accurately described by a quantum field theory possessing local gauge symmetries. Quantum Electrodynamics (QED) describes the electromagnetic interaction with the massless photon as the intermediary gauge boson. QED is unified with the weak interaction in the standard electroweak model. Along with the photon the heavy $W^{\pm}$ and Z particles are the gauge bosons of the electroweak interaction. In the 1970s quantum chromodynamics (QCD) was developed as the theory of strong interactions [1, 2], describing quark and gluon interactions. QCD is based on a non-Abelian local SU(3) colour symmetry. Each quark appears in one of three colour states. The strong force is mediated by massless gluons, which themselves carry colour. An overview of all particles and interactions of the standard model is tabulated in Table. 2.1. Gravitation is the fourth and the weakest fundamental interaction. It is not included in the standard model, because the description of gravitation by a quantum field theory is not yet possible.

This chapter gives a brief overview of the theory describing the physics of the analysis presented in this thesis. The first section explains the kinematics and cross-sections in deep-inelastic *ep*-scattering (DIS) and their interpretation in the framework of QCD. A short section on photoproduction (PhP) follows. The production mechanism of heavy quarks in DIS events, the subsequent fragmentation into hadrons and their hadronic decays are discussed in the second section. Further information can be found in textbooks, e.g. [3].

2.1 Deep-Inelastic Scattering at HERA

In the 1998–2000 data taking period the centre-of-mass system (CMS) energy of the *ep*-scattering process at HERA was 318 GeV with beam energies of $E_e = 27.6\,\text{GeV}$

	Electric Charge/units of e			
	0	-1	$+2/3$	$-1/3$
Generation	Fermions			
	Leptons		Quarks	
1st	ν_e	e	u	d
2nd	ν_μ	μ	c	s
3rd	ν_τ	τ	t	b

Bosons	
g	strong
γ	electromagnetic
W^+,W^-, Z	weak

Table 2.1: The elementary fermions, the fundamental forces that act on them and the corresponding mediator bosons. A further boson, the Higgs, is predicted by the Standard Model, but has not yet been found. The fermions are split into three "generations" with increasing masses.

for the electrons or positrons and $E_p = 920\,\mathrm{GeV}$ for the protons:

$$s = (k + P)^2 \approx 4E_eE_p \approx 318^2\,\mathrm{GeV}^2 \ ,$$

where k and P are the 4-vectors of the electron and the proton as presented in Fig. 2.1 for the two kinds of deep-inelastic scattering (DIS) events. The symbols of the 4-vectors of the incoming and outgoing particles are given in parentheses. A general lepton-nucleon scattering process is defined as a deep-inelastic scattering (DIS) event, if the scattered electron can enter the proton deeply and as a consequence the proton breaks apart. The proton remnants and the struck quark, which forms hadrons via a fragmentation process, define the hadronic system X. A necessary condition for the hit proton to break apart is that the fraction of energy transferred from the lepton to the proton, y, is sufficient, therefore y is considered as the "inelasticity".

As there is no difference between the scattering positron or electron in the context of this thesis[1], electrons and positrons will be denoted by "electrons" in the following.

Measuring the final state or the scattered electron of such deep-inelastic ep-scattering events allows the structure of the proton to be determined. Within the picture of the quark parton model, the proton consists of quarks and gluons. The highly-energetic incoming electron then probes the structure of the proton by coupling through the electroweak current to the charged partons inside the proton. In neutral current (NC) events, $e + p \rightarrow e + X$ sketched in Fig. 2.1, the exchanged

[1]The difference is relevant at high Q^2 for the NC and for the CC process.

boson is either a virtual photon, γ, or a Z boson. For charged current (CC) events, $e+p \to \nu_e + X$, the exchanged boson is a charged W boson, and the final state lepton is a neutrino, which escapes the detector undetected.

Only two variables are needed to fully determine the kinematics of DIS events. Usually two out of the following three are chosen:

$$\begin{aligned} Q^2 &= -q^2 = -(k-k')^2 \\ x &= \frac{Q^2}{2P\cdot q} \text{ and} \\ y &= \frac{q\cdot P}{k\cdot P} \end{aligned}$$

where Q^2, called "virtuality", is the negative squared four momentum transfer from the incoming electron to the proton. Q^2 gives the resolution power of the photon probing the proton, since the photon wavelength is determined by $\lambda = 1/|q| = 1/\sqrt{Q^2}$. This variable gives the "hardness" of the reaction. The maximum possible value of Q is s, therefore it is important to achieve a high CMS energy in order to get a high resolution. In the quark parton model, x can be interpreted as the momentum fraction of the proton carried by the struck parton and is called Bjorken x. It is convenient to boost to the so-called infinite momentum frame, where the proton has very high longitudinal momentum. The masses of the proton and the partons can be neglected and x can be shown to be the momentum fraction of the scattered parton. Thus it ranges from 0 to 1. The inelasticity, y, also ranges from 0 to 1.

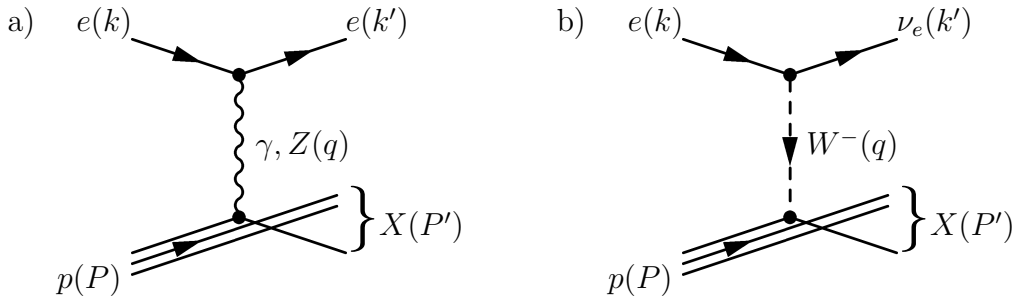

Figure 2.1: Feynman diagrams of the a) neutral current (NC) and b) charged current (CC) DIS process.

Neglecting the electron mass, m_e, the three variables are related to each other by

$$Q^2 = (s - m_p^2)\, xy \;\approx\; sxy \;, \tag{2.1}$$

where the approximation is applicable for $s \gg m_p^2$. The square of the invariant mass of the hadronic final state system X is given by

$$\begin{aligned} W^2 &= (s-m_p^2)\, y - Q^2 + m_p^2 \;\approx\; sy - Q^2, \\ &= Q^2(\frac{1}{x} - 1) + m_p^2 \;, \end{aligned}$$

From Eqn. 2.1 we see that for a DIS event with low Q^2 the product $x \cdot y$ has to be very small. For the analysis presented in this thesis, with an inelasticity range of $0.02 < y < 0.85$, this implies also a very low x range of $10^{-7} < x < 10^{-3}$.

Variable Reconstruction at low Q^2

In this analysis the energy E'_e and the angle θ w.r.t. the beam-axis of the scattered electron are used to reconstruct the event variables. The energy and the angle are accessible with high precision in the Q^2 region of interested. Q^2 and y can be calculated using the following equations ("Electron method"):

$$Q^2 = 2E_e E'_e(1 - \cos\theta) \tag{2.2}$$

$$y = 1 - \frac{E'_e}{2E_e}(1 + \cos\theta) \tag{2.3}$$

There are some other methods to reconstruct the event variables by using a different pair of independent observables. The Jacquet-Blondel method uses energy and angle of the hadronic system whereas the Double Angle method takes the angles of the scattered electron and the hadronic system.

2.1.1 DIS Cross-Sections

The main subject of this thesis is the measurement of the cross-section for heavy quark production at low Q^2 in neutral current events. Hence the following discussions will focus on neutral current events only. The theoretical description of the cross-section for deep-inelastic scattering events consists of a leptonic and a hadronic part

$$d\sigma \sim L_{\mu\nu} \cdot W_{\mu\nu} \tag{2.4}$$

The tensor $L_{\mu\nu}$, called the leptonic tensor, describes the interaction of the electron with the exchanged boson. $L_{\mu\nu}$ is calculable via electroweak theory. For $Q^2 \ll M_Z^2$ photon exchange dominates and the leptonic tensor is described only by QED. If the energy rises, $Q^2 \sim M_Z^2$, the contribution from Z boson exchange must be taken into account. The interaction of the exchanged boson with the proton is described by the so called hadronic tensor $W_{\mu\nu}$. This tensor is not fully calculable but it can be parametrised in various ways. Assuming Lorentz invariance and current conservation, the double differential Born cross-section of DIS events may be expressed in terms of structure functions F_1, F_2 and F_3 of the proton

$$\left(\frac{d^2\sigma^{\mathrm{NC}}(e^{\pm}p)}{dxdQ^2}\right)_{\mathrm{Born}} = \frac{4\pi\alpha^2}{xQ^4}\{y^2 x F_1^{\mathrm{NC}}(x,Q^2) + (1-y)F_2^{\mathrm{NC}}(x,Q^2) \mp \left(y - \frac{y^2}{2}\right) x F_3^{\mathrm{NC}}(x,Q^2)\} \tag{2.5}$$

where α is the electromagnetic coupling constant.

The structure functions express the non-calculable part of the hadronic tensor. The structure function F_3^{NC} represents the parity-violating contribution to the differential cross-section due to Z exchange, and thus only becomes noticeable at very high Q^2. For the analysis, which is the subject of this thesis, the important regime is $Q^2 \lesssim 1\,\mathrm{GeV} \ll M_Z^2$. Hence in the following discussions only γ^* exchange is considered. The structure function F_1 is related to F_2 and the longitudinal proton structure function F_L by the relation $F_L = F_2 - 2xF_1$. The contribution of F_L to the cross-section is small, and only becomes significant at high y. The structure functions in Eqn. 2.5 are defined with respect to the Born cross-section, thus no electroweak radiative effects are taken into account.

2.1.2 The Naïve Quark Parton Model

The naïve quark parton model describes the proton as consisting of point-like non-interacting constituents, the quarks. The deep-inelastic *ep*-scattering process is then simply the scattering off a point-like particle inside the proton. For large enough Q^2 the point-like constituents of the proton can be resolved. Consequently for even higher Q^2 the structure functions, which describe the photon-proton scattering process, should no longer depend on the length scale $\frac{1}{Q}$, characterising the size of the constituents of the proton. Therefore, in this model, the structure functions are expected to be independent of Q^2 because no further detailed structure can be resolved. Hence it follows that the structure functions only depend on one parameter, e.g. on x. This scaling behaviour of the structure functions was predicted by Bjorken, and was observed in DIS experiments at SLAC a short time later [4].

In the picture of the quark parton model, the structure function F_2 for photon exchange only can be simply expressed in terms of quark densities $f_a(x)$ in the proton,

$$F_2(x) = \sum_a e_a^2 x f_a(x) \tag{2.6}$$

where the index a runs over all quark flavours and e_a is the charge of quark a. The structure functions F_1 and F_2 are related by the Callan-Gross relation, $2xF_1(x) = F_2(x)$, because the quarks are point-like spin $\frac{1}{2}$ particles. Hence it follows that the longitudinal structure function $F_L = F_2 - 2xF_1$ is zero in the picture of the naïve quark parton model. Another prediction from the naïve quark parton model is that the integrated momentum fraction $\epsilon_q = \sum_a \int_0^1 x f_a(x) dx$ carried by all quarks inside the proton should be equal to unity. However measurements showed that only about 50% of the protons momentum is carried by the quarks. Hence the remaining 50% must be carried by electrically neutral particles; the gluons introduced by QCD.

2.1.3 Quantum Chromodynamics

The gluons are the mediating gauge bosons of the strong force. The strong interaction between quarks and gluons is described by QCD, a non-Abelian gauge theory based

on the $SU(3)$ colour symmetry group. Quarks carry colour, the charge of the strong interaction. They appear in one of the three colours, "red", "green" or "blue". Colour charge is exchanged between the quarks via gluons. Due to the non-Abelian structure of QCD, the gluons themselves carry colour (forming a colour octet) and therefore interact with each other. The coupling constant of the strong force, α_s, is scale-dependent[2]. Towards high Q^2, and hence small distances, the coupling decreases. The dependence on the scale is given by the renormalisation group equation. To leading order the strong coupling constant is given by

$$\alpha_s(Q^2) = \frac{12\pi}{(33 - 2N_f)\ln\left(\frac{Q^2}{\Lambda^2}\right)} \tag{2.7}$$

where N_f is the number of quark flavours. The parameter Λ describes the scale at which the coupling becomes large. For $Q^2 > \Lambda^2$, α_s decreases logarithmically. This means that due to the small coupling at high energies, the quarks inside the proton may be regarded as free at high Q^2 (asymptotic freedom). For low Q^2 , i.e. $Q^2 < \mathcal{O}(\Lambda^2)$, the coupling becomes large and a perturbative description is no longer valid. Due to the large coupling at low Q^2 , and hence at long distances, quarks cannot be observed as free particles but only as bound states in colourless hadrons. This behaviour is called confinement. Λ is not predicted by theory and so it must be determined by experiment. It is found to have a value of $(100 \ldots 400)\,\mathrm{MeV}$.

Since we have to take the gluon into account, the naïve quark parton model described in Section 2.1.2, which ignores any colour interactions, is incomplete. In addition to $q\gamma^* \to q$, processes like $q\gamma^* \to qg$ (QCD Compton scattering) and $g\gamma^* \to q\bar{q}$ (boson-gluon-fusion, BGF) also contribute to the cross-section for deep-inelastic ep-scattering. In the case of QCD Compton scattering, the quark radiates a gluon either before or after interacting with the virtual photon. If a gluon splits into a quark anti-quark pair and one of the quarks interacts with the virtual photon, the process is called boson-gluon-fusion. These two additional processes are shown schematically in Fig. 2.8. In terms of perturbative QCD, the QCD Compton and BGF processes are leading order (LO) α_s contributions to the deep-inelastic cross-section.

In the perturbative calculation of cross-sections divergences occur. The divergences can be interpreted in terms of virtual fluctuations, such as a gluon fluctuating into a $q\bar{q}$ or gg pair. The divergences can be absorbed into changes of the strong coupling constant α_s. Therefore a cut-off parameter, μ_R, is introduced and all fluctuations that occur at time scales $t < \frac{1}{\mu_R}$ are absorbed into $\alpha_s(\mu_R)$.

2.1.4 The Factorisation Theorem

Perturbative QCD permits the calculation of the cross-sections for scattering processes like $q\gamma^* \to q$, $q\gamma^* \to qg$ or $g\gamma^* \to q\bar{q}$ at high Q^2 (hard scattering processes)

[2]The electromagnetic coupling constant is also scale dependent, but to a lesser extent.

because α_s becomes small. For calculations of ep-scattering processes, the distributions of the quarks and gluons in the proton must be known. These parton densities are not calculable in perturbative QCD since α_s is large (confinement). The "factorisation theorem" defines the structure functions as a convolution of the hard scattering process, $\hat{F}_i^a$, calculable in perturbative QCD, with the parton densities $f_a(x)$ inside the proton [5]. The structure functions F_i of the proton may be written as follows:

$$F_i(x,Q^2) = \sum_a f_a(x,\mu_F) \otimes \hat{F}_i^a\left(x, \frac{Q}{\mu_F}, \alpha_s(\mu_R)\right) \tag{2.8}$$

where the sum runs over gluons and all quark and anti-quark flavours. The factorisation of the structure functions requires the introduction of the factorisation scale μ_F. It divides the soft physics, namely the parton densities, from the hard physics, which is calculable in perturbative QCD. The partonic structure function $\hat{F}_i^a$ describes the hard scattering process between the virtual photon and the parton. Consequently both quantities, $f_a(x,\mu_F)$ and $\hat{F}_i^a(x, \frac{Q}{\mu_F}, \Lambda_s(\mu_R))$, depend on the factorisation scale μ_F. The measurable quantities must be independent of any arbitrary scale introduced by theory. In principle the factorisation scale μ_F and the renormalisation scale μ_R can take any values and one straightforward and common choice is to set $\mu_F = \mu_R = Q = \mu$.

Different schemes exist to define the parton densities and the factorisation and renormalisation scale μ. Some schemes are used frequently, like the minimal subtraction scheme (MS, in the following denoted with "M", as e.g. in CTEQ5M), the deep-inelastic scattering scheme (DIS, labelled with "D") and the fixed flavour number schemes for $N = 3$ and $N = 4$ (FFN3 and FFN4, labelled with "f3" and "f4" respectively) which will be used later in the the NLO calculations. In the DIS scheme the corrections to all orders in α_s are absorbed into the parton density functions, such that the structure function F_2 is simply defined as $F_2(x,Q^2) = x\sum_a e_a^2 f_a(x,Q^2)$. In Section 2.1.2 the structure function F_2 was already expressed in terms of quark densities of the proton within the picture of the naïve quark parton model. In terms of QCD, Eqn. 2.6 is the lowest order, $\mathcal{O}(\alpha_s^0)$, calculation of the structure function F_2 using the factorisation theorem as in Eqn. 2.8.

2.1.5 DGLAP Evolution Equations

Although the initial parton densities cannot be calculated perturbatively, QCD predicts their evolution with Q^2 if the density at a certain initial $Q^2 = Q_0^2$ can be given. The evolution is described by a set of integro-differential equations known as the DGLAP evolution equations after Dokshitzer, Gribov, Lipatov, Altarelli and Parisi [6, 7, 8]. The evolution of the quark density is given by

$$\frac{dq_i(x,Q^2)}{d\ln(Q^2)} = \frac{\alpha_s(Q^2)}{2\pi}\int_x^1 \frac{dy}{y}\left(q_i(y,Q^2)P_{qq}\left(\frac{x}{y}\right) + g(y,Q^2)P_{qg}\left(\frac{x}{y}\right)\right) \tag{2.9}$$

and the evolution of the gluon density is given by

$$\frac{dg(x,Q^2)}{d\ln(Q^2)} = \frac{\alpha_s(Q^2)}{2\pi}\int_x^1 \frac{dy}{y}\left(q_i(y,Q^2)P_{gq}\left(\frac{x}{y}\right) + g(y,Q^2)P_{gg}\left(\frac{x}{y}\right)\right) \tag{2.10}$$

where i denotes the quark flavour, and the sum runs over all quark and anti-quark flavours. $P_{p^f p^i}$ are the splitting functions

$$P_{qq}(z) = \frac{4}{3}\frac{1+z^2}{1-z} \tag{2.11}$$

$$P_{gq}(z) = \frac{4}{3}\frac{1+(1-z)^2}{z} \tag{2.12}$$

$$P_{qg}(z) = \frac{1}{2}(z^2+(1-z)^2) = P_{gq}(1-z) \tag{2.13}$$

$$P_{gg}(z) = 6\left(\frac{1-z}{z} + \frac{z}{1-z} + z(1-z)\right) \tag{2.14}$$

They represent the probability of a quark to radiate a gluon or of a gluon to split into a quark–anti-quark pair. The different processes are shown schematically in Fig. 2.2. The DGLAP equations express that a quark (gluon) with momentum

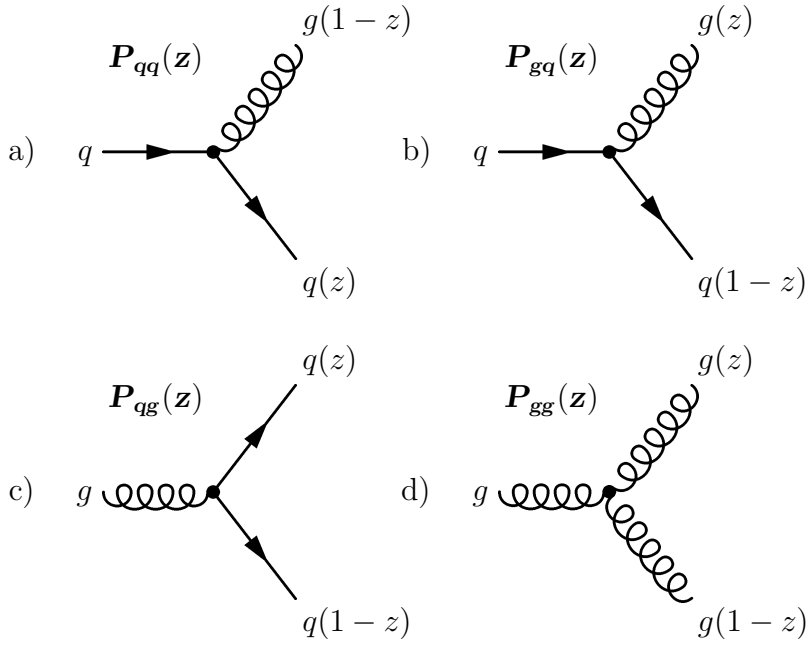

Figure 2.2: Fragmentation of the struck partons into hadrons has to be described by factorisation. It is not calculable using perturbative QCD. Hence, the shown splitting functions for the involved processes a) $P_{qq}(z)$, b) $P_{gq}(z)$, c) $P_{qg}(z)$ and d) P_{gg} have to be used in the DGLAP Evolution Equations (Eqn. 2.9).

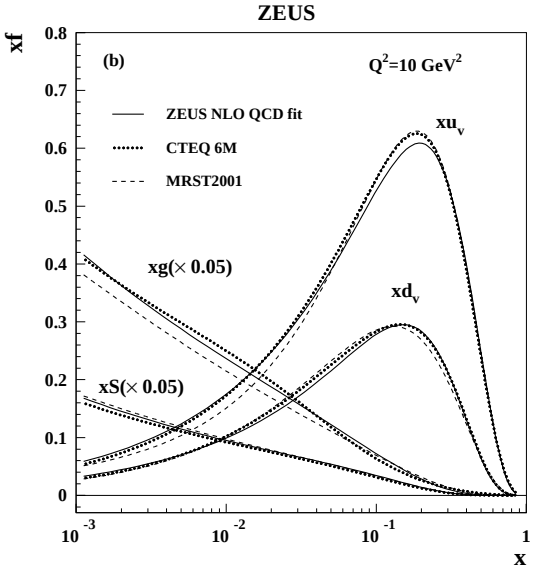

Figure 2.3: The gluon, sea, u and d valence distributions extracted from a ZEUS NLO QCD fit at $Q^2 = 10\,\mathrm{GeV}^2$ [9]. They are compared to those extracted from two other fits MRST2001 [10] and CTEQ6M [11]. Note that the gluon and sea distributions are much higher and are scaled by 0.05.

fraction x can come from a quark or gluon with momentum fraction $y > x$ which either radiates a gluon or splits into a quark–anti-quark or gluon-gluon pair. The probability for such a splitting or radiation is proportional to the respective splitting function. The integral runs over all possible momentum fractions $y > x$. Having a starting value for the parton density at fixed Q_0^2 the parton densities can then be evolved to any Q^2 value.

Due to the quarks radiating gluons as described by QCD and the gluons splitting into $q\bar{q}$ pairs, the picture of the naïve quark parton model is only a first order approximation. One of the consequences is the "scaling violation"[3] of the proton structure functions. Fig. 2.4 shows the proton structure function F_2 versus Q^2 for different values of x. It can be seen that only for $x \sim 0.22$ the structure function is independent of Q^2 , but for lower x, F_2 increases significantly with increasing Q^2. The quarks inside the proton produced by gluon splitting are called sea quarks. Their number increases towards lower x. For increasing Q^2 more and more sea quarks at low x can be resolved. As a consequence the structure function rises with Q^2 in this low x region. Towards higher x the valence quarks carry the proton's momentum and the quark density decreases. Thus no more detailed structure can be resolved with higher Q^2 and the structure function decreases.

With a fixed value of α_s the scaling violation of the structure functions is calculable

[3]Which is in fact not a violation but the general case.

using perturbative QCD. Thus, its measurement allows the extraction of the gluon density in the proton (see Fig. 2.5). It should be noted that QCD predicts that the parton densities are universal. They do not depend on the probe, and should therefore be independent of the measuring experiment.

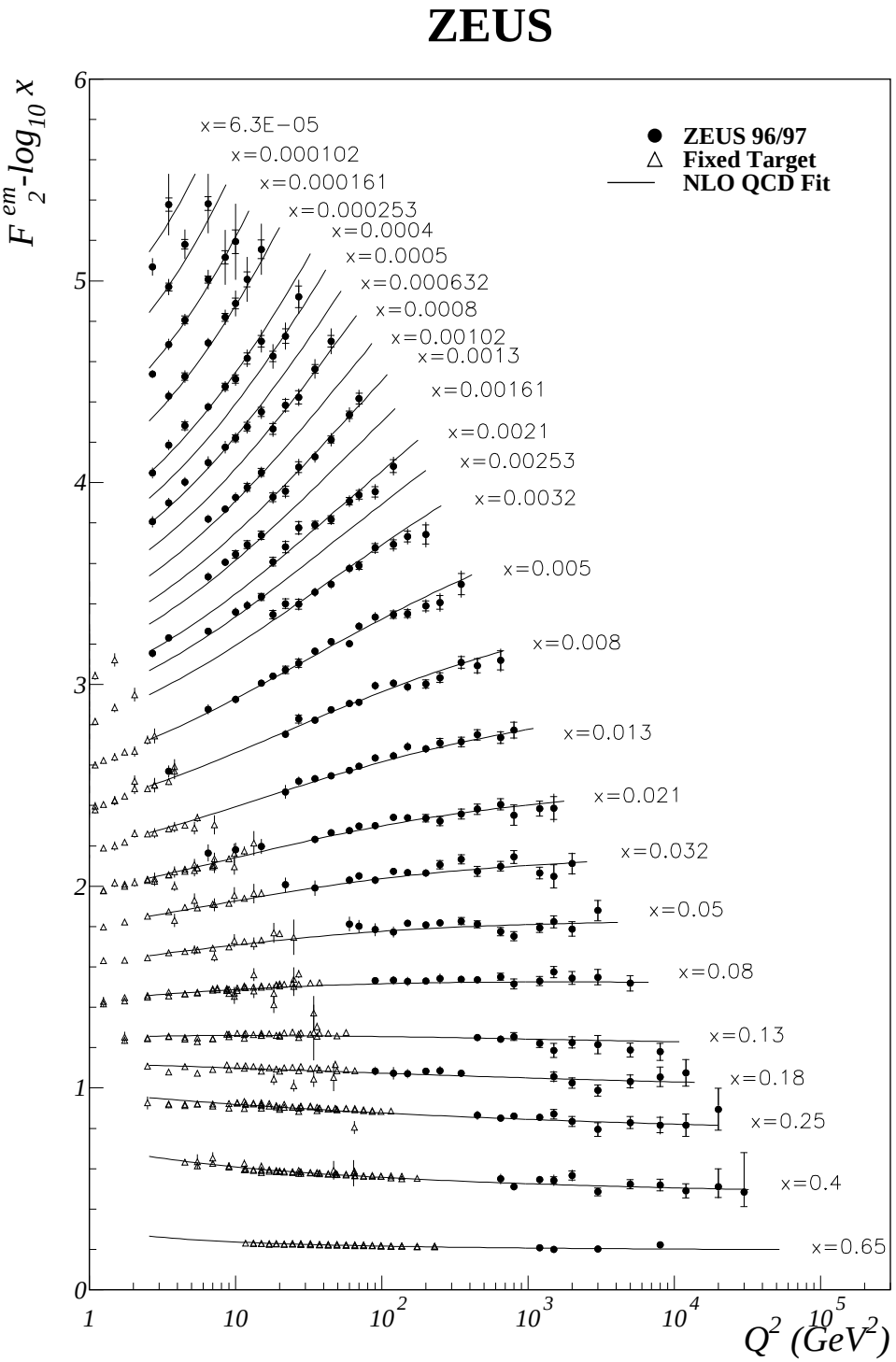

Figure 2.4: The Q^2 dependency of F_2 for different values of x [12]. The so-called "scaling violation" of $F_2(Q^2, x)$ is visible in the low x region and disappears to higher x values.

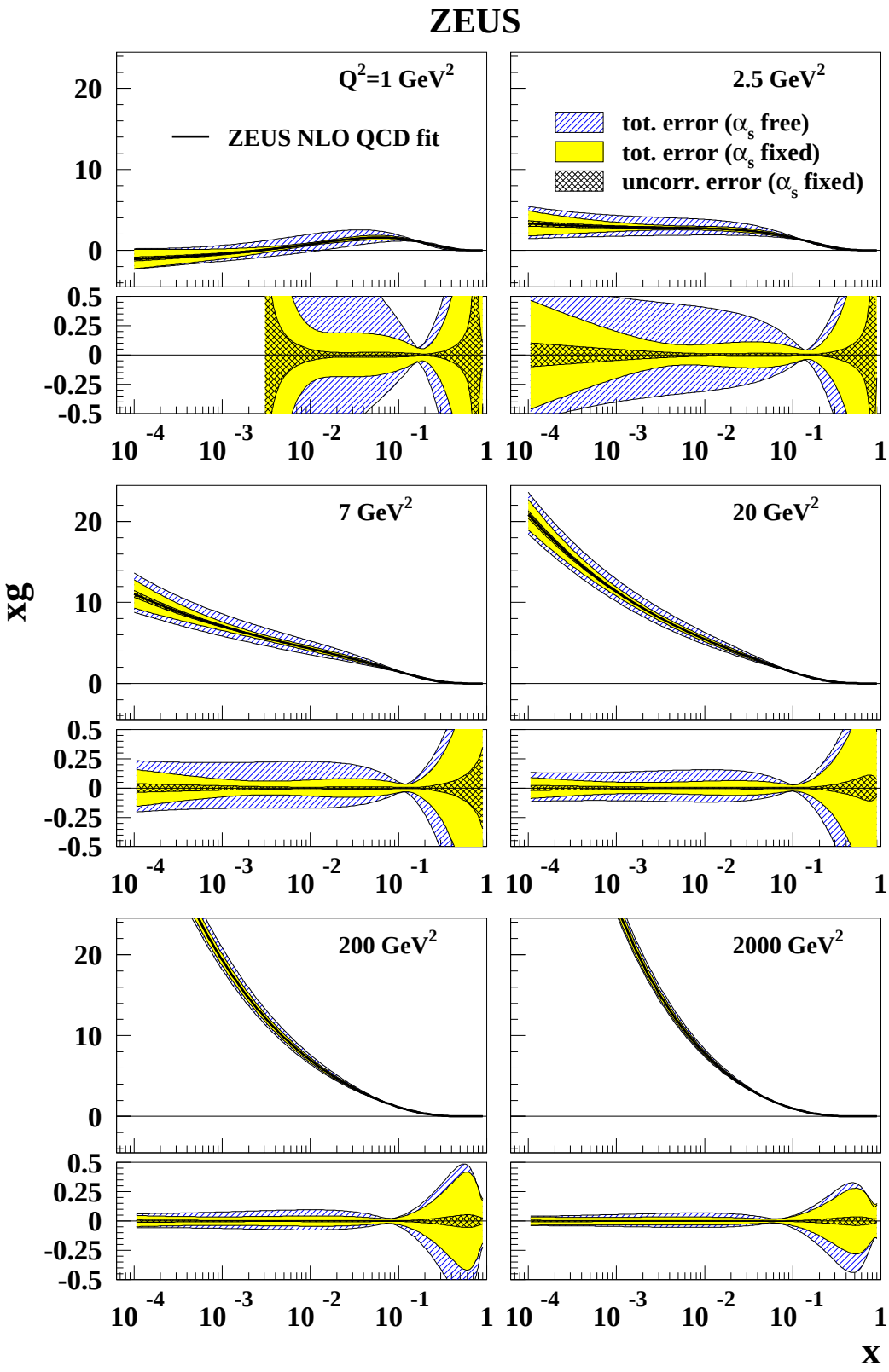

Figure 2.5: The gluon density at six values of Q^2 as obtained from the the ZEUS-S NLO QCD fit to the proton structure functions [9]. The uncertainties on these distributions are shown beneath each distribution as fractional differences from the central value.

2.1.6 Partonic Parametrisations

In order to extract the parton densities from measured proton structure functions, a parametrisation of the densities, with a number of tunable parameters, is fitted to the experimental data. Once the parameters are tuned at a given Q_0^2, the obtained parametrisation can be evolved to any Q^2 using the DGLAP evolution equations. Due to the universality of the parton densities the data used for the fit does not need to be restricted to ep-scattering only, and data from other experiments, for instance $p\bar{p}$ scattering, may be used as well. This approach is used by the CTEQ collaboration [13]. They choose a starting scale Q_0^2 of a few GeV^2 to fit their parametrisation and then evolve to higher Q^2 using the DGLAP equations. The ZEUS collaboration performed the same next-to-leading-order QCD analysis but extended it using recently available ZEUS data together with the data from previous experiments [9]. The gluon density function obtained from this analysis is shown in Fig. 2.5.

2.2 Transition Region to Photoproduction

In contrast to the photon emitted by the incoming electron in a DIS reaction, the photon emitted in a PhP reaction is quasi-real, i.e. $Q^2 \approx 0\,\mathrm{GeV}^2$ and the cross-sections of both processes are different. If the lifetime of the exchanged photon in the electron-photon interaction is long compared to its interaction time with the proton, the interaction can be factorised into the emission of a photon by the electron, and their subsequent interaction of the photon with the proton [14]. This condition is met if

$$x \ll \frac{1}{2r_p m_p} \cdot \sqrt{1 + \frac{4m_p^2 x^2}{Q^2}}\ , \tag{2.15}$$

i.e. for small x and/or large Q^2 ($r_p \approx 1\,\mathrm{fm}$, the proton radius). The electron is treated as source of the photon flux and the interaction is described by the total photon-proton cross-section. The longitudinal and transverse components of the cross-section can be expressed separately, taking into account that the photon has in general three possible helicity eigenstates $\lambda = 0, \pm 1$:

$$\begin{aligned} \sigma_T^{\gamma^* p} &= \frac{1}{2}(\sigma_+ + \sigma_-) \\ \sigma_L^{\gamma^* p} &= \sigma_0\ . \end{aligned} \tag{2.16}$$

The cross-sections for unpolarised photons with $\lambda = +1$ and $\lambda = -1$ are equal, which can be shown by requiring parity conservation. The cross-sections can also be related to the structure functions by

$$\sigma_{tot}^{\gamma^* p} = \sigma_T^{\gamma^* p} + \sigma_L^{\gamma^* p} = \frac{4\pi^2\alpha}{Q^2} F_2 \tag{2.17}$$

$$\sigma_L^{\gamma^* p} = \frac{4\pi^2\alpha}{Q^2} F_L \tag{2.18}$$

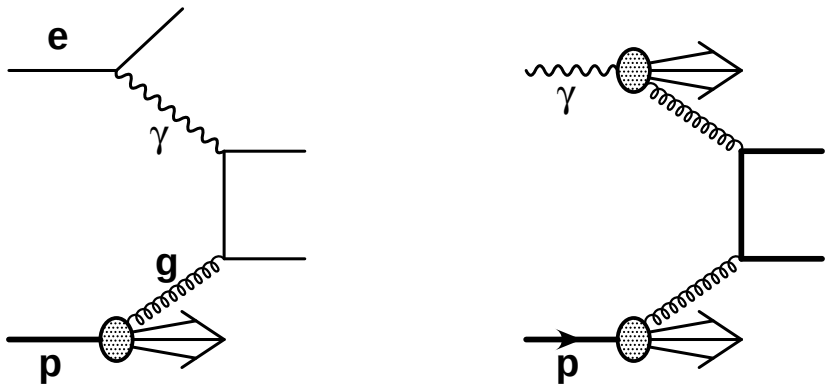

Figure 2.6: The LO direct (left) and NLO resolved (right) contributions to the production of heavy quarks. In the direct process the photon couples directly to the quark whereas in the resolved process the hadronic structure of the photon becomes essential.

In a PhP reaction there is no longitudinal contribution to the cross-section in Eqn. 2.17, because a real-photon has only transverse helicity eigenstates. As a consequence in the transition region between DIS (at ZEUS usually defined as $Q^2 > 2\,\mathrm{GeV}^2$) and PhP where $Q^2 \to 0$, the longitudinal contribution to the cross-section and F_2 will decrease and should disappear completely at $Q^2 = 0\,\mathrm{GeV}^2$.

Since the DGLAP equations have been derived in perturbative QCD, they cannot be expected to be valid when α_s becomes large, equivalent to Q^2 becoming small; $\alpha_s \approx 0.5$ at $Q^2 = 1\,\mathrm{GeV}^2$. It is important to see where perturbative QCD breaks down, i.e. where they predict a Q^2 dependency of the cross-sections and structure functions that is incompatible with the data.

Another limitation of the DGLAP formalism appears when considering the terms that have been neglected so far; there is no recombination mechanism for quarks and gluons, i.e. the process $q\bar{q} \to g$, and thus their number grows towards lower x for increasing Q^2. However, at some point this increase must violate unitarity (an upper bound for the cross-section where the probability of anything to happen becomes greater than 1). Therefore measurements at low Q^2 can be used as a tool to look for signs of recombination.

A speciality of PhP events is that like purely hadronic reactions, photoproduction is expected to have a soft component, due to peripheral processes, as well as a hard component from the scattering of the parton from the proton on a parton from a vector meson. The vector meson comes from a photon fluctuation before the interaction with the soft component. In addition to its hadronic features, the photon can also couple directly to quarks and the coupling is point-like. Therefore the scattering processes are distinguished into two types of processes shown in Fig. 2.6: the "direct" and the "resolved" processes.

The PhP regime can be described theoretically using phenomenological models such as the Vector Dominance Model (VDM) [15] and the Regge theory [16, 17]. The VDM makes the ansatz that the photon is a superposition of the bare photon and of vector-meson states: $|\gamma>=|\gamma_{\text{bare}}>+\sum|V>$, where $V=\rho,\omega,\phi$. Because one observes that the VDM is in agreement with experimental data only at low Q^2 it has been extended to the Generalised VDM (GVDM) [18]. The idea of GVDM is to extend the set of ρ, ω and ϕ by a mass continuum of heavier vector meson states.

Regge theory was originally developed in the early days of strong interaction physics and provides a successful description of soft hadronic cross-sections, as well as of elastic and diffractive scattering. As usual in scattering processes, the interaction of two hadrons is viewed as mediated by the exchange of particles. In the beginning the strong interaction could be well described by one-pion exchange; however, there is no justification not to allow the exchange of other mesons with higher spin, which would unfortunately violate the Froissart bound – an upper limit for cross-sections – for spin ≥ 1. Regge theory solved this problem by the introduction of the concept of the exchange of a trajectory of particles (a reggeon), corresponding to the exchange of many particles with different spin, $J=0,2,4\ldots$ or $J=1,3,5\ldots$, and otherwise identical quantum numbers. A trajectory is made by a group of particles which lie on a straight line in the Chrew-Frautschi plot [19] of spin vs. mass squared. A very prominent prediction of this model is the postulate of a new trajectory particle with $J^{PC}=0^{++}$, the pomeron. Glueballs, bound states of two gluons, would be possible candidates. However, the interest in the Regge theory has decreased over the years as it was unable to describe hard hadronic processes and attempts to make the theory more rigorous proved to be problematic. The Regge theory was partly resurrected when processes interpreted as hard scattering off a pomeron were observed [20, 21] and when at HERA a significant fraction of similar events was found, considered as diffractive deep-inelastic scattering, or deep-inelastic scattering on the pomeron [22, 23].

Previous inclusive ZEUS measurements [24] supported the expectation that in the low Q^2 regime, the dominant processes can be assumed to be non-perturbative and therefore can be described by Regge and GVDM models (Fig. 2.7). However, with increasing Q^2 perturbative contributions become more important. Thus it is of fundamental interest to understand the role of soft and hard processes in different reactions theoretically, and to measure where in Q^2 the transition takes place in the production processes of charmed mesons.

2.3 Heavy Quarks in DIS

Quarks with masses which are considerably higher than the value of Λ, for instance $m_{c/b}\gg\Lambda$, with $m_c=1.2$ to $1.5\,\text{GeV}$ and $m_b=4.1$ to $4.4\,\text{GeV}$ [25], are so-called "heavy" quarks. Therefore, in addition to Q^2 , representing the hard scale for deep-inelastic *ep*-scattering, another hard scale appears, if we consider events with heavy

quark production ($\alpha_s(\mu = m_c) = 0.39$, $\alpha_s(\mu = m_b) = 0.22$ [25]. This makes the measurement of heavy quark production in DIS an interesting test of perturbative QCD, especially in the transition region to PhP.

2.4 Charm Quark Production Mechanism

In this section the heavy quark production mechanisms and their theoretical description are discussed. The focus is on open charm production, since this is the subject of this thesis. Two theoretical approaches exist to describe the production of charm in deep-inelastic *ep*-scattering. In the first approach no charm inside the proton is present, and it is only produced extrinsically by "heavy flavour creation" [26, 27]. Hence, in leading-order, charm is produced exclusively via the boson-gluon-fusion process, $\gamma^* g \rightarrow c\bar{c}$, as illustrated in Fig. 2.8b. In this picture the charm production cross-section is directly correlated with the gluon density in the proton and is therefore expected to increase towards low x. Comparisons of experimental results with theoretical predictions indeed show that the BGF process is the predominant production mechanism for charm quarks in deep-inelastic *ep*-scattering at HERA [28, 29, 30, 31].

The second approach is intrinsic charm production, where a $c\bar{c}$ is assumed to exist in the proton bound state, and is produced via the so-called "heavy flavour excitation" [27]. These charm quarks are not taken into account in the perturbative QCD description. Results from EMC fixed target experiments gave indications for this intrinsic charm component at high x. The flavour excitation process assumes that charm quarks already exist within the radius of the proton. The virtual photon excites a heavy parton inside the proton, which means that the process depends on the virtuality of the photon and is kinematically only possible for $Q^2 \gg m_c^2$ and therefore does not play a role in this analysis.

Several schemes exist to perform the calculation of heavy quark production, where the main difference between them is the treatment of the mass of the charm quark. The zero-mass variable-flavour-number scheme (ZM-VFN) treats the charm quark as a massless parton. Depending on the scale Q^2 of the process, the number of active partons is either four or five. In Eqn. 2.8 the sum in this scheme runs over $a = u, d, s, g$ for $Q^2 < m_c^2$ and $a = u, d, s, c, g$ for $Q^2 > m_c^2$. The partonic structure function describes the hard scattering for all active partons, assigning them zero mass. For charm production this scheme is a reasonable approximation for $Q^2 \gg m_c^2$, and clearly becomes unreliable in the region where $Q^2 \sim \mathcal{O}(m_c^2)$. In the fixed-flavour-number scheme (FFN), a fixed number of flavours, where all quarks are regarded as massless, are assumed to contribute to the proton sea at all values of Q^2. In the FFN3 scheme only the light partons, $a = u, d, s, g$, are included in the proton parton densities f_a. The production of the heavy charm quark is calculated via the hard scattering process, using the charm mass. The perturbative calculation contains logarithmic factors, $\ln(Q^2/m_c^2)$, which become large if Q^2 becomes large. Hence the

FFN scheme is most reliable in a region where $Q^2 \sim m_c^2$, and becomes inappropriate in the higher Q^2 region. The FFN4 scheme also treats charm as a massless active flavour at all values of Q^2 and therefore is only reliable at very high Q^2 and thus not used to calculate the predictions for the measurements presented in this thesis. Other schemes exist which try to cover the problematic region between $Q^2 \geq m_c^2$ and $Q^2 \gg m_c^2$ where none of the above schemes is appropriate [32]. One of them is the ACOT (Aivaziz-Collins-Olness-Tung) scheme, which matches the FFN scheme with the ZM-VFN scheme with non-zero-mass charm quarks. The problematic terms in the FFN scheme, $ln(Q^2/m_c^2)$, can be resumed and become a parton distribution f_c without taking the limit $m_c^2 \to 0$ as done in the ZM-VFN scheme.

In this thesis the results will be compared to calculations which are using the FFN3 scheme because this scheme is expected to be the most reliable in the low Q^2 region below $1\,\mathrm{GeV}^2$.

2.4.1 Contribution of $F_2^{c\bar{c}}$ to the Proton Structure Function

The double differential cross-section for charm production in deep-inelastic scattering events, $e+p \to e+c+\bar{c}+X$, where one of the charm quarks is tagged, can be expressed in terms of charm structure functions $F_i^{c\bar{c}}$, in analogy to Eqn. 2.5 in Section 2.1.4. Considering only virtual photon exchange, and thus neglecting F_3, and substituting F_1 by $(\frac{1}{2x}(F_2 - F_L))$, the following expression is obtained:

$$\frac{d^2\sigma_{c\bar{c}}^{\mathrm{NC}}}{dxdQ^2} = \frac{2\pi\alpha^2}{xQ^4}[(1+(1-y)^2)F_2^{c\bar{c}}(x,Q^2) - y^2 F_L^{c\bar{c}}(x,Q^2)]\,. \tag{2.19}$$

In the y range covered by this analysis the contribution to the cross section from the longitudinal structure function $F_L^{c\bar{c}}$ is small and therefore neglected. The charm contribution to the inclusive proton structure function F_2 is up to 20% at small x [33].

A precise measurement of $F_2^{c\bar{c}}$ is therefore interesting for the understanding of the sea quark and gluon distribution of the proton. As discussed above, charm production is dominated in leading order by BGF, $\gamma^* g \to c\bar{c}$. Considering Eqn.2.8 the measurable quantity $F_2^{c\bar{c}}$ can therefore directly be related to the gluon density g of the proton by

$$F_2^{c\bar{c}}(x,Q^2) = g(x,\mu_F) \otimes \hat{F}_2^g(x, \frac{Q}{\mu_F})\,. \tag{2.20}$$

$\hat{F}_2^g$ describes the BGF part, which is calculable in perturbative QCD. The extraction of $g(x)$ from charm measurements and its comparison with the result from the scaling violation of F_2 thus provides another consistency check of QCD. In addition to the LO BGF process, next-to-leading order processes (NLO), in $\mathcal{O}(\alpha_s^2)$, contribute to the charm cross-section. These are the gluon-bremsstrahlung process, $\gamma^* g \to c\bar{c}g$, and processes of the type $\gamma^* q(\bar{q}) \to c\bar{c}q(\bar{q})$. The $q(\bar{q})$ is a massless quark, radiating a gluon which then interacts with the virtual photon. A NLO calculation for the charm cross-sections exists [34] and will later compared to the measurements.

2.4.2 Fragmentation of Heavy Quarks

The particles observed experimentally are the decay products of the hadrons resulting from fragmentation of the charm quarks. Measurements of the charm cross-section and the charm structure function, $F_2^{c\bar{c}}$, therefore require phenomenological descriptions about the fragmentation process and the subsequent decay into the observed particles.

To calculate the cross-section for processes like $ep \to eHX$, where H means a heavy hadron, the process of fragmentation needs to be described theoretically. The hadronisation of charm quarks into hadrons (confinement) is not calculable perturbatively in QCD, but is assumed to be independent of the hard scattering process. Hence the calculation of the cross-section can be factorised in a way similar to the factorisation of the proton structure function, which was described in Section 2.1.4. To extend the calculation for charm production to the production of heavy hadrons, the cross-section for charm production has to be convoluted with a fragmentation function.

Several models exist to describe the process of fragmentation of heavy quarks, Q, into hadrons. The Peterson fragmentation function [35] is frequently used in the description of the transition $Q \to H(Q\bar{q}) + q$:

$$D_Q^H(z) = \frac{N_H}{z}(1 - \frac{1}{z} - \frac{\epsilon_Q}{1-z})^{-2} \tag{2.21}$$

The heavy quark, Q, with momentum P is marginally slowed down by picking up a light anti-quark $\bar{q}$. The resulting hadron then carries the momentum zP, with a probability proportional to $D_Q^H(z)$. N_H is the normalisation factor constrained by the sum over all hadrons containing the heavy quark, $\sum_H \int dz D_Q^H(z) = 1$. The only free parameter is ϵ_Q of $\mathcal{O}(\frac{m_q^2}{m_Q^2})$, which can be determined from fits to experimental data from $e^+ + e^-$ colliders. Fig. 2.9 shows the Peterson fragmentation function for different values of ϵ_Q. The function peaks at $z = (1 - 2\epsilon_Q)$ and its width is $\sim \epsilon_Q$. Thus the higher ϵ_Q the softer the spectrum of the fragmented heavy hadrons.

The variable z in Eqn. 2.21 is not directly accessible by experiments, and so other scaling variables which are close approximations to z must be used. Figure 2.10 shows the inclusive cross-section for D^0 and D^{*+} production versus the variable $x_P = p/p_{max}$. The measurements were performed by the ARGUS [36] and CLEO [37] collaborations in $e^+ + e^-$ collisions at $\sqrt{s} \sim 10\,\text{GeV}$. A fit to the data using only the Peterson fragmentation function yields $\epsilon_Q(D^0) = 0.135 \pm 0.010$ and $\epsilon_Q(D^*) = 0.078 \pm 0.008$. In order to obtain results which are comparable to other experiments, radiative effects must be taken into account. This has been done by the OPAL collaboration. They studied the production of $D^{*\pm}$ mesons in Z_0 decays. A fit of the Peterson function gives a softer fragmentation spectrum, with $\epsilon_Q(D^*) = 0.035 \pm 0.009$ [38, 39]. This is the value used as input for predictions for D^* production at HERA.

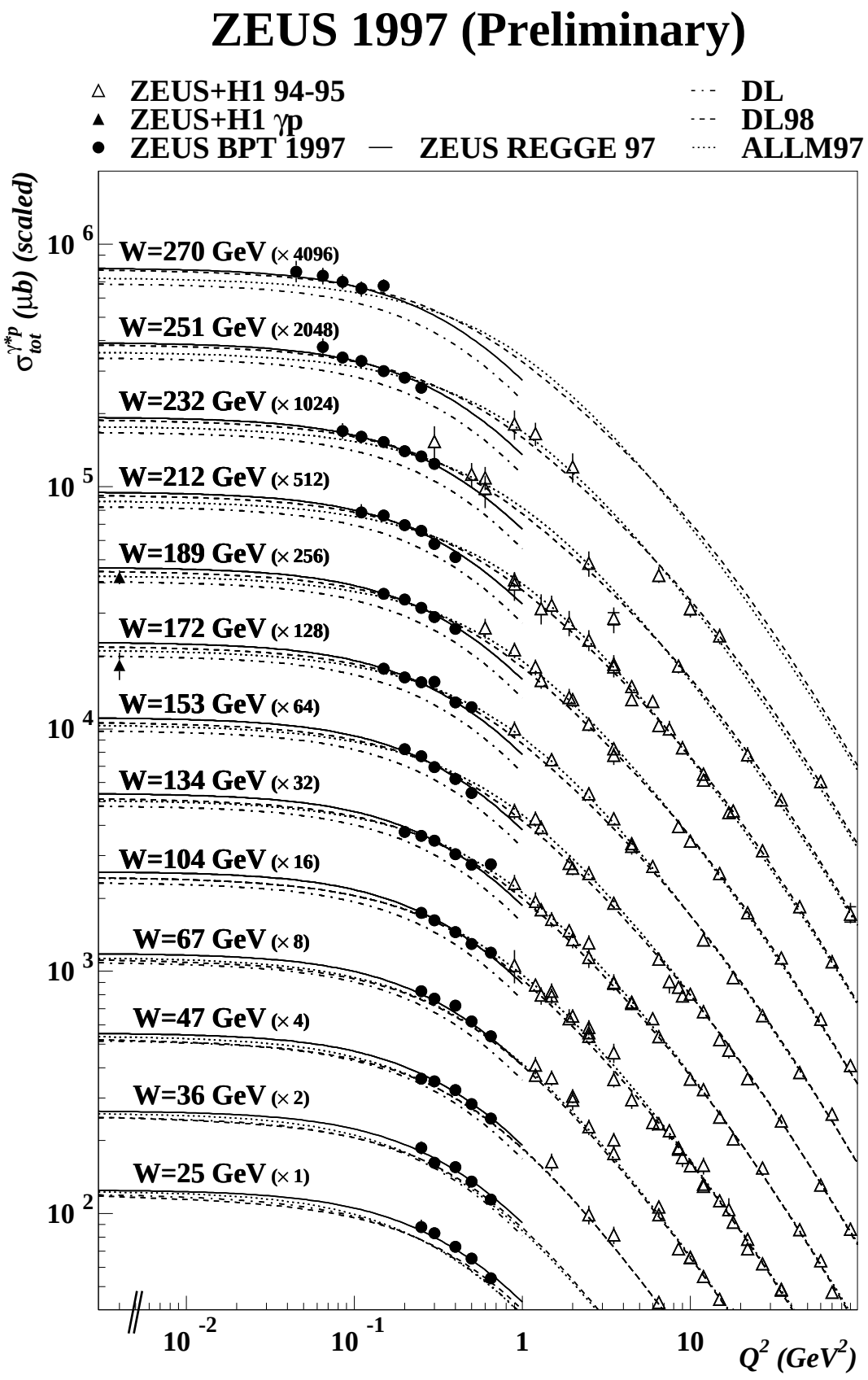

Figure 2.7: $\sigma_{\rm tot}^{\gamma^* p}$ vs. Q^2 in bins of W from a previous inclusive ZEUS DIS measurement [24].

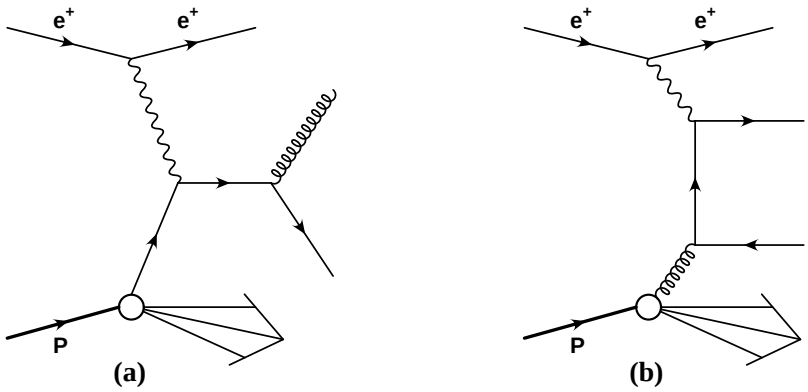

Figure 2.8: LO contributions to D^* production cross-section: The a) the QCD Compton process and b) boson-gluon-fusion (BGF). At low Q^2 BGF dominates the production. For each of both processes exist another indistinguishable process of the same amplitude where for a) the gluon radiation takes place before the interaction of the quark with the photon and for b) the outgoing quark lines are twisted.

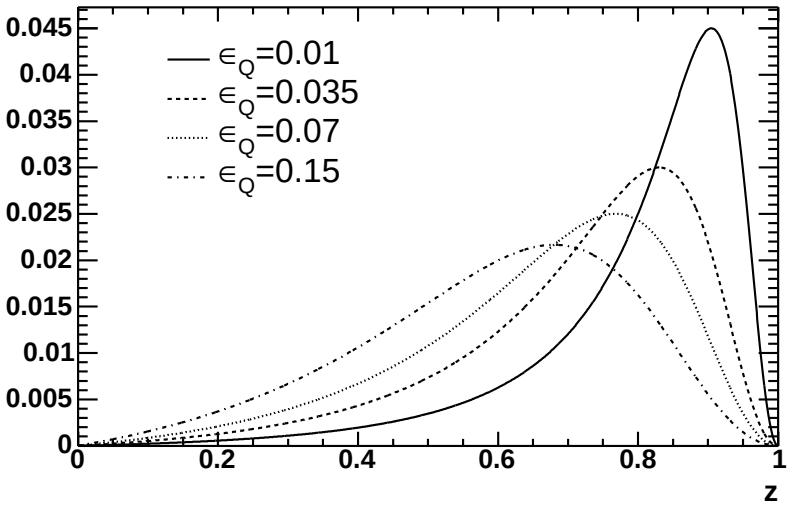

Figure 2.9: The Peterson fragmentation function for different values of ϵ_Q

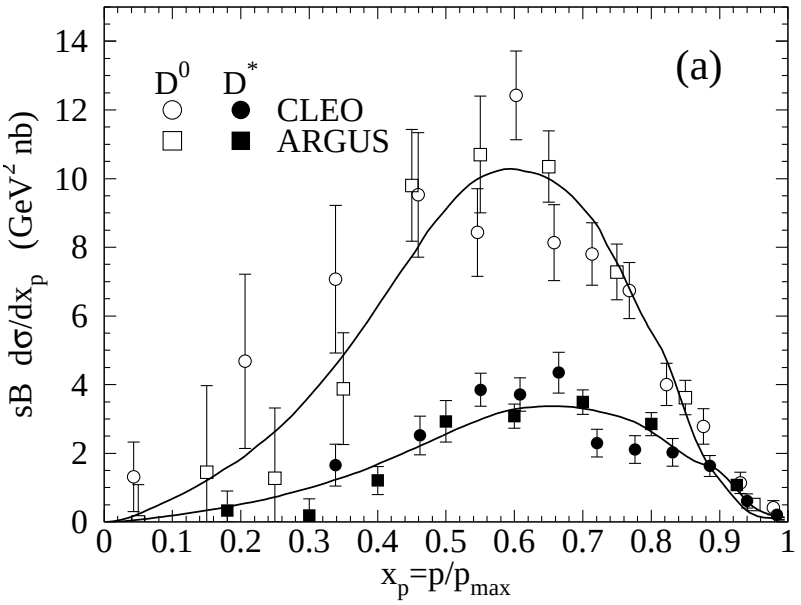

Figure 2.10: Inclusive cross-sections for D^0 and D^* production vs. $x_P = p/p_{max}$. The solid lines indicate the result of fits to the data using the Peterson fragmentation functions [40].

Chapter 3

Physics Simulation

The complexity of the ZEUS detector system complicates the accurate determination of its efficiency and resolution for the desired particle momentum and position reconstruction as well as for the energy measurement. The measured data has to be corrected for the detector effects in order to obtain detector independent and comparable results.

The response of the detector to a certain physics event has to be studied using a simulation of the scattering process (event generator) and then a complete detector simulation. Monte-Carlo (MC) simulation is the basis of these studies.

The event generators used for this analysis will be described in the first section. The second section is dedicated to the description of a NLO calculation for charm production in DIS events, which will be used to compare the results of the D^* production at low Q^2 analysis. The chapter will end with an description of MOZART, the detector simulation package.

3.1 Event Generators

The initial physics scattering process is simulated by an event generator. In this thesis two of these generators are used: HERWIG and RAPGAP. Both use as theoretical input perturbative QCD for the hard process of charm and beauty production in the scattering reaction.

HERWIG and RAPGAP simulate essentially the same processes but RAPGAP includes an extension to also generate diffractive events. HERWIG is used as the standard MC generator in this analysis because the $\eta(D^*)$ distribution (Fig. 3.1) agrees better with previous D^* production measurements at HERA [41].

The soft part is described by phenomenological models – e.g. the parton density function and the fragmentation process. In the next step the particles, namely hadrons and leptons, are propagated through the ZEUS detector. In the propagation effects like decays, multiple scattering, ionisation, etc. are taken into account using the MOZART (Section 3.3) package.

3.1.1 HERWIG

The dominant mechanism to produce charmed and bottom mesons at low Q^2 in DIS and photoproduction is the BGF mechanism (described in Section 2.4). In order to generate a MC sample of such events for the analysis the event generator HERWIG 6.301 [42, 43] is used. Photoproduction and beauty production events are treated as background in this analysis. The BGF process can be considered to be subdivided into resolved and direct processes (Fig. 2.6) by looking at the photon vertex. However, the ratio between the number of D^* mesons produced in both processes has not been measured in the transition region between photoproduction and DIS ($0 < Q^2 < 1\,\mathrm{GeV}^2$). Therefore the ratio of resolved and direct processes which is used to create the initial HERWIG MC sample was taken from previous ZEUS photoproduction measurements (~ 0.3). In order to estimate the corresponding error on the cross-section calculation different values of the ratio are assumed and put into a systematic uncertainty.

The HERWIG event generator starts the physics simulation by generating the 4-momenta of the particles involved in the ep reaction according to the theoretical predictions. The hard part of the scattering process is calculated using the pQCD processes, here namely the BGF process. The parametrisations of the parton densities functions of the proton can be selected. For the MC sample produced for this analysis the CTEQ5L pdf parametrisation was chosen, where the suffix "L" denotes a leading-order fit to CTEQ data. The generator takes care of radiative processes before and after the ep-scattering process, i.e. initial and final state radiation. QCD radiative processes are simulated in QCD parton showers based on the DGLAP evolution equations [6, 8] to leading order in α_s.

The partons are transformed into hadrons using the cluster fragmentation model [44], whereby the primary hadrons are produced from an isotropic two body decay of colour-singlet clusters formed from partonic constituents.

3.1.2 RAPGAP

The RAPGAP event generator [45] is used in this analysis to study the systematic uncertainties coming from different parton shower algorithms and fragmentation models. RAPGAP uses the program packages HERACLES, JETSET and LEPTO – all described below – enhanced with parton showers based on DGLAP evolution equations calculated to leading order in α_s. For a more detailed simulation of the LO process the exact matrix element of the specific process can be included. For heavy quark production this is done via the BGF process.

Again, the CTEQ5L parametrisation of the parton densities of the proton is chosen for this analysis. The parton showers comprise gluon radiation from the charm quarks and approximate NLO corrections for charm production.

For the QED radiative process along the electron beam-line, RAPGAP uses the HERACLES event generator [46] to generate the $(e\gamma^* e)$ vertex including initial and

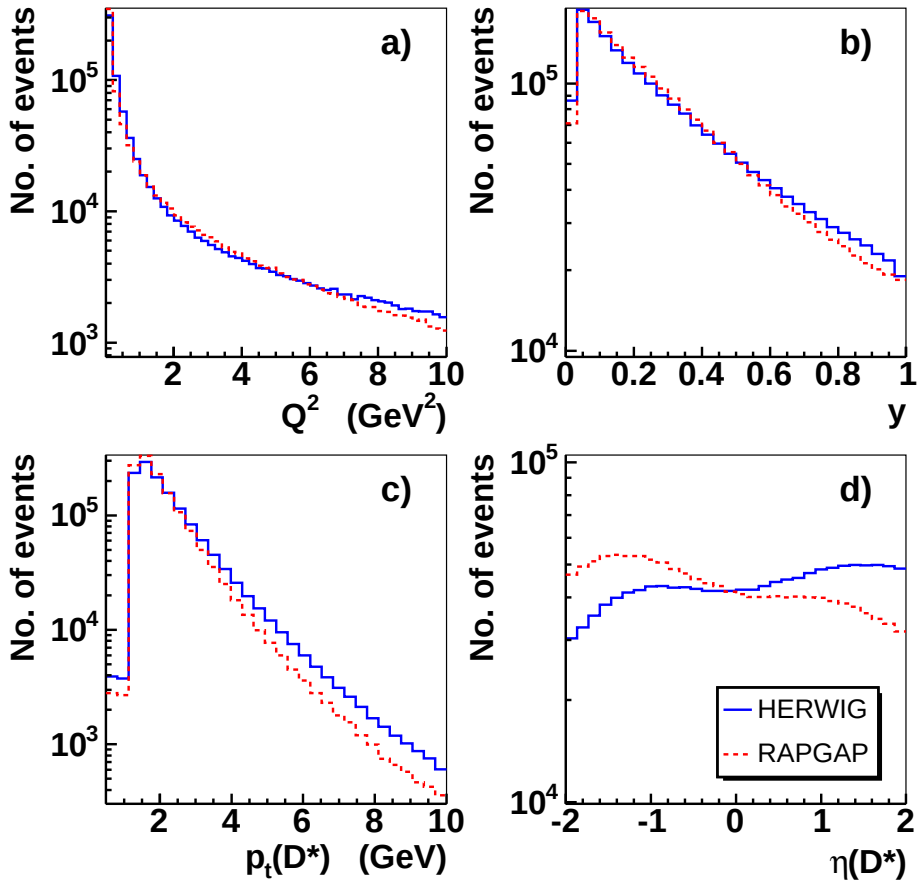

Figure 3.1: Distributions of the kinematic variables a) Q^2, b) y, c) $p_t(D^*)$ and d) $\eta(D^*)$ taken from the event generator. Solid lines indicate the HERWIG MC distributions, RAPGAP MC is represented by dashed lines. The RAPGAP MC distributions are normalised to the same area as the HERWIG MC distributions.

final state radiation as well as virtual corrections.

The fragmentation is simulated by JETSET using the Lund string model [47]. In this model the proton remnant is connected with the produced – coloured – partons by a colour string. The further the parton moves away from the proton remnant, the more energy is stored in the colour string and it breaks up by the production of $q\bar{q}$ pairs. By this method light $q\bar{q}$ pairs are produced between the outgoing partons and the proton remnant. The production of heavy quarks in this process is suppressed due to their large mass and hence they are not expected to be produced via fragmentation but only in the hard scattering process.

The treatment of the proton remnant is done by LEPTO [48]. In the case of BGF a colour octet gluon is removed from the proton which creates a $q\bar{q}$ pair. Two colour strings are generated connecting each of the quarks with the proton remnant.

A comparison of the distributions of the relevant kinematic variables from the event generators are shown in Fig. 3.1. The slope of the $\eta(D^*)$ distributions are different for both generators; the HERWIG distribution rise towards higher $\eta(D^*)$ values while the RAPGAP distribution is falling. The measured distributions of $\eta(D^*)$ (Fig. B.1d) for the analysis presented in this thesis and for previous ZEUS D^* in DIS analysis [49] agree better with the HERWIG distribution and therefore HERWIG is used in this analysis for the calculation of the acceptance. However, the discrepancies between the two generators are well within the statistical error of this analysis and therefore the RAPGAP MC is used in the systematic uncertainty calculation.

3.2 NLO Calculations

An integration of the LO matrix elements is performed in HERWIG and RAPGAP which depends on the renormalisation and fragmentation scale of the scattering process. Therefore calculations of higher order are desirable. For heavy quark production a MC program named HVQDIS [50] exists, which performs the calculations up to NLO.

3.2.1 HVQDIS

Instead of generating single events like an event generator, the HVQDIS program provides kinematic distributions calculated in LO and NLO for the production of heavy quarks in DIS. Thus, no full MC simulation including the detector and trigger simulation of the NLO predictions is possible. The measured data has to be corrected for detector effects with LO MC such as HERWIG and the obtained distributions can then be compared to the NLO predictions from the HVQDIS program.

The FFN3 parametrisation scheme (see Section 2.1.4) is used to perform the calculation assuming the charm production occurs only via BGF and higher order QCD processes. The calculation starts with the differential cross-section for charm production in terms of the proton structure functions. Higher order corrections, including gluon bremsstrahlung, higher order production processes and virtual corrections, are calculated and added as NLO corrections to the charm structure functions.

The input parton densities are by default limited to three factorisation schemes: GRV, CTEQ4F3 and CTEQ5F3 [13]. In this thesis an enhanced parton density set based on the ZEUS NLO fits [51], including the results of ZEUS open charm analyses from 1995 to 2000, is used. In order to use these PDFs the HVQDIS program was extended by the ZEUS collaboration [52].

The results are expected to be most accurate at $Q^2 \leq m_c^2$ and become less reliable for $Q^2 \gg m_c^2$ due to the use of the FFN3 scheme. The choice of the the charm quark mass value is left to the user and will be varied for systematic checks. The scale at

which the LO and NLO calculation are performed – e.g. $\mu^2 = (Q^2 + 4m_c^2)$ – can be chosen by the user and will also be changed for systematic checks.

The output of the program are differential distributions for parton kinematics accurate up to $\mathcal{O}(\alpha, \alpha_s^2)$. To obtain observable distributions, Peterson fragmentation is applied to both charm quarks to obtain the cross-section on the hadron level. The Peterson fragmentation function contains a single parameter, ϵ_c, that should be determined by experiment (see Section 2.4.2).

3.3 Detector Simulation

The interaction of the detector with the final state particles of the events is described in the detector simulation. For this purpose, it contains a description of the geometry and the materials of the detector, in order to be able to emulate the interaction of primary and secondary particles with matter, like shower formation etc. The decays of unstable particles inside the detector are described as well. This is the passive part of the detector simulation.

In the MC sets for this analysis the path of produced particles through the ZEUS detector is calculated using the MOZART program which is part of the MC simulation package (funnel). MOZART is based on GEANT [53], the detector simulation package. MOZART describes the decay, multiple scattering, ionisation and energy loss of the propagating particles. The knowledge of the detector response is based on the current understanding of the detector from physics studies and from test-beam measurements, always taking into account the geometry and materials.

The MC also implements algorithms that simulate the response of the active detector components to the particles as most components use the energy deposit to generate an electronic response. This is the active part of the simulation. For example, in a calorimeter the amount of energy deposited in the simulated scintillator plates could be taken as a measure of the amount of light that would be created in the real detector.

This active part is done for the ZEUS detector using e.g. the trigger simulation package (ZGANA) and the reconstruction package (ZEPHYR).

The output from the detector simulation is reconstructed with the same algorithms as the real data (although for some aspects separate branches exist, implementing a slightly different treatment of data and MC), and the output has the same format as the output from the real detector, plus some additional variables about the "true" particles. This true particle variables, e.g. Q^2_{MC}, provided by the event generator do not undergo any reconstruction and are used for detector resolution studies etc.

Chapter 4

HERA and ZEUS

The first lepton-proton collider HERA [54] collides electrons or positrons with protons and is located at DESY in Hamburg, Germany. It was approved in 1984; the electron ring was operational in 1989, while the proton ring started in 1991. Some technical details are presented in section 4.1. In the following year, the colliding beam detectors ZEUS and H1 took their first data.

The ZEUS detector, which is introduced in section 4.2, is operated by an international collaboration of 400 physicists and many engineers and technicians from around 50 institutes distributed all over the world.

4.1 The HERA Collider

HERA consists of two storage rings, one for electrons and one for protons which circulate in opposite directions (see Figure 4.1). The rings are located 15–25 m underground and have a circumference of 6.3 km.
In 1998 and the first half of 1999 electrons of 27.6 GeV collided with 920 GeV protons. From the second half of 1999 HERA switched to positrons with the same energy as the electrons. Some of the most important HERA parameters are listed in Table 4.1. During normal operation, the electrons (protons) are injected with an energy of 12 (40) GeV and then accelerated further to their nominal energy (so called "ramping"). Due to collisions with residual gas molecules ("beam gas"), the electron current drops continously with a typical lifetime between 8–16 hours. This can be seen in Figure 4.2. After this time, the electron beam is usually dumped and new electrons are filled and ramped. The electrons and protons are grouped in up to 210 bunches and the bunch crossing rate is 96 ns.

Four experiments have used the HERA facility during 1998–2000 to carry out their physics research program.

Longitudinally polarised electrons from the electron beam are scattered off the HERMES [55] target nuclei of polarised hydrogen, deuterium or ^{3}He. Thus it is possible to measure the spin structure of the corresponding nuclei. The fixed targets

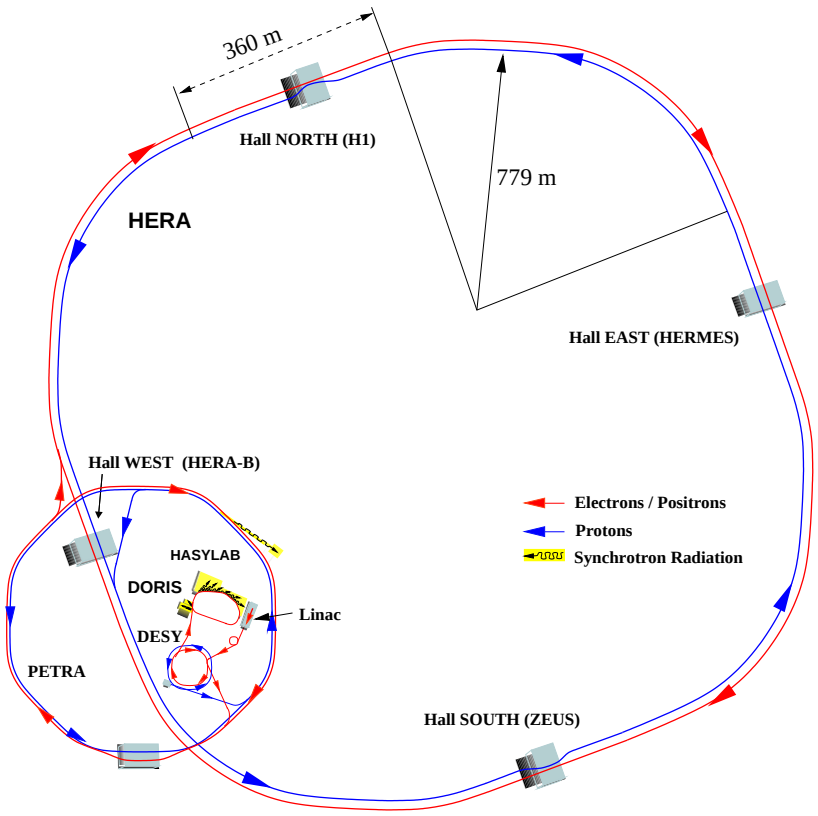

Figure 4.1: The HERA collider. Four circular 90°-arcs are connected with straight sections. There is one experiment in the middle of each straight section. The pre-accelerators Linac, DESY and PETRA are shown as well.

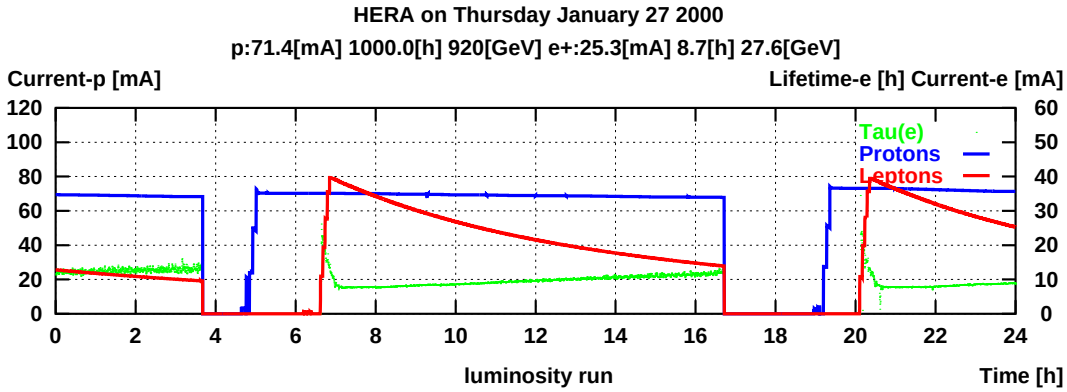

Figure 4.2: A typical 24 hour period of HERA luminosity run. At around 4:00 and 16:30, both electron and proton beams were dumped and afterwards filled again, first protons (in three steps), then positrons. Data were taken e.g. between 7:30 and 16:00.

HERA parameters	Design Values		Achieved in 1998–2000	
	$e^{\pm}$	p	$e^{\pm}$	p
Circumference [m]	6336			
Energy [GeV]	30	820	27.6	920
Centre-of-mass energy [GeV]	314		318	
Injection energy [GeV]	14	40	12	40
Maximum current [mA]	58	160	37	99
Number of bunches ("pilot" bunches)	210	210	174 (15)	174 (6)
Time between bunch crossings [ns]	96			
Horizontal beam size [mm]	0.301	0.276	0.200	0.200
Vertical beam size [mm]	0.067	0.087	0.054	0.054
Longitudinal beam size [mm]	8	110	8	170
Specific luminosity [$\mathrm{cm^{-2}s^{-1}\,mA^{-2}}$]	$\leq 3.6 \cdot 10^{29}$		$\leq 9.9 \cdot 10^{29}$	
Inst. luminosity [$\mathrm{cm^{-2}s^{-1}}$]	$\leq 1.5 \cdot 10^{31}$		$\leq 2.0 \cdot 10^{31}$	
Integrated luminosity per year [$\mathrm{pb^{-1}a^{-1}}$]	35		34	

Table 4.1: HERA design parameters and the values of the 1998–2000 running period.

at the HERA-B experiment [56, 57], are wires of different materials. Protons from the beam halo of the proton beam collide with these wires. The aim was to measure the CP-violation in the B system and the dependence of charm production on the atomic number of the wire material.

Both beams are brought to collision in the North and South experimental halls where the H1 and ZEUS detectors are located. These multi-purpose detectors are designed to analyse the particles which are produced and scattered in the ep-collisions. Their angular calorimetry coverage is almost hermetic. The detectors differ mainly in the choices that were made with respect to calorimetry. H1 [58] decided to build their liquid argon calorimeter within the magnetic field of a superconducting coil delivering 1.15 T, thereby achieving very good electron identification and energy resolution. ZEUS built a compensating calorimeter, i.e. its response to electromagnetic and hadronic showers is the same, thus achieving a good unbiased jet energy measurement.

The first period of HERA (HERA I) was completed in August 2000. In the subsequent shutdown, major upgrade modifications were made [59]. New superconducting beam focusing magnets were installed close to the interaction points at ZEUS and H1. These are designed to improve the instantaneous luminosity by a factor of ~ 5. The ZEUS and H1 detectors were partially changed and new detector components were installed. ZEUS installed the Micro-Vertex-Detector and the Straw-Tube-Tracker to improve the tracking of charged particles in order to make full use of the higher luminosity [60]. Also the luminosity system was changed.

4.2 The ZEUS Detector

The ZEUS detector [61] consists of many specialised detector components. Most of the components can be seen in Figure 4.3. The ZEUS detector is asymmetric

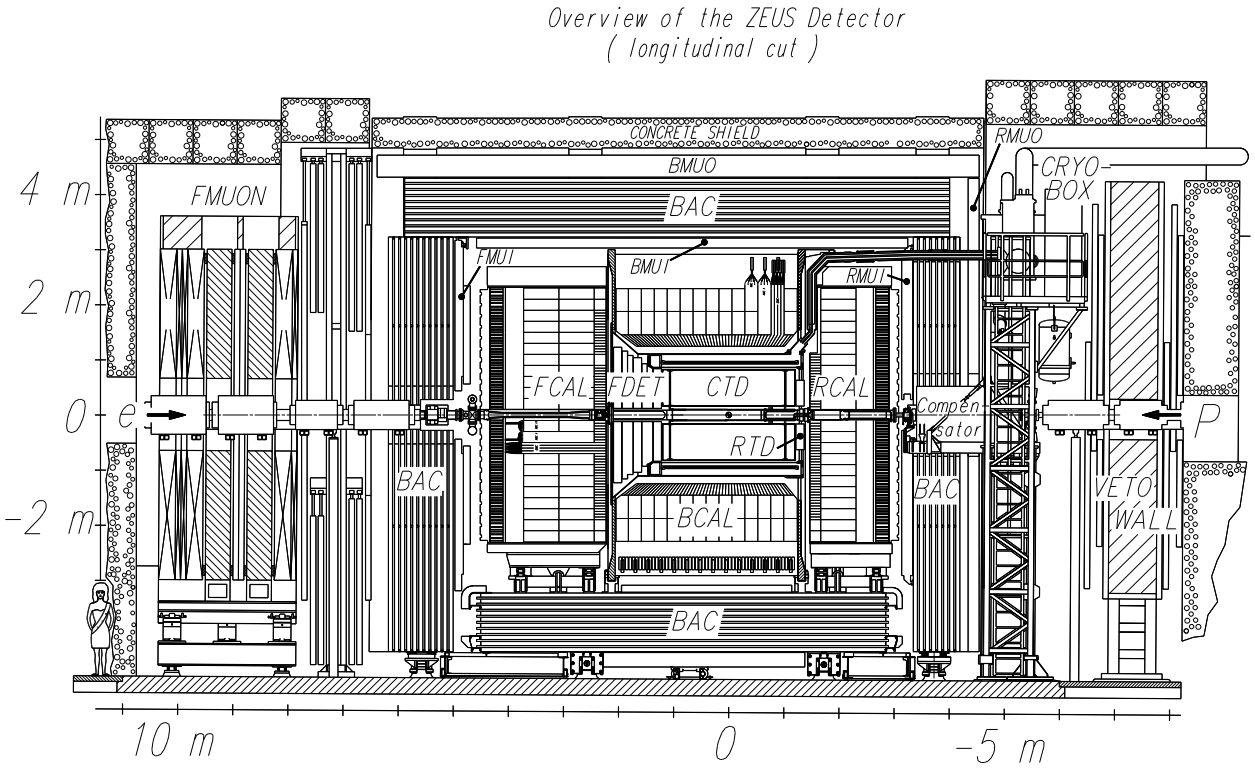

Figure 4.3: The ZEUS detector in a Z–Y-cross section.

because it is adapted to the special kinematics at HERA. The different energies of the electron and proton result in a CMS moving in the "forward" proton beam direction[1] in the laboratory system with a boost of $\beta = 0.94$. As a consequence the detector is instrumented more extensively in the forward hemisphere.

Since the start-up the ZEUS detector has seen many – almost yearly – upgrades by adding or exchanging components in the detector. Here, the status of the ZEUS detector (Fig. 4.3) as of the 1998–2000 running period is described from inside outwards.

The beam-pipe is surrounded by a tracking system for charged particles. It consists of a set of gas chambers (Figure 4.4). The cylindrical drift chamber (CTD)

[1]The ZEUS coordinate system is a right-handed Cartesian system, with the Z axis pointing in the proton beam direction, referred to as "forward direction", and the X axis pointing left towards the centre of HERA. The coordinate origin is at the nominal interaction point.

surrounds the interaction point. In the forward region, three sets of planar drift chambers (FTD) and a transition radiation detector (TRD) are installed. In the rear direction, additional tracking information is provided by one set of drift chambers, the rear tracking device (RTD). The CTD is embedded in the axial magnetic field of 1.43 T of a superconducting solenoid, thus giving the possibility to measure a charged particle's track and momentum. Additionally the inner tracking detectors are used for particle identification by dE/dx and transition radiation measurements.

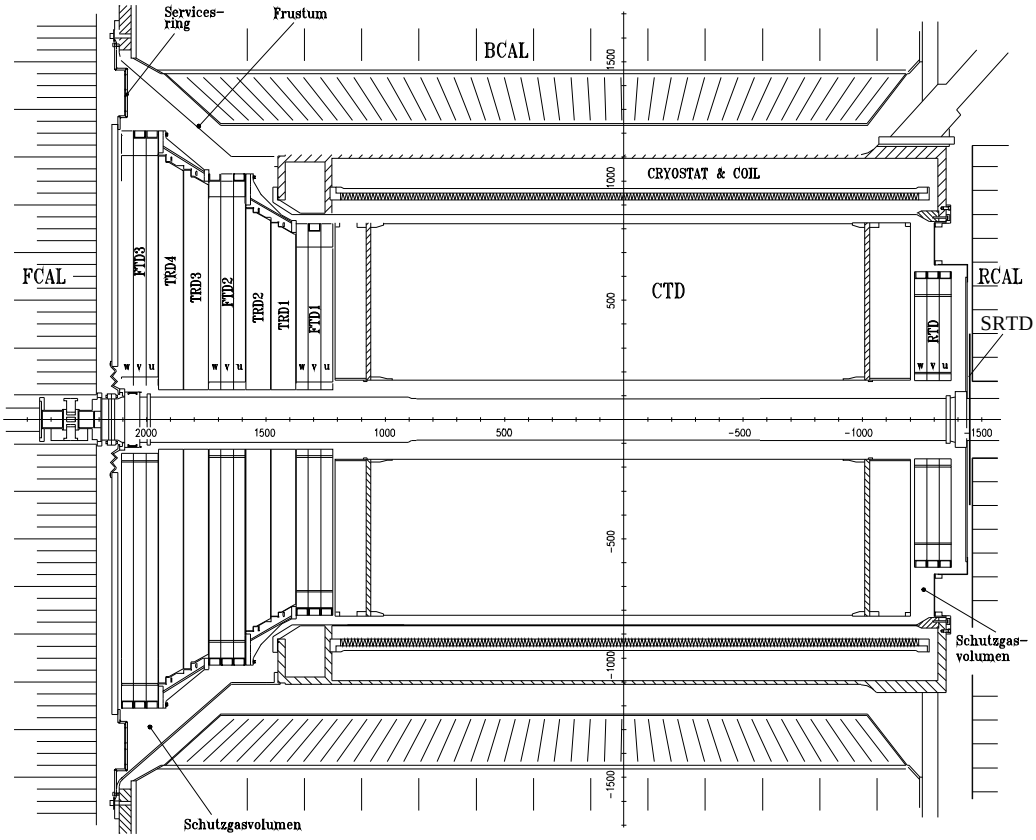

Figure 4.4: The inner components of the ZEUS detector, namely the central tracking detector (CTD), the forward tracking detector modules (FTD), the transition radiation detector (TRD), and in the rear part the rear tracking detector (RTD). The CTD is surrounded by the superconducting coil supplying the magnetic field and the first sections of the calorimeter (of FCAL, BCAL and RCAL). The small angle rear tracking detector (SRTD), which is attached to the RCAL around the beam-pipe is also shown here.

The whole inner detector is surrounded by a high resolution uranium-scintillator calorimeter (UCAL), which is the main instrument to measure the energy of electrons and hadrons. It is subdivided into three parts, the forward (FCAL), the barrel (BCAL) and the rear calorimeter (RCAL). From 1995 to 2000, the beam-pipe

calorimeter (BPC) was installed in a gap between the RCAL and the beam-pipe to detect electrons scattered under very small angles, thereby providing the possibility to measure very small values of Q^2 (Chapter 5).

An iron yoke conducts the magnetic field flux of the solenoid. The yoke consists of 7.3 cm thick iron plates, which surround the UCAL. Electromagnetic and hadronic showers are absorbed in the uranium calorimeter. If any energy leaks out, it can be measured with the backing calorimeter (BAC), consisting of proportional chambers placed inside the iron yoke [62, 63]. Muons can pass through all the calorimeter layers. Their momentum is measured in the rear (RMUON), barrel (BMUON) and forward (FMUON) region using the magnetic field of the yoke and limited streamer tubes mounted inside (R-, B-, FMUI) or outside (R-, B-, FMUO) the iron yoke [64]. The FMUO additionally uses drift chambers and the toroidal field.

Leaving the radial path through the detector and entering the axial – beam-line – path, there are several detector components close to the beam-line, which address various more specialised topics. In the proton direction at $Z = 26-96$ m six stations of silicon strip detectors measure very forward scattered protons in the leading proton spectrometer (LPS) [65]. The forward neutron calorimeter (FNC) is installed at $Z = 105.6$ m to detect very forward produced neutrons [66].

In the electron beam direction, at about 8 m, 35 m and 44 m, small calorimeters measure forward scattered electrons at different values of W and $Q^2 \approx 0\,\mathrm{GeV}^2$, thus extending the kinematic range of tagged photoproduction (see Figure 4.9).

The most important detector components for this thesis will be described in more detail in the following.

4.2.1 The Central Tracking Detector

The CTD [67] is a cylindrical drift chamber. Its active volume has a length of 205 cm, an inner radius of 18.2 cm and an outer radius of 79.4 cm. The azimuthal angle, ϕ, is covered completely whereas the polar angle region is $15° < \theta < 164°$. The CTD is operated with a mixture of argon, CO_2 and ethane[2]. It is partioned in $\rho = \sqrt{x^2 + y^2}$ into nine superlayers, and in the azimuthal angle, ϕ, into eight octants. Figure 4.5 shows the layout of a CTD octant. The number of drift cells per superlayer in an octant increases from four in the first superlayer to twelve in the ninth superlayer. Every drift cell is equipped with eight sense wires. Superlayers with odd numbers have sense wires parallel to the beam axis, while the sense wires in those with even numbers run under a certain small stereo angle to the beam axis.

For the superlayers 1, 3 and 5, the signal latency time on the sense wires can be used to produce a "Z-by-timing" measurement with a resolution (standard deviation) of $\sigma_Z \approx 4$ cm. The resolution in $r - \phi$ is about 230 µm, while in Z it is 1–1.4 mm using stereo hits. For full length tracks, this results in a transverse momentum

[2]During the running period 2000, ethanol was added in order to regain the efficiency of the previous running periods.

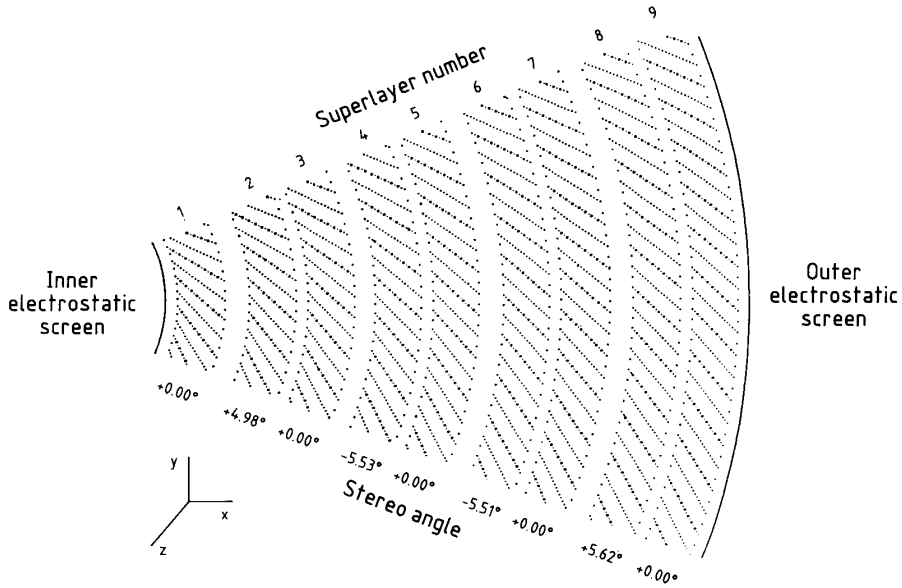

Figure 4.5: Layout of a typical CTD octant. The stereo angle of each superlayer is indicated.

resolution of $\sigma(p_T)/p_T = (0.58p_T \oplus 0.65 \oplus 0.14/p_T)\%$ with p_T in GeV and a pseudo-rapidity resolution, $\sigma(\eta)$, of about 0.002 for $p_T > 2\,\text{GeV}$ [68]. The interaction vertex is measured for events containing at least one CTD track with a typical resolution along (transversal) the beam direction of 0.4(0.1) cm. For each track, the energy loss by ionisation, dE/dxm, is determined.

4.2.2 The Uranium Calorimeter

The high resolution uranium-scintillator calorimeter (CAL) [69] is a sampling calorimeter which consists of alternating layers of 3.3 mm thick depleted uranium and 2.6 mm thick plastic scintillator plates. It is compensating, i.e. the energy response to electrons and hadrons is the same ($e/h = 1.00 \pm 0.02$). The CAL energy resolutions, measured under test beam conditions, are $\sigma(E)/E = 0.18/\sqrt{E}$ for electrons and $\sigma(E)/E = 0.35/\sqrt{E}$ for hadrons (E in GeV).

The calorimeter is divided into three parts corresponding to pseudo-rapidity regions of -3.49 to -0.72 (RCAL). -0.74 to 1.10 (BCAL) and 1.01 to 3.95 (FCAL). Each part is subdivided transversely into towers and longitudinally into one electromagnetic section (EMC) and either one (in RCAL) or two (in BCAL and FCAL) hadronic sections (HAC) as shown in Figure 4.6. The layout of an FCAL module can be seen in Figure 4.7. The CAL towers, shown in Figure 4.8, have a surface of

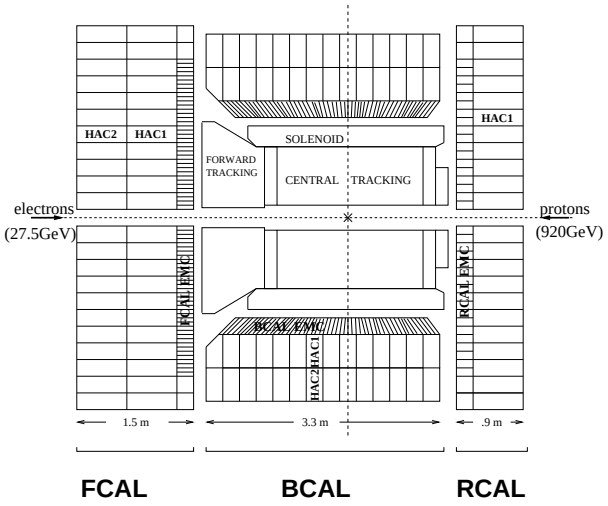

Figure 4.6: Overview of the uranium calorimeter of ZEUS. RCAL, BCAL and FCAL cover different pseudo-rapidity regions.

$20 \times 20\,\mathrm{cm}^2$; while each HAC section in a tower consists of one cell, the EMC section is transversely subdivided into four EMC cells (two in the RCAL) with rectangular surface $20 \times 5(10)\,\mathrm{cm}^2$, resulting in a better Y resolution for the RCAL and FCAL and θ in the BCAL.

4.2.3 The Luminosity Measurement

One key ingredient in the determination of a cross-section is the measurement of the luminosity. It has to be done with high precision, because its variance immediately adds a systematic uncertainty on the time-integrated luminosity to each measured cross-section. A way to a measurement of the luminosity is to measure the number of events N for a process with a well-known cross-section σ. At ZEUS the number of events with Bremsstrahlung photons from the Bethe-Heitler process $ep \to e\gamma p$ is counted. The cross-section for this process is known from QED to an accuracy of better than 0.5%. There is a detector to measure the photons (LUMIG), and one for the scattered electrons (LUMIE) [70]. However, the ZEUS collaboration decided to use only the photon detector for the luminosity measurement.

Figure 4.9 shows the complete luminosity monitor system. The Bethe-Heitler photons with $\pi - \theta < 0.5$ mrad leave the beam-pipe through a Cu-Be window at $z = -92\,\mathrm{m}$ and are detected at $z = -107\,\mathrm{m}$ in the lead-scintillator calorimeter LUMIG. A position reconstruction with a precision $\approx 0.2\,\mathrm{cm}$ is provided by two layers of orthogonal 1 cm wide scintillator strips installed at a depth of $7X_0$ within the LUMIG. Hence, the electron beam profile can be determined and is used by HERA when optimising the beam. In front of the detector, a carbon-lead filter shields it against synchrotron radiation. At $z = -35\,\mathrm{m}$ there is the small electromagnetic lead-

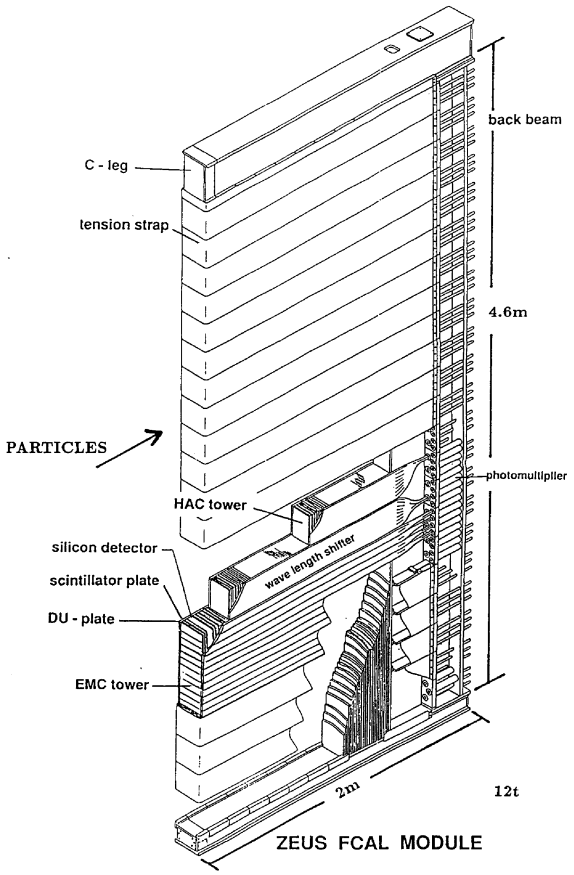

Figure 4.7: Cross section of an FCAL module. It is subdivided into one EMC and two HAC sections, which are divided further into towers.

scintillator calorimeter LUMIE, that detects electrons with energies between 7 and 20 GeV and scattering angles less than 5 mrad, which have been deflected by the HERA magnet system.

The measured photon rate has to be corrected for background events originating from Bremsstrahlung processes with residual gas molecules. The empty proton bunches paired with electron bunches are used to estimate this background.

The accuracy of the luminosity measurement, which depends on the beam conditions, is about 2% for the 1998–2000 running period.

4.2.4 The C5 Counter and the Veto Wall

The C5 counter is a scintillator based particle counter located at the collimator "C5" at $Z = -3.15\,\mathrm{m}$. The time measurement of the C5 counter is used obtain the mean vertex position in the z direction.

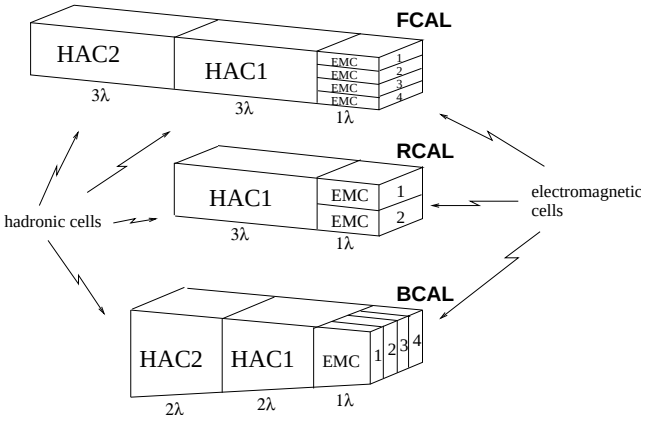

Figure 4.8: The tower structure of the uranium calorimeter. λ is the nuclear interaction length ($1\lambda \approx 25X_0$).

The veto wall is a iron plate of $8 \times 8\,\mathrm{m}^2$ at $Z = -7.4\,\mathrm{m}$. On both sides of this wall scintillators are used to detect background events.

Both detectors are mainly used to suppress non-*ep* background.

4.2.5 The Trigger and the Data Acquisition System

During data taking the predominant task is to find interesting signal events in a far greater number of uninteresting background events. For the huge amount of data to be processed and stored, this decision has to be taken "online", during the process of data taking itself. This is the purpose of triggers.

At the HERA interaction points the electron and proton bunches cross with a rate of 10.4 MHz. In some of these bunch crossings an *ep*-interaction takes place. The event measurements, containing information from about 250000 readout channels, can be put onto hard disks with a rate of about 5 Hz. This implies that only the most interesting events can be written to tape. On the other hand, the rate of detectable signals in the detector components is dominated by non-*ep*-events like the interaction of the proton beam with residual gas in the beam-pipe or – less frequently – beam halo interactions, cosmic ray events and electron beam gas interactions. These amount to a rate of the order 10 – 100 kHz. The ZEUS trigger system was designed to perform a good separation of signal and background events under these conditions.

It consists of three stages, the first, second and third level trigger (FLT, SLT and TLT shown in Fig. 4.10). In order to keep the dead-time low, the detector components store their data in hardware buffers or pipelines.

Firstly, the event information is processed at the local FLT of the components which send information to the gFLT – mainly the CTD and the CAL. The decision has to be sent to the gFLT within 3 µs. In order to satisfy this requirement the FLT

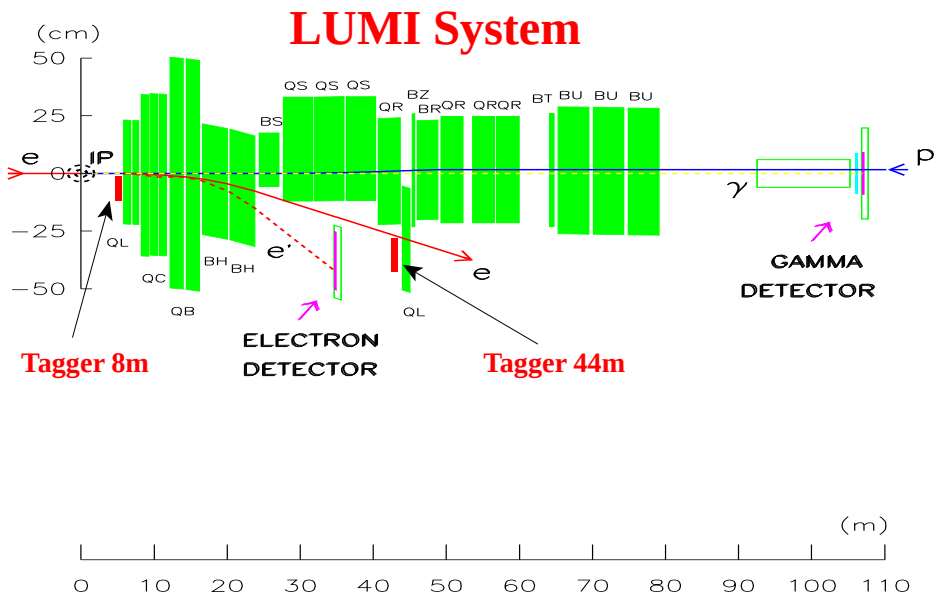

Figure 4.9: Layout of the luminosity measuring devices: the electron and the γ detector. Note the very different horizontal and vertical scales. The interaction point (IP), the nominal electron and proton beam lines (e–e, P–e) and the corresponding magnets are indicated. The 8 m and 44 m-taggers are shown as well.

is designed as a fast analogue hardware trigger. The GFLT combines this information and issues a trigger decision within another 2 µs. Only if this is positive, the components read out their pipelines and process the data further. The FLT reduces the event rate to below 1 kHz. The second level trigger has to reduce the event rate to less than 100 Hz. It uses a network of programmable transputer CPUs, designed for high network throughput. Again, the global SLT (GSLT) forms its decision from the local SLT information of the components.

After a positive GSLT, the components transmit their data to an event builder. This combines the data and makes it available to the TLT in the (ADAMO) database format, which is also used for offline processing and analysis. Hence, the TLT has information from all components, and a part of the offline reconstruction code can be used to analyse the events. After the TLT, the goal of lowering the event rate to ~ 5 Hz is reached.

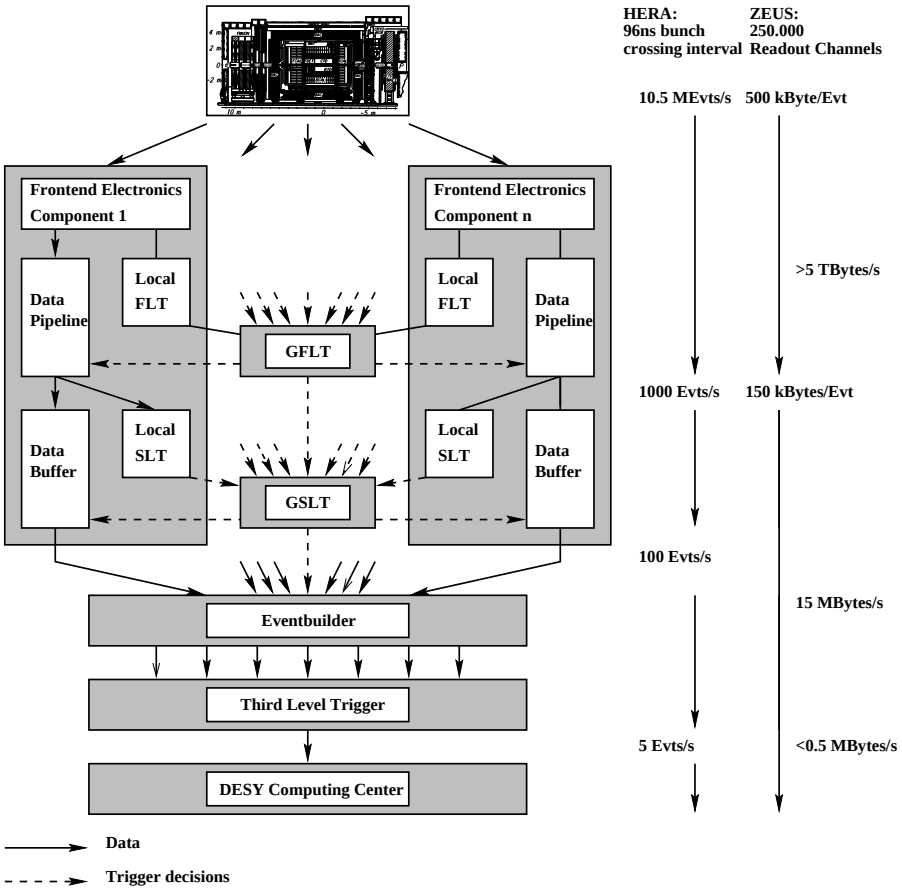

Figure 4.10: Schematic layout of the three-level-trigger and readout system of ZEUS.

Chapter 5

The Beam-Pipe Calorimeter

In this chapter the key detector for the D^* production at low Q^2 analysis is presented. The chapter starts with a motivation and continues with an overview of the BPC. Further the measurement of the energy and position of the scattered electron or positron with the BPC is described. The chapter ends with a discussion of the calibration of the BPC energy for the running period 1998–2000.

5.1 Measurements at low Q^2

The motivation to install a small-angle detector like the BPC at ZEUS was to get access to the fraction of electrons emerging at low scattering angles w.r.t. beam axis.

In DIS reactions, detecting the scattered electron at these small angles is equivalent to measure the reaction at low Q^2 (Section 2.1). This is the key to studying the transition region between deep-inelastic scattering and photoproduction.

There are two more possible methods to measure the electron for lower values of Q^2, but both have the disadvantage of reduced statistics and larger systematic uncertainties. One is the shifted vertex method, where the event vertex is shifted in the proton direction, so that the scattered electron can be detected in the RCAL at lower values of the polar angle θ. This was done only for a very limited period of runs in 1995 and 2000. Additionally, two RCAL modules were moved nearer to the beam-pipe.

The second method uses events, where an initial-state radiation photon is seen in the LUMIG detector. The photon lowers the ep-CMS energy, and thus the same scattering angle implies lower values of Q^2. However the statistics is reduced due to the limited ISR probability and large systematic uncertainties arise.

The BPC measures Q^2 in low-Q^2 events, when the electron escapes through the beam-pipe windows in the RCAL direction [71, 72]. In this region, any other reconstruction method suffers from a very poor resolution [33, 73]. Thus, it is necessary to measure well the scattered electron.

5.2 The BPC in ZEUS

In 1995 the BPC was installed to measure energy and position of the scattered electron at very high values of the polar angle, 18 mrad $< \theta <$ 32 mrad (Fig. 5.1). It consists of two modules, one on the south side and one on the north side of the beam-pipe (Fig. 5.2). The backward beam-pipe has two exit windows at $Z = -249.8$ cm in

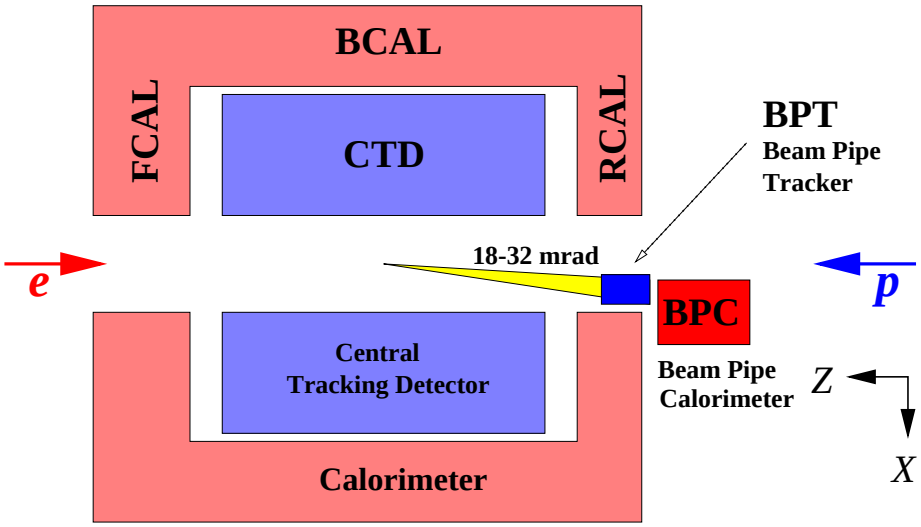

Figure 5.1: Schematic Z-X view of the ZEUS detector, indicating the position and angular acceptance of the BPC. The angles are determined by a window in the beam-pipe where the electrons can escape. Located in front of the BPC is the BPT detector, that provided tracking information of the scattered electron in the 1995 running period.

front of the BPC modules. They are made of 1.5 mm thick aluminium, corresponding to a very small radiation length of 0.016 X_0. Their dimensions in X and Y are defined by the surrounding RCAL modules. These are responsible for the effective fiducial areas of the BPC modules. The space for the exit window in front of the BPC South module is significantly smaller, resulting in a very small fiducial area.

The readout electronics of the RCAL and BPC modules constrain the dimensions of the two BPC modules. The modules are both 13.8 cm in Y and 16.0 cm in Z, but of different size in X (North 13.8 cm, South 9.8 cm). Their design is shown in Figure 5.3. They consist of 26 plates of tungsten alloy (3.5 mm thick) and alternating layers (2.6 mm thick) of scintillator material. The overall radiation length of 24 X_0 provides sufficient longitudinal shower containment for electromagnetic showers up to the maximum energy of 27.6 GeV. The scintillator layers are transversely divided into 7.9 mm wide optically decoupled fingers. Their orientation alternates between the X- and Y-direction. Both BPC modules have 16 fingers in Y. In X, BPC North has 15 and BPC South 11 fingers. The light of all fingers with the same orientation lying

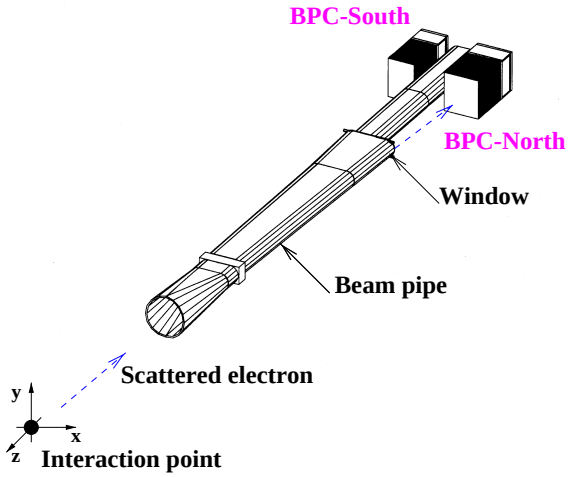

Figure 5.2: The backward beam-pipe and the BPC modules North and South. Two exit windows for the scattered electron reduce the amount of material to be traversed to a minimum.

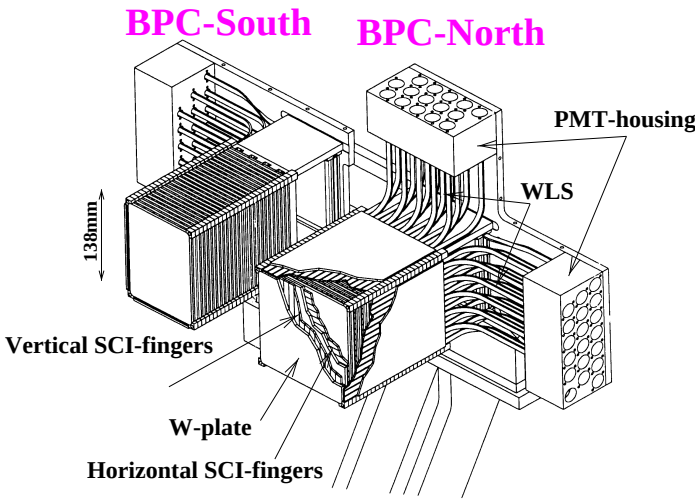

Figure 5.3: The BPC North and South modules. The scintillator fingers, wavelength shifters (WLS) and photomultiplier tube (PMT) housings are indicated. The beam-pipe separates both modules and the RCAL readout electronics surrounds them completely.

behind each other in the longitudinal direction (called a "strip") is collected together by means of wavelength shifters into one photomultiplier tube (PMT) corresponding to one readout channel. Hence, the BPC is insensitive to the longitudinal shower profile, but the transverse position of a shower can be determined.

From the BPC PMT pulses, a charge fraction of approximately 10% is used for a BPC first level trigger. The remaining charge is analysed by BPC analogue cards. If a positive GFLT decision arrives, event information is sent to digital cards, where (uncalibrated) energy and time are reconstructed by digital signal processors (DSPs). This information is available for the reconstruction.

Important BPC parameters are given in Table 5.1. More details on the detector and the trigger can be found in [72].

BPC parameters		
Energy resolution	$17\%/\sqrt{E/\mathrm{GeV}}$	(1)
Position resolution	$\approx 0.22\ \mathrm{cm}/\sqrt{E/\mathrm{GeV}}$	(2)
Depth	$\approx 24\,\mathrm{X}_0$	(3)
Molière radius	≈ 13 mm	(3)
Linearity	$\leq 1\%$	(3)
(1) from test beam measurements		
(2) from 1997 data [74]		
(3) from design		

Table 5.1: Some BPC parameters. The position determination has additional biases from other sources like alignment amounting to 0.1 cm.

Between the beam-pipe exit window and the BPC North, a tracking device, the Beam-Pipe Tracker (BPT), was installed. It consists of five silicon micro-strip detectors mounted orthogonal to the Z-axis. It is designed in order to improve Z-vertex reconstruction, reduce photon background and enhance the position measurement of the BPC to improve especially the Q^2 resolution. As the Q^2 resolution of the BPC is sufficient (Section 6.7.1) for this analysis only the BPC energy and position is used to measure the scattered electron here.

The BPC South module is only used for alignment purposes as it has a substantially reduced active area. It is not designed to be used in physics analyses, therefore the following chapters will concentrate on the BPC North module. In the following BPC will always denote the BPC North.

5.3 BPC Position Measurement

The measurement of the impact position of the electron in the BPC is needed for a precise reconstruction of Q^2.

The BPC is segmented transversely into X and Y fingers as discussed in Section 5.2. Since no information of the longitudinal energy deposition in the BPC is available, only the X and Y position (X_{BPC},Y_{BPC}) of electrons detected in the BPC can be calculated. This is done at Z^e_{BPC}, the effective depth, of the electromagnetic shower produced by initial electron in the BPC. Z^e_{BPC} is from the measured energy and a shower simulation [75].

The reconstruction of the X^e_{BPC} and Y^e_{BPC} position at the effective depth is done using the energy imbalance between strip energies. This method uses a fit of the energy imbalance of the most energetic X and Y strips an its neighbours to extract the X^e_{BPC} and Y^e_{BPC} position with a spatial resolution of less than 1 mm for energies greater than 4 GeV [74].

The impact position $(X^e_{BPC}, Y^e_{BPC}, Z^e_{BPC})$ is extrapolated in the vertex direction to the front face of the BPC and denoted as (X, Y, Z) in the following.

5.3.1 Survey for the 1998–2000 Running Period

After the 1998 shutdown a survey of the BPC was performed in order to determine the absolute position in the ZEUS coordinate system. The method of the survey was identical to the method used after the 1995 and 1997 shutdowns [33]. With optical devices the positions of the BPC modules were determined relative to the compensator magnet. The position of the magnet was determined relative to the ZEUS coordinate system.

The result of the survey refers in X to the position of the inner edge of the first X-finger. In Y it refers to the edge between the 8th and 9th Y-finger and in Z to the BPC front face. The overall precision is estimated to be 0.1 cm. Also the angles of the BPC edges w.r.t. ZEUS coordinate system were determined and found to be negligibly small.

The result of the 1998 survey is

$$\begin{aligned} X^0_{BPC} &= 4.31 \pm 0.03(\text{stat}) \pm 0.06(\text{sys})\,\text{cm} \\ Y^0_{BPC} &= 0.01 \pm 0.03(\text{stat}) \pm 0.06(\text{sys})\,\text{cm} \\ Z^0_{BPC} &= -293.70 \pm 0.03(\text{stat}) \pm 0.06(\text{sys})\,\text{cm} \end{aligned}$$

These position values were used in the standard ZEUS offline BPC reconstruction software (BPRECON) for this analysis.

5.3.2 BPC Fiducial Area

One of the most important cuts in this analysis is the BPC fiducial area cut. This cut is applied because the energy deposition of an electromagnetic shower has to be

contained inside the BPC. Thus, a small gap between the lateral position of the shower and the edge of the BPC is needed. Events detected in this gap suffer from energy leakage and therefore have a reduced BPC energy. To avoid this systematic effect a fiducial area cut on the lateral shower position is applied. For the 1997 F_2 analysis the cut was chosen to be [33]:

Data and MC							
(5.2 cm	$< X <$	9.3 cm)	$\wedge$	(−2.3 cm	$< Y <$	2.8 cm)	$\wedge$
$(X - Y$	$<$	10.7 cm)	$\wedge$	$(X + Y$	$<$	11.2 cm)	

The event sample of the 1997 analysis was much larger than in this analysis because an inclusive *ep* trigger was used. The fiducial area was enlarged as much as possible in order to improve the statistics of this analysis (Fig. 5.4). The impact positions are in a D-shaped area given by the escape window of the beam-pipe. There is a slightly higher occupancy at X between 4.8 cm and 5.0 cm than in the rest of the BPC. The significantly enlarged fiducial area cut for this analysis can be found in the following table:

Data			Monte Carlo		
5.0 cm	$< X <$	10.0 cm	5.0 cm	$< X <$	10.0 cm
−2.5 cm	$< Y <$	3.5 cm	−2.9 cm	$< Y <$	3.1 cm
$X - Y$	$<$	11.2 cm	$X - Y$	$<$	11.6 cm
$X + Y$	$<$	12.2 cm	$X + Y$	$<$	11.8 cm

Comparing Data and MC for the 1998–2000 running periods a shift in the Y-position of 0.4 cm is found (see also [76]). Therefore the fiducial area cut applied to the MC was shifted correspondingly in Y to cut on the same area and the electron scattering angle reconstructed with the BPC was corrected for MC.

5.4 BPC Time and Shower Width Reconstruction

The reconstructed time, T_{BPC}, and the shower size, Σ_{BPC}, are used to reject background events (see Section 6.6).

T_{BPC} is reconstructed from the energy weighted time, t_i, of the single scintillator strips taken from the DSPs. T_{BPC} has the order of microseconds and is the time between the *ep*-reaction and the appearance of a signal on the DSPs. The major part of this time is consumed by reading out the photomultipliers. As the timing between the HERA clock, which defines when the *ep*-reaction has taken place, and the GFLT timing can shift, one is not interested in T_{BPC}, but in BPC timing distribution per run, $\overline{T_{BPC}}$, and the time residual $T^{res}_{BPC} = \overline{T_{BPC}} - T_{BPC}$ to reject background events. T^{res}_{BPC} has the order of nanoseconds because the constant but large signal propagation and processing delay in the readout electronic is subtracted in the residual.

The shower width, Σ_{BPC}, is taken from the second moments of the lateral shower distributions in X and Y using a logarithmically-weighted energy method [72].

5.5 BPC Energy Measurement

The BPC energy calibration is important for the D^* production at low Q^2 analysis presented here. The measured BPC energy is used for the reconstruction of the kinematic variables in the electron method and therefore influences the event selection. A different energy scale in data and MC may result in event migration.

The energy readout of the DSPs during data taking is only a first approximation to the true BPC energy. It is corrected for strip-to-strip gain variations, energy leakage out of the calorimeter, light attenuation inside the scintillators and non-uniformities caused by the 0.1 mm gaps between adjacent scintillators as described in [74]. These corrections are implemented in BPRECON and therefore used for this analysis.

The built-in corrections in the reconstruction software were optimised for the analysis of 1995–1997 data and thus do not take into account the energy degradation before and during the 1998–2000 running period. This BPC energy which is corrected using the 1995–1997 correction but not the 1998–2000 corrections is called E_{BPC}^{uncorr} here. For this analysis a recalibration of E_{BPC}^{uncorr} is performed as described in the next section.

5.6 Energy Calibration for 1998–2000

In the running periods 1998–2000 the energy response of the BPC decreased significantly due to radiation damage of the BPC scintillators. This radiation damage is mainly caused by hard synchrotron radiation, which is most intense at the BPC position very close to the ZEUS beam-pipe.

In this section the effects of position and time dependence of the energy response are studied. The results are used to correct the BPC energy degradation.

5.6.1 Expected and Measured Energy

Four-momentum conservation leads to the definition of energy-momentum difference along the z-axis of the event, δ_{BPC}. This quantity can be used as an estimator for the calibration of the BPC energy and to clean the analysis event sample from PhP background events. One can write

$$\delta_{BPC} = (E - p_z)_{e'} + \delta + (E - p_z)_{P'} \tag{5.1}$$

where e' denotes the final electron state, P' the proton (remnant) and $\delta = \sum_i (E - p_z)_i$ the final NC event state with index i running over all UCAL clusters. This equation is true, if the energy of the electron is detected in the BPC and the energy of the rest of

the final state is detected in the UCAL. In this case $(E-p_z)_{e'}$ can be calculated using the BPC energy, E_{BPC}, and the angle of the scattered electron w.r.t. the beam-axis, Θ_{BPC}, measured in the BPC:

$$(E-p_z)_{e'} = 2E_{e'} = E_{BPC}(1-\cos(\Theta_{BPC}) \ , \tag{5.2}$$

neglecting the mass of the scattered electron.

Regarding the initial state we can evaluate equation (5.1) to $\delta_{BPC} = (E-p_z)_e = 2E_e = 55.2\,\text{GeV}$. The right side can be simplified as $(E-p_z)_{P'} \approx 0$. Using Eqn. (5.1) and Eqn. (5.2) one can define the "missing energy":

$$\begin{aligned} E_{miss} &= 2E_e - E_{BPC}(1-\cos(\Theta_{BPC})) - \delta \\ &= 55.2\text{GeV} - \delta_{BPC} \ . \end{aligned} \tag{5.3}$$

In the following this quantity is used to correct the energy of the BPC. An ideal detector would give an unbiased energy $E_{miss} = 0$ for a NC DIS event. If the resolution is not negligible, as in this analysis, the mean missing energy $\langle E_{miss} \rangle$ should be 0 with a spread given by its resolution. In the ZEUS detector there are always a few particles which escape partially or completely undetected, e.g. through small gaps in the region between the RCAL and the BPC, and give a bias to E_{miss}. Therefore $\langle E_{miss} \rangle$ is not even 0 for MC. However, the E_{miss} distribution for data and MC should have approximately the same mean and shape.

The energy correction for 1998–2000 was iterated until the E_{miss} distributions for data and MC showed a reasonable agreement (Fig. 5.5). The resolution in data is somewhat worse than in MC mainly due to the radiation damage. The calibration procedure will be discussed in detail in the next sections.

5.6.2 Event Selection

In order to study the energy and time dependence a data sample of D^* mesons with the same properties[1] as the final sample for the D^* production at low Q^2 analysis is needed. Ideally it should have a much higher statistics and shouldn't contain the final D^* mesons of the D^* production at low Q^2 analysis.

The calibration sample uses the same inclusive NC D^* and BPC triggers as the final sample. A description of these triggers can be found in Section 4.2.5 and 6.2. To enrich the data sample only loose selection cuts on the D^* topology and kinematics are applied (Appendix A). The BPC fiducial cut is not applied, thus the calibration is done for the whole active area of the BPC.

After these selection cuts the number of D^* candidates in the calibration sample is about 100000. Therefore the contribution of the events of the final sample of the D^* production at low Q^2 analysis, around 700, can be neglected.

[1] All selected events have a scattered electron in the BPC and a D^* candidate is found. The additional final state particles are detected in the CTD and the CAL.

5.6.3 Y-Position Dependent Energy Calibration

The radiation damage is not homogeneously distributed over all BPC fingers but has a special structure which is presented for the Y distribution in Figure 5.6 and for the X distribution in Figure 5.7. One would expect an energy degradation slightly increasing towards the beam-pipe, i.e. to lower X values, because the radiation which causes the damage is more intense here. Surprisingly, this behaviour is not observed. However there is a maximum in the energy degradation around $Y \approx -1\,\mathrm{cm}$.

To correct the Y-dependency the shape of the average of E_{BPC} was fitted using three linear functions in three Y regions as indicated by the lines in Figure 5.6. The functions $e_1(Y)$, $e_2(Y)$ and $e_3(Y)$ obtained by these fits (see Table 5.2) are used in the following way to calibrate the energy:

$$E^*_{BPC} = E^{uncorr}_{BPC}(Y) * \left(1 + \frac{E^0_{BPC} - e_i(Y)}{E^0_{BPC}}\right) , \tag{5.4}$$

where i has to be chosen w.r.t. Y and $E^0_{BPC} = 26.5\,\mathrm{GeV}$ is the mean BPC energy for the MC sample. No corrections were applied to the $E^{uncorr}_{BPC}(X)$ distribution.

Function Index	Range	Correction Function
1	$Y \leq -1.1\,\mathrm{cm}$	$e_1(Y) = 18.0\,\mathrm{GeV} - 3.4\frac{\mathrm{GeV}}{\mathrm{cm}} \cdot Y$
2	$-1.1\,\mathrm{cm} < Y \leq -0.5\,\mathrm{cm}$	$e_2(Y) = 26.5\,\mathrm{GeV} + 4.4\frac{\mathrm{GeV}}{\mathrm{cm}} \cdot Y$
3	$-0.5\,\mathrm{cm} < Y$	$e_3(Y) = 24.5\,\mathrm{GeV} - 0.4\frac{\mathrm{GeV}}{\mathrm{cm}} \cdot Y$

Table 5.2: Correction functions extracted by linear fits to the average of $E_{BPC}(Y)$.

After the correction of the Y-dependent part of the energy degradation the energy distribution E^*_{BPC} is distributed homogeneously in X and Y over the whole fiducial area as shown in Fig. 5.7. But the X- and Y-averaged BPC energy shows still a time dependence and therefore $E^*_{BPC} = E^*_{BPC}(Runnr)$.

5.6.4 Calibration of the Run Dependent Energy Response

The BPC energy degradation worsened continuously during the 1998–2000 running period. In order to visualise this effect the mean missing energy $\langle E_{miss} \rangle$ for groups of 30 runs is plotted against the run number (Fig. 5.8). To first order the time dependence of $\langle E_{miss} \rangle$ can be described by a straight line [76]. Therefore a linear correction factor $k(Runnr)$ which increases with the run number can be defined:

$$k(Runnr) = 0.98 + 0.08 \cdot \frac{Runnr - 30000}{7000} \tag{5.5}$$

Applying this correction to $E^*(Runnr)$ one obtains the calibrated BPC energy E_{BPC} (Fig.5.8), which is used in this analysis:

$$E_{BPC} = E^*_{BPC}(Runnr) \cdot k(Runnr) \tag{5.6}$$

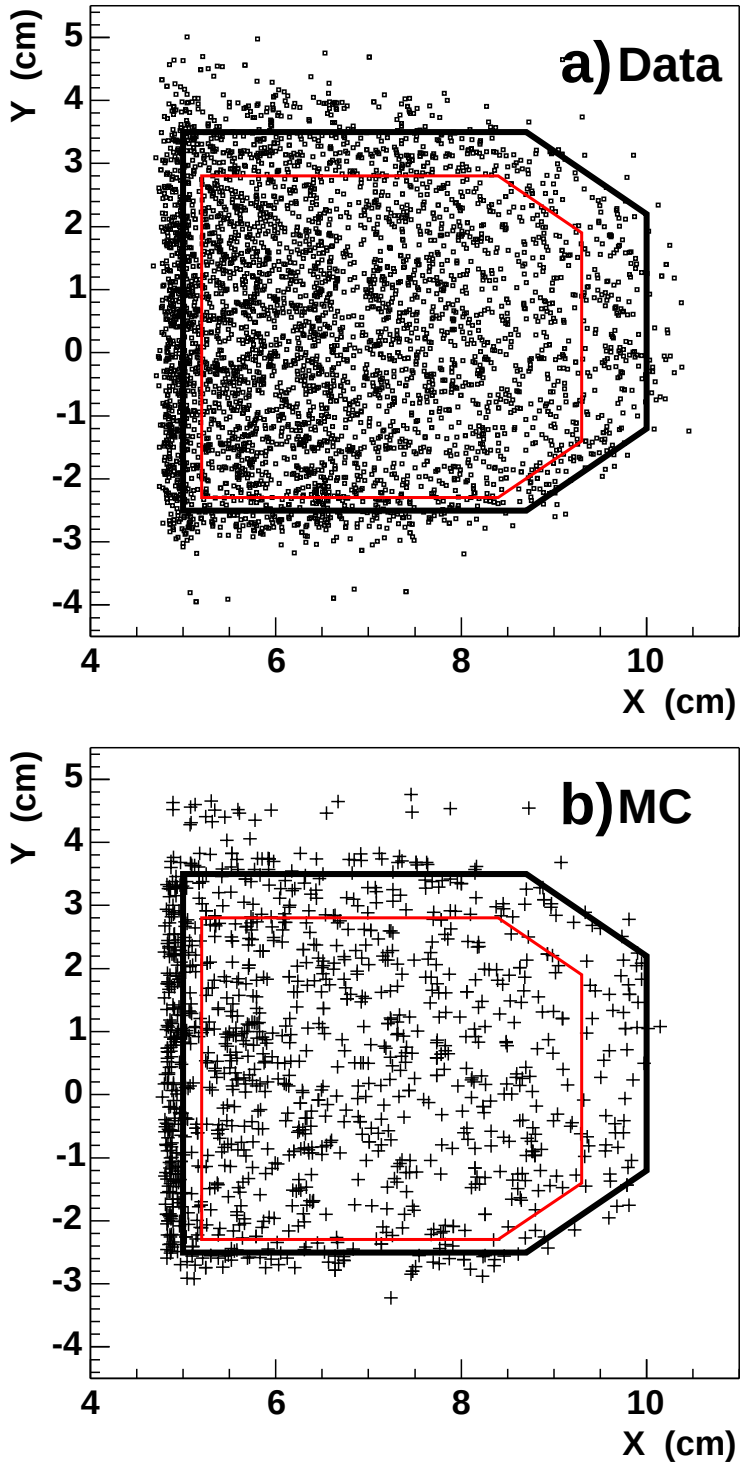

Figure 5.4: Reconstructed impact position of scattered electrons in the BPC for a) data and b) Monte Carlo. These event samples were obtained by using the BPC trigger and requiring $E_{BPC} > 4\,\mathrm{GeV}$. The area within the outer lines is the fiducial area of the BPC used in this analysis. The fiducial area of the 1997 analysis is indicated by the inner thinner lines.

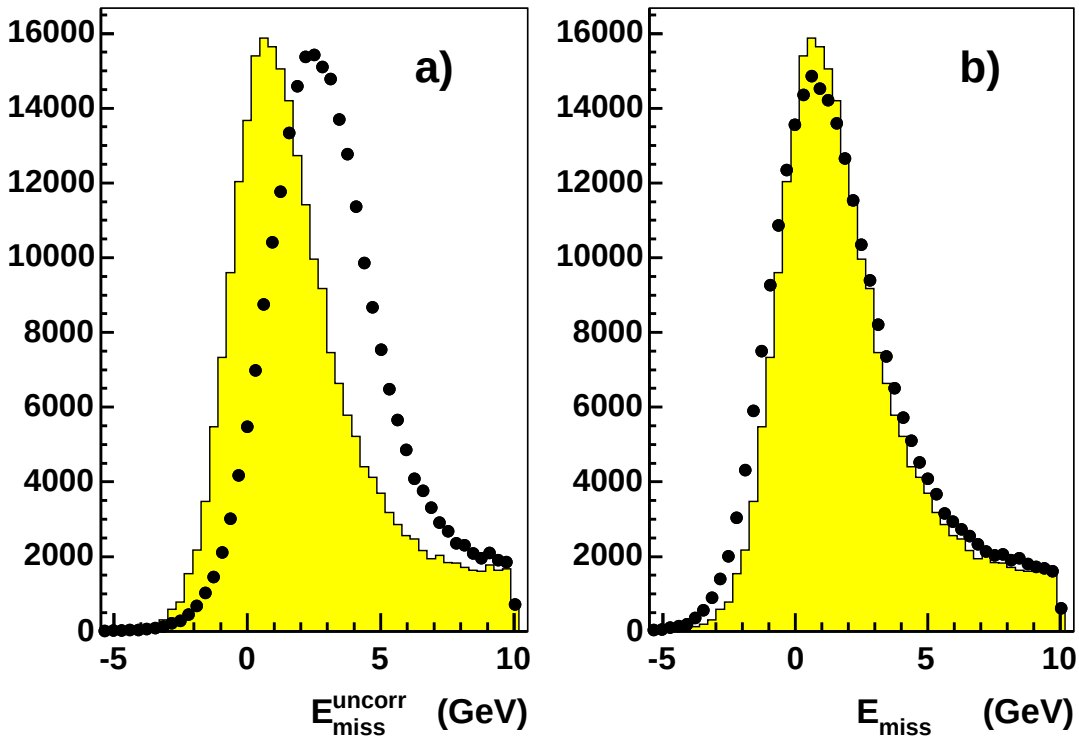

Figure 5.5: Distributions of the missing energy E_{miss} for the calibration sample a) before and b) after applying the 1998–2000 corrections to the BPC energy. The data are represented by points. The filled area is the MC distribution normalised to the same area as the data distribution. The rapid fall at 10 GeV is an effect of the δ selection cut applied on the calibration sample (see Section 5.6.2).

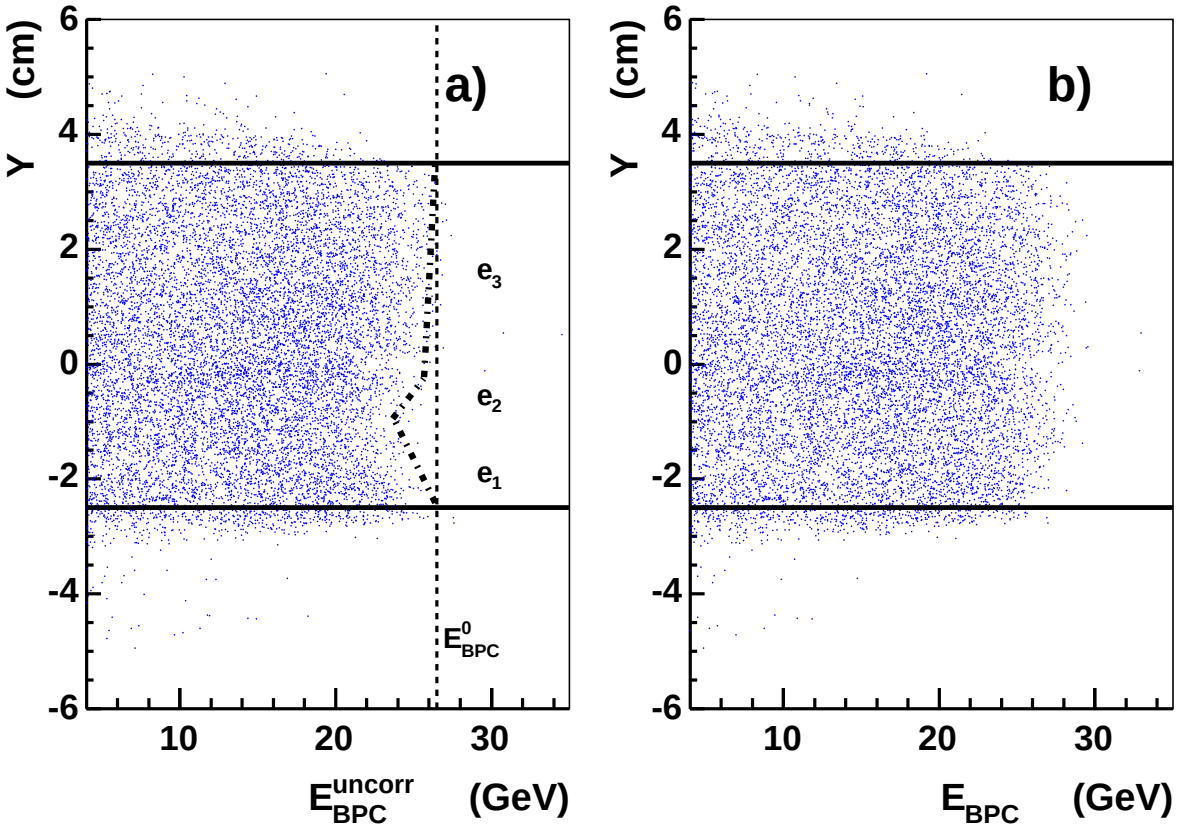

Figure 5.6: Y-dependence of E_{BPC} a) before and b) after applying the 1998–2000 corrections on the calibration sample. The dotted lines e_1, e_2 and e_3 indicate the linear fits for the calibration of $E_{BPC}(Y)$. The solid lines indicates the limits of the fiducial area of the BPC used in this analysis (see Section 5.3.2).

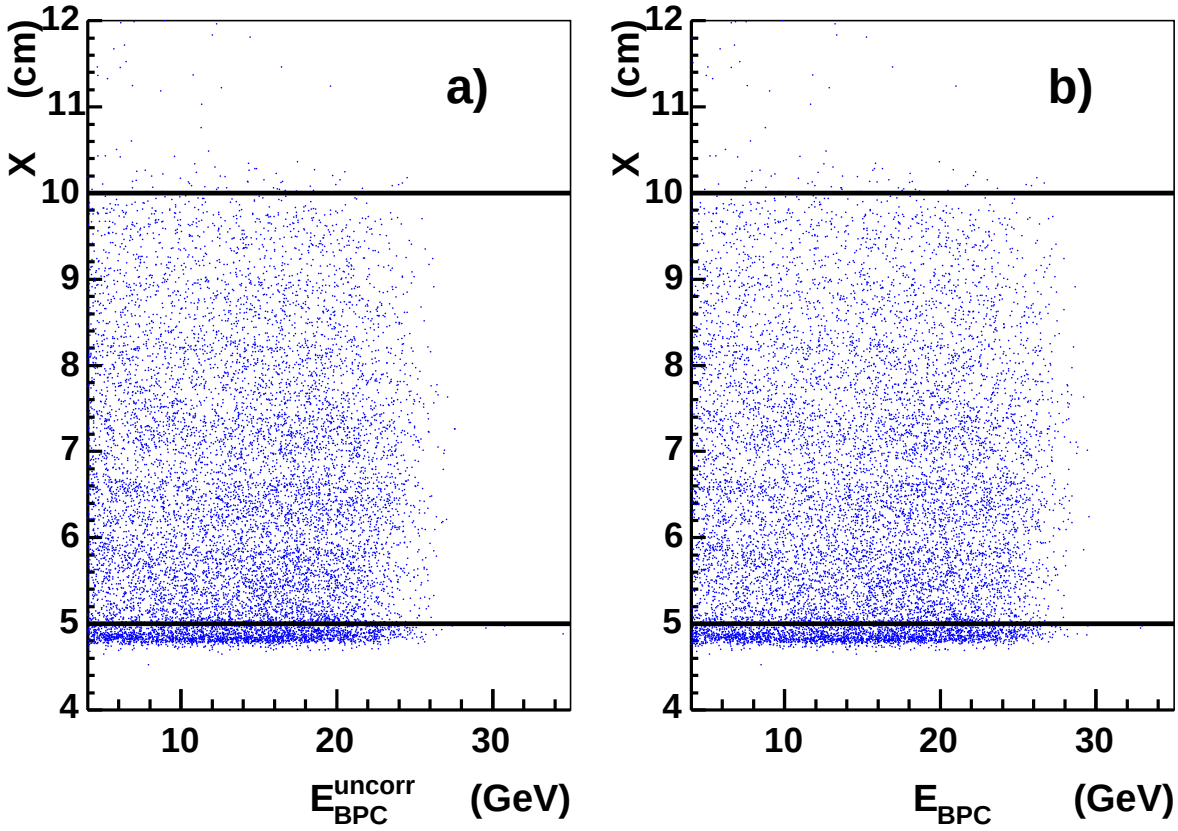

Figure 5.7: X-position dependence of E_{BPC} a) before and b) after applying the 1998–2000 corrections to the calibration sample. The solid lines indicates the limits of the fiducial area of the BPC used in this analysis (see Section 5.3.2).

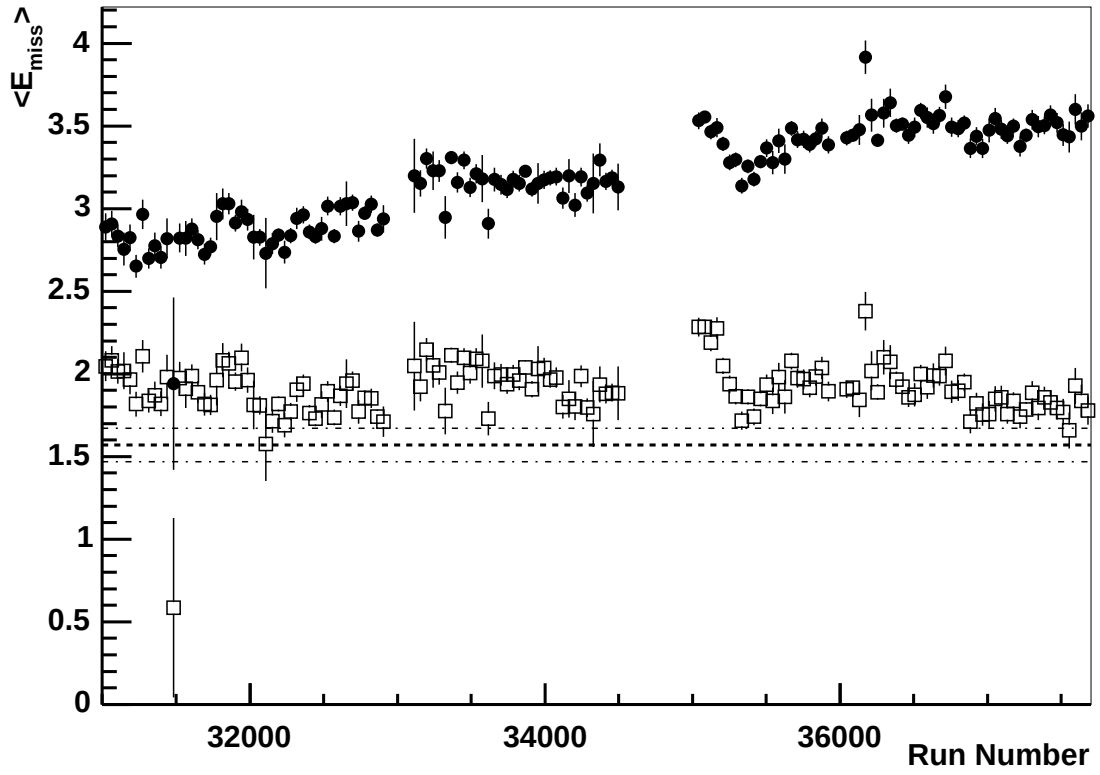

Figure 5.8: Time dependence of the mean missing BPC energy, $\langle E_{miss} \rangle$, with (open rectangles) and without (filled circles) the 1998–2000 calibrations, $\langle E_{BPC}^{uncorr} \rangle$. Each entry is the mean over 30 runs and the error bars are the standard error on $\langle E_{miss} \rangle$ and $\langle E_{BPC}^{uncorr} \rangle$. The dashed line is $\langle E_{miss} \rangle$ of the MC sample, the dotted-dashed lines indicates the standard error on $\langle E_{miss} \rangle$ of the MC sample.

Chapter 6

D^* Meson Production at Low Q^2

The goal of the analysis presented in this chapter is to measure the cross-section of D^* production at low Q^2 using the BPC of ZEUS as motivated in Chapter 2. For this measurement a sample of events containing a D^* together with an identified and well-measured electron in the BPC is required.

The analysis follows the usual steps of such an high-energy physics analysis: the selection of the desired event class, the extraction of the signal and the correction for the influence of the detector. At the end the total D^* production cross-section is presented as well as the differential cross-sections in the variables Q^2, y, $p_t(D^*)$ and $\eta(D^*)$. These cross-sections will be compared with theoretical predictions from NLO calculation in the next chapter.

6.1 The Analysed $D^{*\pm}$ Meson Decay

The decay channel investigated in this analysis is

$$\begin{aligned} D^{*+} &\rightarrow D^0 + \pi_s^+ \\ &\rightarrow K^- + \pi^+ + \pi_s^+ \end{aligned}$$

and the charge-conjugate channel[1]. Due to the small mass difference between the D^* and the D^0 meson, $\Delta M = M(D^*) - M(D^0) = 145\,\text{MeV}$, the momentum of the pion in the D^* rest frame is very low, hence the subscript "slow" on π_s. The mass difference ΔM is measured in this analysis instead of the mass of D^* or D^0 itself to increase the resolution.

The decay of the $D^{*+} \rightarrow D^0\pi_s^+$ has a branching ratio of $\approx 68\%$. The subsequent decay $D^0 \rightarrow K^-\pi^+$ has a branching ratio of only 3.85%, which gives for the whole decay process a branching ratio of $\approx 2.6\%$[2].

[1] In the following the charge-conjugate channel is always implied

[2] There are of course many more possible D^* decays, e.g. $D^{*+} \rightarrow K^-\pi^+\pi^+\pi^-\pi^+_{(s)}$ or $D^{*+} \rightarrow K^-\pi^+\pi^+\pi^0$. The first decay has a larger branching ratio but suffers from increased combinatorial

6.2 Trigger Preselection of the Data Sample

The trigger preselection is done by demanding that the ZEUS heavy flavour BPC trigger (HFL-BPC) has fired during data taking.

Additionally, events taken when the ZEUS heavy flavour photoproduction (HFL-PHP) trigger has fired are also selected in order to study the efficiency of the HFL-BPC trigger in the 1998–2000 running period. The reason to choose the HFL-PHP trigger for that purpose is that events triggered by the HFL-BPC trigger are an independent subset of events triggered by the HFL-PHP. The details will be described in the following sections.

6.2.1 Event Topology

Events which pass the trigger preselection have some general properties which are defined by the signal class of the D^* production at low Q^2 analysis. One is the presence of three tracks from the interaction point of the event which can be combined to a D^* candidate as described in Section 6.3. Additionally a reconstructed electron in the BPC is needed as well as some amount of energy in the uranium calorimeter from the hadronic final state. Furthermore the absence of a scattered electron in the the uranium calorimeter is used as a veto condition to reduce DIS background events with $Q^2 > 2\,\mathrm{GeV}^2$. A typical D^* event of the low Q^2 signal class is shown in Figure 6.1.

6.2.2 HFL-BPC Trigger

In Section 4.2.5 the ZEUS trigger system was introduced. Different physics filters are used at each trigger level and each physics filter is designed to trigger events from a certain process. For the running period 1998–2000 there was a dedicated hardware trigger to select events with an electron in the BPC and tracks in the CTD which can be combined to a D^* candidate.

This is the first analysis which benefits from the implementation of this trigger. The HFL-BPC trigger used in this analysis consists of the HFL-FLT Slot 34, the HFL-SLT slot 8 and the HFL-TLT slot 14 (Fig. 6.2). If a positive decision is given at each of these trigger slots the event is selected. The trigger conditions at each trigger level are described below:

D^* + BPC First Level Trigger (HFL-FLT34)

If the following simple conditions are fulfilled, the HFL-FLT34 slot "fired":

- Localised energy deposition detected in BPC:
  This indicates that an electron candidate was found in the BPC.

background. The second has a neutral particle in the final state which make the reconstruction more difficult.

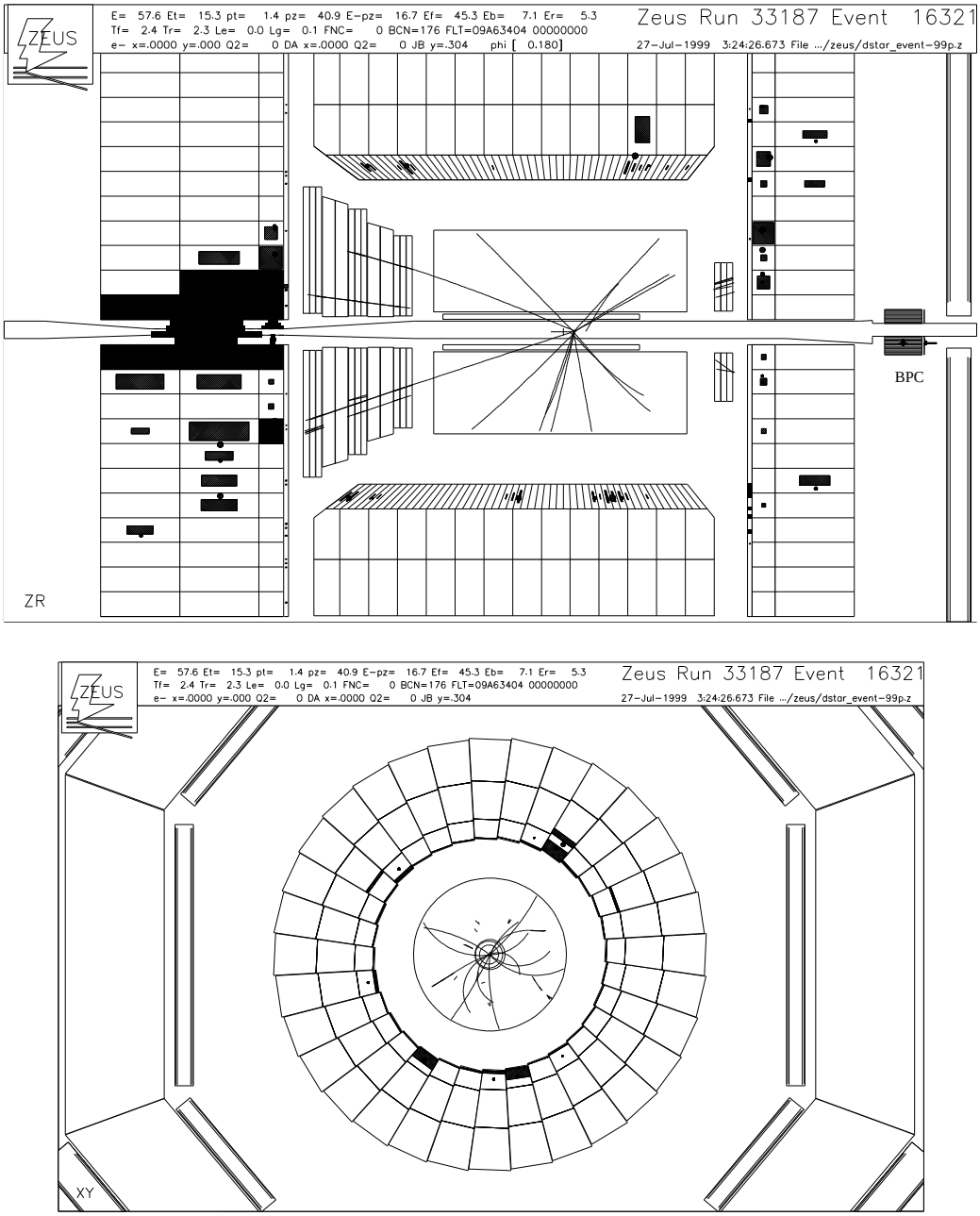

Figure 6.1: A typical ZEUS low Q^2 DIS event. The event display on top shows a Z-R projection through the ZEUS detector while the event display at the bottom is the projection in the plane perpendicular to the beam which includes the event vertex. In this event the D^* reconstruction has found one candidate with the correct charge by combining the 4-vectors of three CTD tracks as described in Section 6.3. The BPC has detected an electron with $E_{BPC} = 23.4\,\text{GeV}$ and additionally no electron was found by the electron finder of the CAL (Sinistra). In the FCAL close to the beam-pipe the energy deposit of the proton remnant, which has been broken up, is indicated by filled rectangles with areas proportional to the measured energy in each EMC/HAC cell.

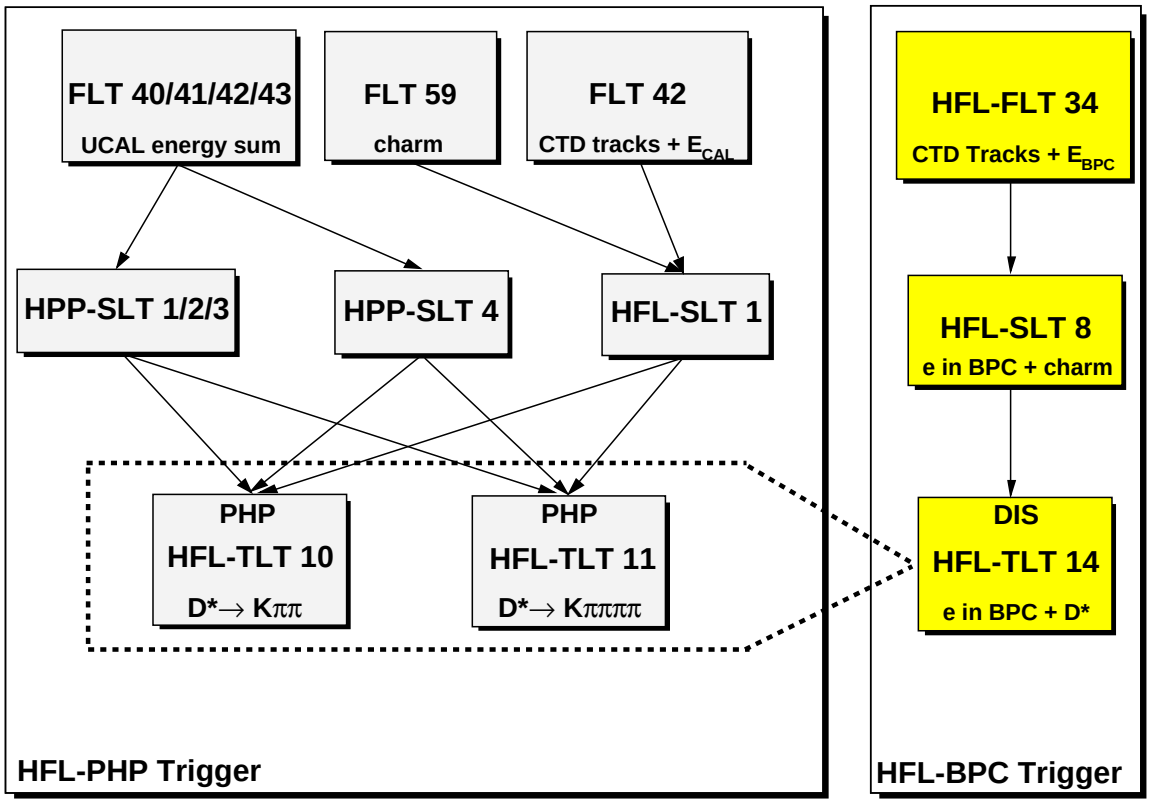

Figure 6.2: An overview sketch of the ZEUS HFL-PHP and HFL-BPC triggers as implemented in the 1998–2000 running period. The arrow-like area indicates that events triggered by the HFL-BPC trigger are a sub-sample of the HFL-PHP trigger as the trigger conditions to find a D^* pre-candidate are the same for both of these triggers. The text on the bottom of the boxes is a rough description of the event attribute or variable used by the corresponding trigger slot. Details are described in the text.

- $E_{CAL} > 4972\,\text{MeV}$ and no. of CTD tracks ≥ 5 in the CTD:
  The amount of energy is sufficient to find an D^* in the hadronic final state and the number of charged CTD tracks is sufficient to combine them to a $D^* \to K\pi\pi$ or $D^* \to K\pi\pi\pi\pi$ candidate.

Some additional trigger conditions prevent the HFL-FLT34 from firing, so called vetoes:

- The C5 and the veto wall (Section 4.2.4) component signals that the reaction has taken place outside the ZEUS interaction region.
- The SRTD detects a scattered electron and thus the electron detected in the BPC is probably a fake electron.

D^* + BPC Second Level Trigger (HFL-SLT8)

On the next level of the event triggering a simplified tracking has been done and more precise variables can be used to in order to select the desired events. Signal events of this analysis have to fulfil the following conditions:

- HFL-FLT34.
- An ep-vertex[3] has been reconstructed.
- The transverse calorimeter energy is $E_T := \sum_i E_i \sin\theta_i > 4\,\text{GeV}$; the sum is over all UCAL cell energies, E_i, and their angle, θ_i, ignoring the two inner rings of FCAL.
- The number of vertex matching CTD tracks ≥ 2.
- The number of found CTD tracks ≥ 5.
- The number of found CTD tracks ≤ 16 or the sum of two highest-p_t tracks $> 1.2\,\text{GeV}$.

D^* + BPC Third Level Trigger (HFL-TLT14)

At the last trigger level the full reconstruction has been done, thus all reconstructed event variables can be used to select physics events. The conditions for the HFL-TLT14 trigger to fire are:

- HFL-SLT8.
- HFL-TLT10 ($D^* \to K\pi\pi$, see Section 6.2.3) or
  HFL-TLT11 ($D^* \to K\pi\pi\pi\pi$) has fired.

[3]The reconstruction of an ep-vertex is done using CTD tracks in an iterative procedure. The vertex finding algorithm is described in detail in [77].

6.2.3 HFL-PHP Trigger (HFL-TLT10)

For the study of the HFL-BPC trigger efficiency the HFL-PHP trigger is used to preselect the event sample as it is known to have an efficiency ≈ 0.92 in the same kinematic region as considered in this analysis, but with a limited y range of $y < 0.7$ [78]. The event samples selected by both triggers have a large overlap, as the HFL-PHP trigger uses almost the same quantities and cuts as the HFL-BPC trigger. However, both triggers are implemented using different program codes are therefore independent.

The HFL-PHP trigger selects D^* events in photoproduction by the absence of the scattered electron in the uranium calorimeter without requiring of an electron in the BPC. The HFL-BPC trigger uses the filters of the HFL-TLT10 and HFL-TLT11 to select D^* candidates. As the HFL-PHP trigger has no veto condition on the BPC, events which are triggered by the BPC should also be triggered by the HFL-PHP trigger if they are also in the kinematic region of the BPC. The detailed conditions for the HFL-TLT10 to fire are the following:

- HFL-FLT40 $\vee$ 41 $\vee$ 42 $\vee$ 43 $\vee$ 59
- HPP-SLT1 $\vee$ 2 $\vee$ 3 $\vee$ 4 or HFL-SLT1[4]
- $-50 < Z_{vertex} < 50\,\text{cm}$
- $3 \leq$ No. of CTD tracks < 100
- $p_t(\pi_s) > 0.1\,\text{GeV}$
- $p_t(K, \pi) > 0.35\,\text{GeV}$
- $1.4 < M(D^0) < 2.2\,\text{GeV}$
- $\Delta M < 0.170\,\text{GeV}$
- $p_t(D^*) > 1.5\,\text{GeV}$

The trigger does not cut on the charge of the D^0 candidate, therefore wrong charge combinations are also triggered. The HFL-BPC trigger efficiency is defined in the following as the ratio:

$$\epsilon_{BPC} = \left.\frac{N(\text{HFL} - \text{PHP} \wedge \text{HFL} - \text{BPC})}{N(\text{HFL} - \text{PHP})}\right|_{\text{total visible kin. BPC region}} \tag{6.1}$$

where N is the number of events triggered with the condition in the argument. The evaluation of the efficiency is restricted to the *total visible region* of this analysis – i.e.

[4] All used subtriggers require a reconstructed ep-vertex, a certain amount of transverse energy in the UCAL and the absence of the scattered electron in the CAL. The amount of transverse energy and the number and momentum of the CTD tracks they cut on is varied in the different subtriggers.

the whole accessible kinematic BPC and D^* region after applying all analysis cuts (Section 6.6):

$$\begin{aligned} 0.05 < \quad & Q^2 & < 0.7\,\mathrm{GeV}^2 \\ 0.02 < \quad & y & < 0.85 \\ 1.5 < \quad & p_t(D^*) & < 9.0\,\mathrm{GeV} \\ & |\eta(D^*)| & < 1.5 \end{aligned}$$

Using the 1998–2000 data sample one obtains $\epsilon_{BPC} = 0.97 \pm 0.01$. The same is done for each kinematic bin (Section 6.7) of this analysis (Fig. 6.3). The HFL-BPC trigger efficiency is larger than 94% in all bins of the considered kinematic variables, except in the third $\eta(D^*)$ bin where also the statistics is low.

Due to the small dependency of the trigger efficiency on the kinematic variables, the effect of the trigger on the cross-sections is corrected assuming $\epsilon_{BPC} = 97\%$ to be constant in all analysis bins.

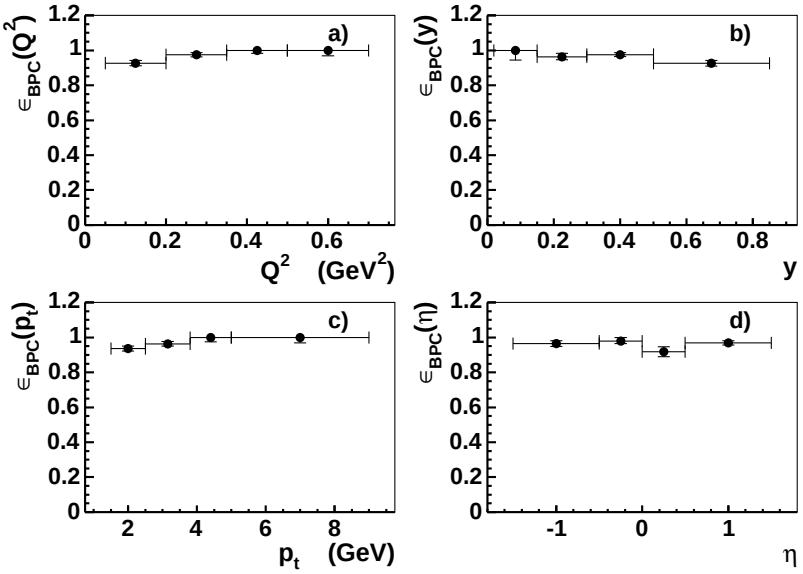

Figure 6.3: Dependence of the HFL-BPC trigger efficiency on the kinematic variables used in the D^* production at low Q^2 analysis for the running period 1998-2000. The efficiencies are divided into the analysis bins for each kinematic variable a) Q^2, b) y, c) $p_t(D^*)$ and d) $\eta(D^*)$. The errors are calculated using binominal statistics.

6.2.4 Run Range

This analysis uses the data of the running periods 1998–1999 (electrons) and 1999–2000 (positrons) taken by the ZEUS collaboration. The data taking performance and

quality were monitored during the whole period and all runs affected by detector problems were discarded.

The total integrated luminosity taken during the 1998–2000 running period is $\mathcal{L}_{int} = 82.2\,\mathrm{pb}^{-1}$. For details see Table 6.1.

Run Range	Running Period	Integrated Luminosity
30764 – 32075	$1998e^-$	$4.7\,\mathrm{pb}^{-1}$
32125 – 32906	$1999e^-$	$12.2\,\mathrm{pb}^{-1}$
33125 – 34486	$1999e^+$	$19.9\,\mathrm{pb}^{-1}$
35031 – 37715	$2000e^+$	$45.4\,\mathrm{pb}^{-1}$
Total		$82.2\,\mathrm{pb}^{-1}$

Table 6.1: Run range used in the D^* production at low Q^2 analysis. HERA switched from electrons to positrons in 1999; the charge of the lepton is indicated in the running period column.

6.3 Reconstruction of the $D^* \to K\pi\pi$ Decay

The selection of the desired class of events starts with the forming of a D^0 candidate using the 3-momentum and the charge of a pair of CTD tracks, which both passes the following conditions: the tracks can be matched to the *ep*-vertex[5], $p_t > 0.1\,\mathrm{GeV}$, the number of hit CTD super-layers ≥ 3 and the tracks are oppositely charged.

For each pair of oppositely charged particle tracks[6], the tracks are assigned alternately the π mass and the K mass. The 4-vectors, calculated from the CTD momenta and the mass hypothesis, are summed and if the mass of the 4-vector sum, $M(D^0)$, is distributed in a certain window around the mass of the D^0 particle the pair is taken into account as a D^0 candidate.

The next step is to form a D^* candidate by looking for another charged particle track and assigning the π mass to it. If the mass difference of the 4-vector sum of the latter and the D^0 candidate, $\Delta M(D^*)$, is consistent with the hypothesis of being a D^*, the three tracks are counted as a D^* candidate.

The $M(D^0)$ selection window has to be chosen with care because close to the signal peak of the D^0 particle, the so-called satellite peak can appear in the $M(D^0)$ distribution. The satellite peak comes from the $D^0 \to K^-\pi^+\pi^0$ decays. The π^0 leaves the CTD undetected. Due to the imperfect momentum (track) reconstruction such

[5]If a CTD track matches the *ep*-vertex is decided by a measurement of the distance of the extrapolated track to the vertex. It does not matter if the decay happens at the primary or secondary vertex because the ZEUS is not able to distinguish between them.

[6]Before the tracks are combined to candidates cleaning cuts are applied on the p_t of the particle tracks which build the D^0 candidate and p_t of the third particle track which then combines to the D^* candidate.

a three body decay can be misidentified as $D^0 \to K^-\pi^+$. In order to reduce these events a $p_t(D^*)$ dependent cut on the $M(D^0)$ distribution is applied (Table 6.2).

The $M(D^0)$ and ΔM distribution for the calibration sample are shown in Fig. 6.4. Both distributions show clear signals on a combinatorial background which is well described by the "wrong charge" (WC) background (Fig. 6.4). This background

$p_t(D^*)$/[GeV/c]	$M(D^0)$/[GeV] Cut Window
1.50 – 3.25	1.82 – 1.91
3.25 – 5.00	1.81 – 1.92
5.00 – 8.00	1.80 – 1.93
8.00 – 9.00	1.79 – 1.94

Table 6.2: To pick out D^* candidates a $p_t(D^*)$ dependent cut on $M(D^0)$ is used. The $M(D^0)$ cut window is widening with increasing $p_t(D^*)$ because the momentum resolution of the CTD is worsening at higher values of p_t.

is obtained by the same procedure as for the "right charge" (RC) combinations but combining like-signed charged tracks to a pseudo-D^0 candidate. All combinations of three tracks with charge ± 1 and its treatment in this analysis are described in Table 6.3. Combinations with charges $\neq 1$ are discarded.

Sign of Charge $\overbrace{K \quad \pi}^{D^0}$		π_s	Type	Treatment in the Analysis
+	+	−	WC	D^{*+} Background
+	−	−	RC	D^{*-} Signal
+	−	+	—	Neglected (DC suppr.)
−	+	+	RC	D^{*+} Signal
−	+	−	—	Neglected (DC suppr.)
−	−	+	WC	D^{*-} Background

Table 6.3: All charge combinations of CTD tracks to build a $D^{*\pm}$ candidate. The candidates are classified as RC and WC using the charge of the K and the π. The use of the combinations in the analysis is mentioned in the last column. For right charge combinations the π_s candidate carries always the charge of the decayed $D^{*\pm}$. Combinations with a subsequent decay $D^0 \to K^+\pi^-$ or $\overline{D^0} \to K^-\pi^+$ are "doubly Cabbibo" suppressed and thus neglected (branching ratio $\approx 1.5 \cdot 10^{-4}$).

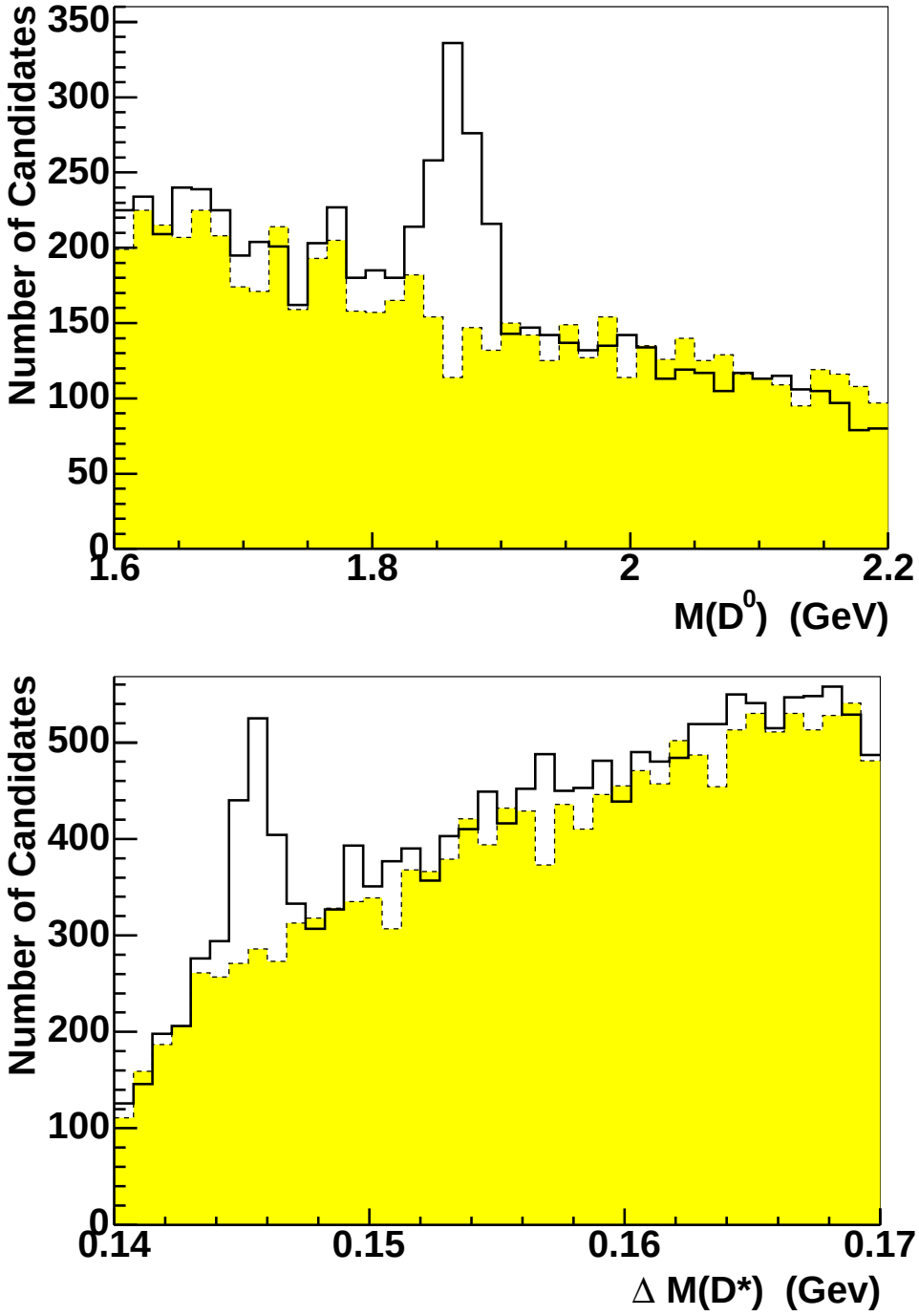

Figure 6.4: The $M(D^0)$ and $\Delta M(D^*)$ distributions obtained by combining 2 (top) + 1 (bottom) CTD tracks from the full kinematical range of this analysis after application of the preselection cuts and the $E_{BPC} > 4\,\text{GeV}$ cut. Clear invariant mass peaks of the D^0 meson ($1864.5 \pm 0.5\,\text{MeV}$ [40]) and of $\Delta M(D^*)$ ($145.421 \pm 0.010\,\text{MeV}$ [40]) can be seen. The shaded areas are the combinations of like-sign charged tracks to a D^0 candidate. This so-called "wrong charge" (WC) background gives an estimate of the combinatorial background in the "right charge" (RC) distribution. The SNR is ≈ 1.5 for the upper and ≈ 1.4 in the bottom distribution.

6.4 Monte Carlo Simulation

The reason to use a Monte Carlo simulation is to correct the number of reconstructed signal events for the detector acceptance. Thus it is necessary to simulate the production and decay of the D^* as described earlier (Chapter 3).

6.4.1 Signal Monte Carlo

The MC simulating the D^* production signal events and the subsequent decay is HERWIG 6.301. The MC sample for 1998–2000 was generated by the ZEUS heavy flavour working group for general heavy flavour analysis purposes in the full Q^2 range of the ZEUS detector ($0.01 < Q^2 < 50000\,\mathrm{GeV}^2$). It includes several charm and beauty production and decay modes. The integrated MC luminosity generated for 1998–2000 is $\approx 600\,\mathrm{pb}^{-1}$.

Trigger emulation

The BPC trigger used to select the data sample is not simulated in MC. Therefore in MC all trigger conditions (Section 6.2.2) have to be emulated by offline cuts on raw detector information.

6.5 Corrections

Several corrections have to be applied on the data and the MC sample for effects which are not simulated in data or MC.

6.5.1 Correction of the BPC Trigger Efficiency

The MC simulation of the BPC trigger is done by offline cuts in this analysis only (Section 6.4.1). These cuts do not take the dependence of the HFL-BPC trigger efficiency on the BPC energy into account. Thus the HFL-BPC energy dependence is corrected in MC using the measured efficiency in data in 1 GeV bins according to Fig. 6.5.

6.5.2 CTD Momentum Scale

The CTD momentum is scaled up by 0.3% to bring the $\Delta M(D^*)$ peak in DIS to the ΔM peak at 0.1454 GeV [79]. This correction is applied to data and MC.

6.5.3 CTD Water

In 2000 the gain of the CTD decreased significantly. In order to improve the situation a small amount of water was added to the chamber gas. The change of the gas mixture

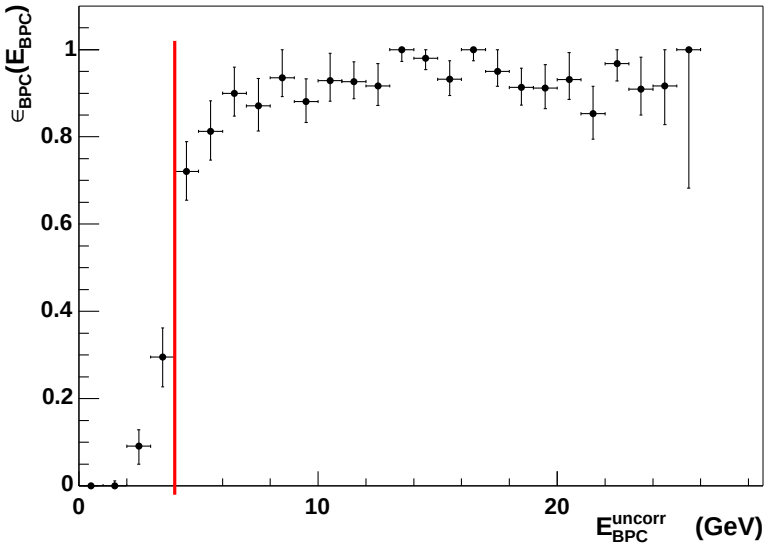

Figure 6.5: Measured energy dependence of the HFL-BPC trigger in the 1998–2000 D^* production at low Q^2 analysis data sample in bins of 1 GeV. At low E_{BPC} the the trigger is inefficient. The line indicates the cut $E_{BPC} > 4\,\text{GeV}$ which is used to reduce systematic uncertainties in the analysis. The errors are calculated using binominal statistics.

had a strong influence on the resolution of the CTD and thus on the BPC trigger, especially for low p_t tracks. To reduce the impact of this effect D^* candidates from runs with a run number larger 36560 and $p_t(\pi_s) < 0.25\,\text{GeV}$ were discarded. For the 1998–2000 MC sample a fraction of D^* candidates with $p_t(\pi_s) < 0.25\,\text{GeV}$ were discarded to correct for this effect. The fraction of D^* which should be taken into account is calculated using the integrated luminosity over the runs before the water was added to the CTD gas and the integrated luminosity over all runs used in this analysis (Sec. 6.2.4):

$$\mathcal{L}^{e^{\pm}p}_{\text{before water}}/\mathcal{L}^{e^{\pm}p} = 0.795$$

That means roughly every 5th D^* candidate with $p_t(\pi_s) < 0.25\,\text{GeV}$ is discarded.

6.6 Signal Selection Cuts

Several offline cuts are applied on data and MC in order to reduce combinatorial and physics background which is not already rejected by the trigger. Physics background of this analysis are e.g. D^* candidates coming from processes when the incoming electron radiates a photon (ISR) at a very small angle w.r.t to beam-pipe or events from photoproduction when the photon does not escape completely undetected through the beam-pipe but deposits some energy in the BPC.

The cuts and their influence on the data and MC sample are summarised in Table 6.4 and visualised in Fig. 6.6. Although the HFL-BPC trigger reduced the analysis background quite efficiently, some background events have to be discarded by the cuts. A short description of each analysis cut is given following list. The numbers in curly brackets after the cuts name correspond to the cut numbers, i, in the table. The corresponding plots are collected in Appendix B.

- Preselection cuts: {0}
  As disk space is always limited only the relevant information of the BPC and D^* triggered events are stored. The events are also preselected offline by the same conditions as the events for the BPC energy calibration (Section 5.6).

- BPC offline trigger cuts: {1}
  This cut selects only events with a positive decision at each level of the BPC trigger chain: HFL-FLT34 → HFL-SLT8 → HFL-TLT14. Due to the missing trigger simulation for the BPC in MC this cut is applied only to the data. In MC the BPC is simulated by offline cuts (Section 6.4.1 and 6.2.2) . The cuts are applied to these variables correspondingly.

- BPC timing cut: $|T^{res}_{BPC}| < 3\,\text{ns}$ {2}
  Events with time residuals longer than 3 ns are taken out of the sample because they are not correlated to the event. Their origin is mostly electronic noise. This cut is applied only to the data because the timing is not simulated in the detector simulation of the BPC.

- BPC energy cut (Fig. B.1): $E_{BPC} > 4\,\text{GeV}$ {3}
  The BPC trigger shows a lack of efficiency at energies less than 4 GeV. To reduce the systematic uncertainties BPC triggered events with lower energies are discarded. The value of this energy cut restricts the upper limit of the y range of the analysis to $y < 0.85$.

- Energy imbalance cut (Fig. B.1): $35 < \delta_{BPC} < 65\,\text{GeV}$ {4}
  The photoproduction background is rejected by applying this cut. The rejection of photoproduction background is efficient because photoproduction events typically have $\delta_{BPC} < 10\,\text{GeV}$ whereas for DIS events δ_{BPC} peaks at $\approx 55\,\text{GeV}$.

- BPC fiducial area cut (Fig. 5.4): {5}
  The fiducial area cut is applied to reduce the systematic effects caused by events with an incomplete energy measurement in the BPC (See Section 5.3.2). The fiducial area cut restricts the Q^2 range of the analysis to $0.05 < Q^2 < 0.70\,\text{GeV}^2$.

- Veto cut on Sinistra electrons: {6}
  The uranium calorimeter reconstruction software Sinistra provides the electromagnetic energy of a particle and its probability to be the scattered electron. This information is used to find BPC triggered events which are background or fake events. An event is removed if Sinistra finds an electron in the uranium calorimeter with a probability of more than 90% and an electron energy $E_e > 5\,\text{GeV}$.

- Z-Vertex cut (Fig. B.4): $|Z_{\text{Vertex}}| < 50\,\text{cm}$ {7}
  The longitudinal vertex distribution is used to reject events from non-ep background.

- D^* finder cuts (Fig. B.2): The combinatoric background of the D^* candidate reconstruction can be reduced by tightening the related cuts. For this analysis the cuts are chosen to be:

  - Slow pion momentum cut: $p_t(\pi_s) > 0.12\,\text{GeV}$ {8}

  - Pion momentum cut: $p_t(\pi) > 0.45\,\text{GeV}$ {9}

  - Kaon momentum cut: $p_t(K) > 0.45\,\text{GeV}$ {10}

- D^0 mass cut, $p_t(D^*)$ dependent: {11}
  The D^0 mass window cut has to be applied in order to select the signal range in the D^0 mass distribution. However, the CTD momentum resolution worsens with increasing momentum. Therefore the D^0 mass cut is varied depending on $p_t(D^*)$ (Table 6.2).

- CTD acceptance region cuts: {12}
  Two cuts on the D^* candidates are used to define the kinematic range of this analysis. The cuts on $|\eta(D^*)| < 1.5$ and $p_t(D^*) > 1.5\,\text{GeV}$ have already been applied in the preselection {0} of the data and MC sample. Here, additionally the upper limit of the momentum region is limited to $p_t(D^*) < 9.0\,\text{GeV}$ for a better comparison with previous ZEUS analysis. The cuts are chosen to be well within the region where the CTD acceptance is high.

- Event shape cut (Fig. B.2): $p_t(D^*)/E_t > 0.1$ cut: {13}
  The cut on $P_t(D^*)/E_t$ permits background events to be rejected without loss of signal, because charm fragmentation is hard and thus the D^* carries a significant fraction of the c-quark momentum.

No.	Cut	$(N_{0\ldots i})_{\text{data}}$	$(N_{0+i})_{\text{data}}$	$(N_{0\ldots i})_{\text{MC}}$	$(N_{0+i})_{\text{MC}}$
0	Preselection	190041	190041	1309390	1309390
1	BPC trigger	73811	73811	10041	10041
2	BPC timing	73241	174398	10041	1309390
3	BPC energy	68928	91481	9763	17252
4	δ_{BPC}	61886	114420	8635	439903
5	BPC Fiducial Area	36380	103953	4279	36736
6	Sinistra Veto	35602	183660	4257	1025928
7	Z_{Vertex}	35359	188400	4169	1274838
8	$p_t(\pi_s)$	30057	164064	3795	1172227
9	$p_t(\pi)$	26633	167760	3362	1152017
10	$p_t(K)$	22530	164273	2850	1133137
11	$M(D^0)$	3614	29212	1337	532400
12	$p_t(D^*)$	3607	189943	1326	1302357
13	$p_t(D^*)/E_t$	2806	142014	1260	1163806

Table 6.4: Influence of the cuts on data and MC for the full kinematic region of the analysis. $N_{0\ldots i}$ is the number of events which pass all cuts up to the i-th. N_{0+i} is the number of events which pass the 0-th and the i-th cut. All combinations of the fit region $m_\pi < \Delta M < 0.168\,\text{GeV}$ (RC) are taken into account. Due to the substantially reduced combinatoric background of the signal MC sample $(N_{0\ldots 14})_{\text{MC}}$ is much smaller than $(N_{0\ldots 14})_{\text{data}}$.

6.7 Signal Extraction

The total number of visible D^* candidates which are left in data in the window between $0.14 < \Delta M < 0.17\,\text{GeV}$ after all selection cuts are applied is around 2800

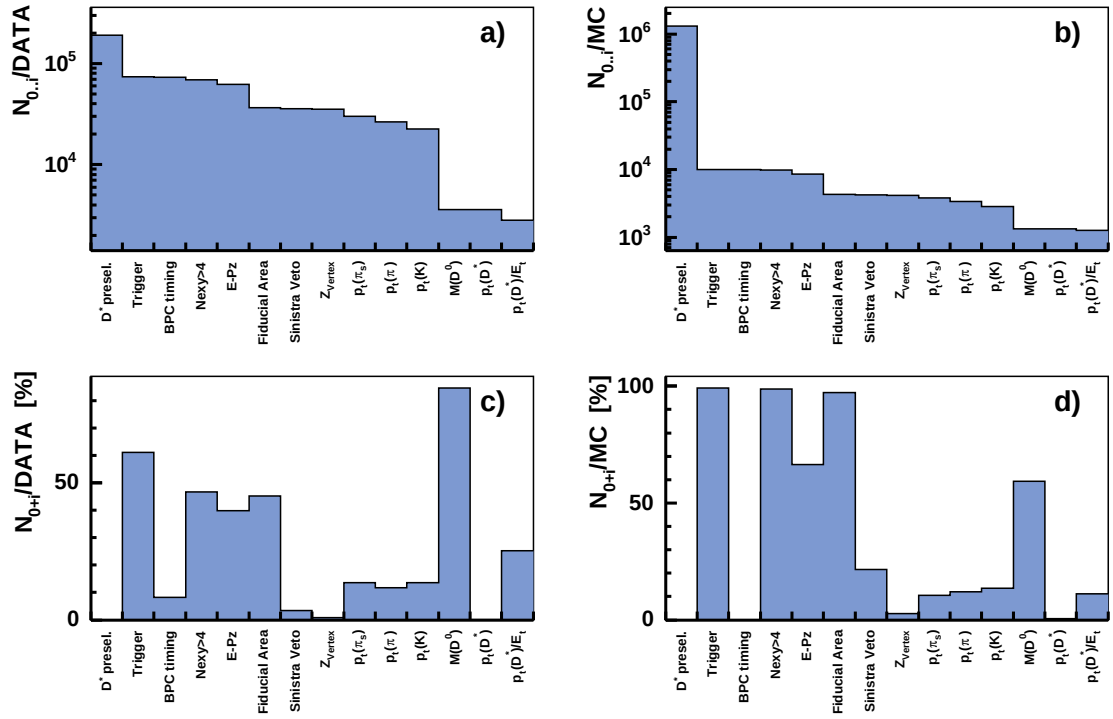

Figure 6.6: Influence of the cuts on data and MC for the visible kinematic region of the D^* production at low Q^2 analysis. $N_{0...i}$ is the number of events which pass all cuts from left to right up to the one in the corresponding bin shown in a) for data and in b) for the HERWIG signal MC. N_{0+i} is the percentage of events which are discarded by the cut in the corresponding bin w.r.t. the number of events which pass the preselection cuts shown in c) for data and in d) for the HERWIG signal MC. The cuts are described in detail in Section 6.6.

including the combinatoric background. In order to reduce the error on the measurement of the total visible cross-section and the differential cross-section the signal extraction method has to be chosen carefully. For this low statistics analysis a simple counting of the D^* after a statistical subtraction of the properly scaled[7] WC background in a certain ΔM signal window will lead to large statistical errors for the number of signal D^*. Therefore a fit of the ΔM distribution is prefered to extract the number of measured D^*. However, the standard method to fit the WC subtracted ΔM distribution using a simple Gaussian signal function has no advantage as the fit error is still large due to the subtraction of the WC background.

Hence, in this analysis the signal and background distributions are fit using the following fit function $f(\Delta M)$ with five free parameters:

$$f(\Delta M) = s(\Delta M) + b(\Delta M) \tag{6.2}$$

$$= \frac{a_0}{\sqrt{2\pi}a_2} \exp\left(-\frac{(\Delta M - a_1)^2}{2a_2^2}\right) + a_3(\Delta M - m_\pi)^{a_4} \tag{6.3}$$

with $m_\pi = 0.13957\,\text{GeV}$, the mass of the pion. The first term in Eqn. 6.2 describes the Gaussian signal (a_0: scale factor, a_1: mean and a_2: σ) whereas the second term is the combinatoric background (a_3: normalisation factor and a_4: slope).

First the ΔM distribution from WC combinations, which contains only combinatoric background, is fit over the full ΔM mass window ($m_\pi < \Delta M < 0.168\,\text{GeV}$) using only the background function $b(\Delta M)$. From this fit the scale a_3' and the slope a_4' of the WC ΔM distribution is obtained. These parameters are used as initial values for the corresponding parameters in the following fit of the RC ΔM distribution, which contains the D^* signal. This step was introduced in order to stabilise the fit results, because the combinatoric background (and the SNR) depends strongly on the considered kinematic bin.

Then the RC ΔM distribution is fit in the same range $m_\pi < \Delta M < 0.168\,\text{GeV}$ using the fit function $f(\Delta M)$ with 5 free parameters $a_0 \ldots a_4$. The initial parameters of the fit are set to the previously measured peak value of the ΔM signal [79], $a_1 = 0.1454\,\text{GeV}$, to values obtained by the previous WC background fit, $a_3 = a_3'$ and $a_4 = a_4'$, and to values which are in the expected parameter range, $a_0 = 80$ and $a_2 = 6 \cdot 10^{-4}\,\text{GeV}$[8]. However, the fit is not sensitive to the variation of a_0, a_2, a_3, a_4 and also not to small variations ($\approx 15\%$) of a_1.

To perform the fits an unbinned likelihood method [80] was used because the stability of the standard binned likelihood fits was not sufficient. The result of the fit in the total visible region (Fig. 6.8) for data is $N_{tot}^{data}(D^*) = 250 \pm 22$. The same fit on MC sample yields $N_{tot}^{MC}(D^*) = 1069 \pm 29$ (Appendix C).

For the differential analysis the total visible region has to be divided into bins of the kinematic variables. In this analysis four bins in Q^2, y, $p_t(D^*)$ and $\eta(D^*)$ were

[7] For this analysis scale factors between 0.03 and 0.06 are necessary depending on the kinematic bin. Previous ZEUS D^* analyses used scaled factors up to 0.13.

[8] Similar to previous ZEUS D^* measurements [49]

Bin n	1	2	3	4
Q^2_n (GeV^2)	$[0.05, 0.20[$	$[0.20, 0.35[$	$[0.35, 0.50[$	$[0.50, 0.70]$
y_n	$[0.02, 0.15[$	$[0.15, 0.30[$	$[0.30, 0.50[$	$[0.50, 0.85]$
$p_{t,n}(D^*)$ (GeV)	$[1.5, 2.5[$	$[2.5, 3.8[$	$[3.8, 5.0[$	$[5.0, 9.0]$
$\eta_n(D^*)$	$[-1.5, -0.5[$	$[-0.5, 0.0[$	$[0.0, 0.5[$	$[0.5, 1.5]$

Figure 6.7: Bin definitions for the differential D^* analysis in Q^2, y, $p_t(D^*)$, $\eta(D^*)$.

chosen, requiring at least 25 signal D^* in each bin. The bin definitions are given in Table 6.7.

After performing the fits in all those bins it turned out that some of the fits still do not converge, e.g. in the first Q^2 and in the first $p_t(D^*)$ bin where the combinatoric background is rather high. Therefore the widths w_i in the differential fits are fixed to $w_{tot}^{data} = a_2 \approx 6.6 \cdot 10^{-4}$ GeV and $w_{tot}^{MC} \approx 6.5 \cdot 10^{-4}$ GeV obtained by the fit of the total visible RC ΔM distribution in data and MC, respectively. This parameter fixation reduces also the fit error because number of degrees of freedom is reduced.

The ΔM distributions and the corresponding fits are presented in Fig. 6.9 and Fig. 6.10 for all bins of the data sample. The extracted number of D^* mesons $N_{X_i}(D^*)$ – with X out of $\{Q^2, y, p_t(D^*), \eta(D^*)\}$ and $i = 1 \ldots 4$ – by these fits are tabulated in the following table and a graphical representation is shown in Fig. 6.11:

$N^{data}_{X_i}(D^*)$	$n=1$	$n=2$	$n=3$	$n=4$
$X = Q^2_n$	65 ± 11	106 ± 12	57 ± 8	25 ± 6
$X = y_n$	55 ± 7	69 ± 9	78 ± 10	50 ± 10
$X = p_{t,n}(D^*)$	77 ± 13	102 ± 11	40 ± 6	31 ± 5
$X = \eta_n(D^*)$	74 ± 9	57 ± 8	40 ± 8	81 ± 12

Very similar unbinned likelihood fits are done for MC and the results are presented in Appendix C. The only difference from the fit of the data sample is that the initial fit parameters of the background function, a_3 and a_4, are not taken from separate WC background fits but are set to values which parametrise an almost flat and very low combinatoric background. This is needed because in the HERWIG MC sample the combinatoric background is significantly lower than in data.

A graphical representation of the numbers of D^* extracted by the fits in each bin for the HERWIG MC sample is shown in Fig. 6.11 and the numbers are listed in the following table:

$N^{MC}_{X_i}(D^*)$	$n=1$	$n=2$	$n=3$	$n=4$
$X = Q^2_n$	335 ± 16	433 ± 18	210 ± 13	95 ± 9
$X = y_n$	180 ± 12	294 ± 15	317 ± 16	281 ± 15
$X = p_{t,n}(D^*)$	298 ± 15	407 ± 18	207 ± 13	160 ± 11
$X = \eta_n(D^*)$	302 ± 15	200 ± 13	201 ± 13	370 ± 17

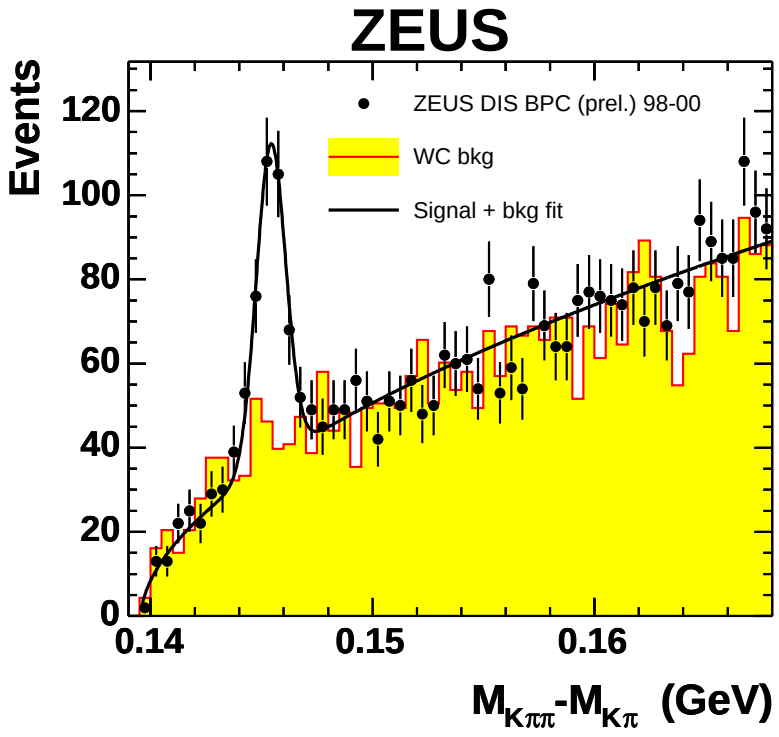

Figure 6.8: The ΔM distribution in the total visible region of the data sample. The number of D^* is extracted by an unbinned likelihood fit to a Gaussian signal function and a background function (see Section 6.7). The points represent the data, the shaded area is the WC background. The line shows the result of the fit. The obtained number of D^* is $N_{tot}^{data}(D^*) = 250 \pm 22$

The HERWIG MC sample was generated with a luminosity corresponding to $\mathcal{L}_{MC} \approx 600$ pb^{-1} and thus we expect around 6 times more events in MC than in data. The tables above are in good agreement with this expectation.

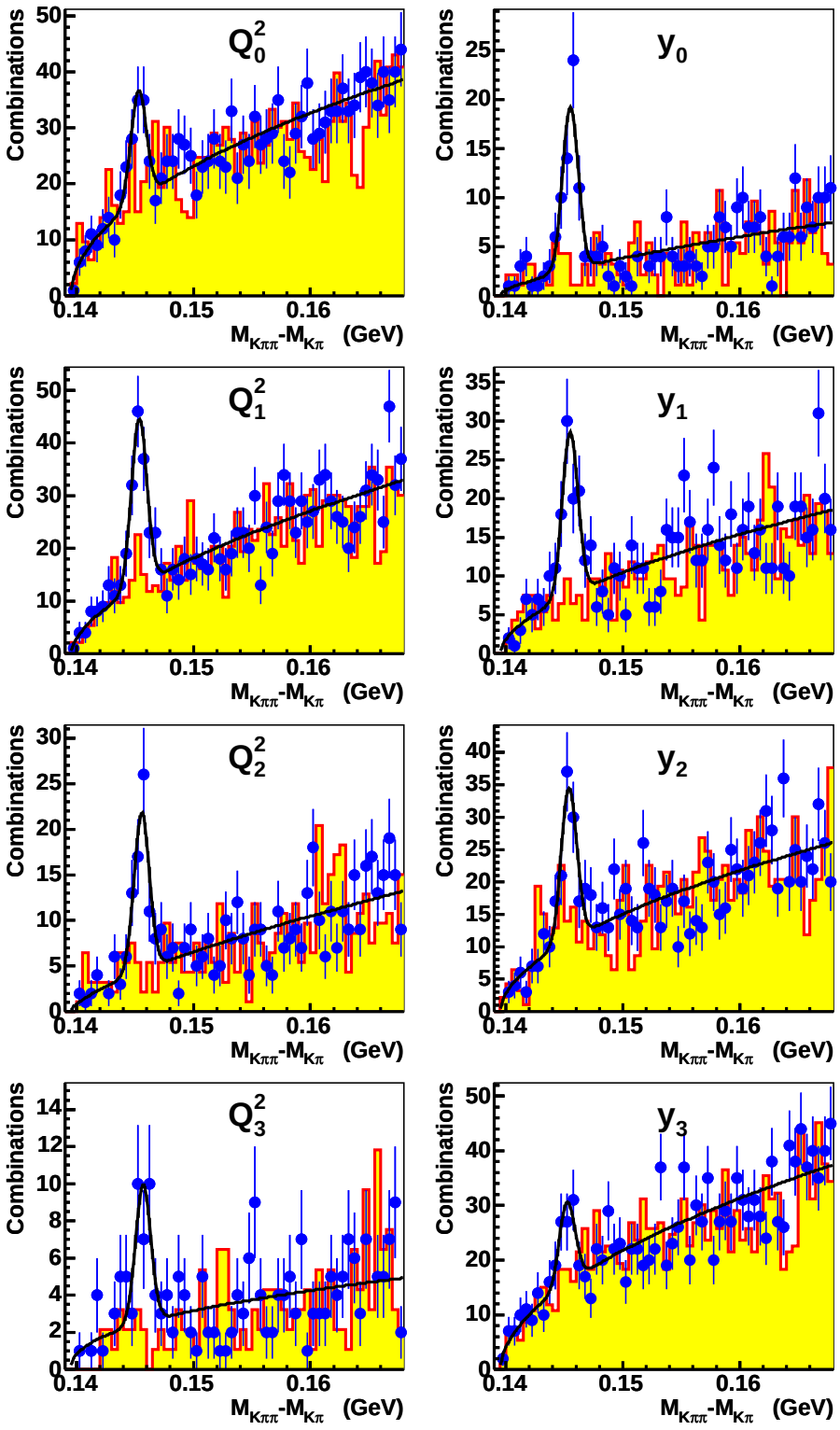

Figure 6.9: The ΔM distribution for the differential analysis in each Q^2 and y bin of the data sample. The number of D^* is extracted in every bin by an unbinned likelihood fit of a Gaussian signal + a background function (see Section 6.7). The data are represented by points, the shaded area is the WC background. The lines show the result of the fits.

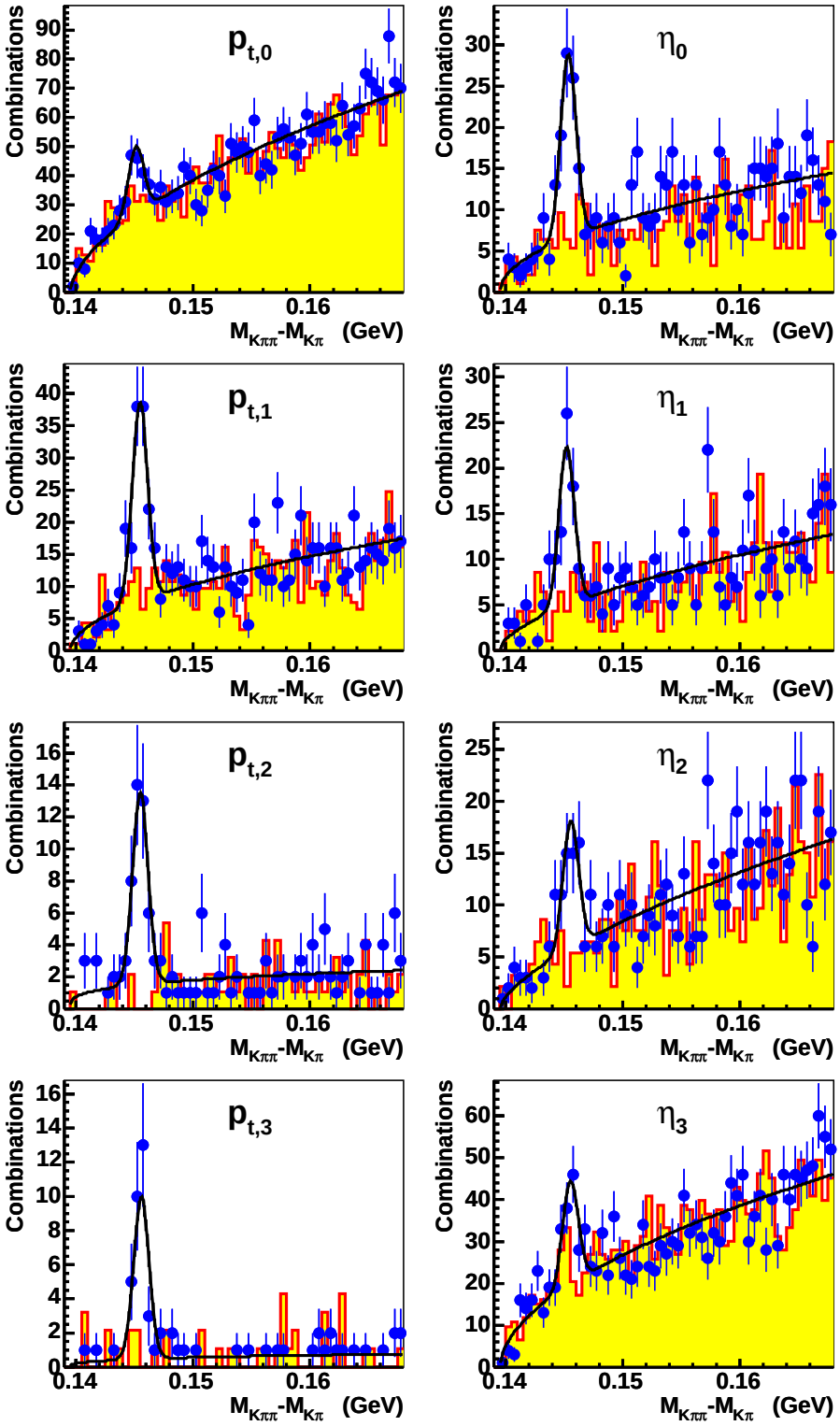

Figure 6.10: The ΔM distribution for the differential analysis in each $p_t(D^*)$ and $\eta(D^*)$ bin of the data sample. The number of D^* is extracted in every bin an unbinned likelihood fit of a Gaussian signal + a background function (see Section 6.7). Data are represented by points, the shaded area is the WC background. The lines show the result of the fits.

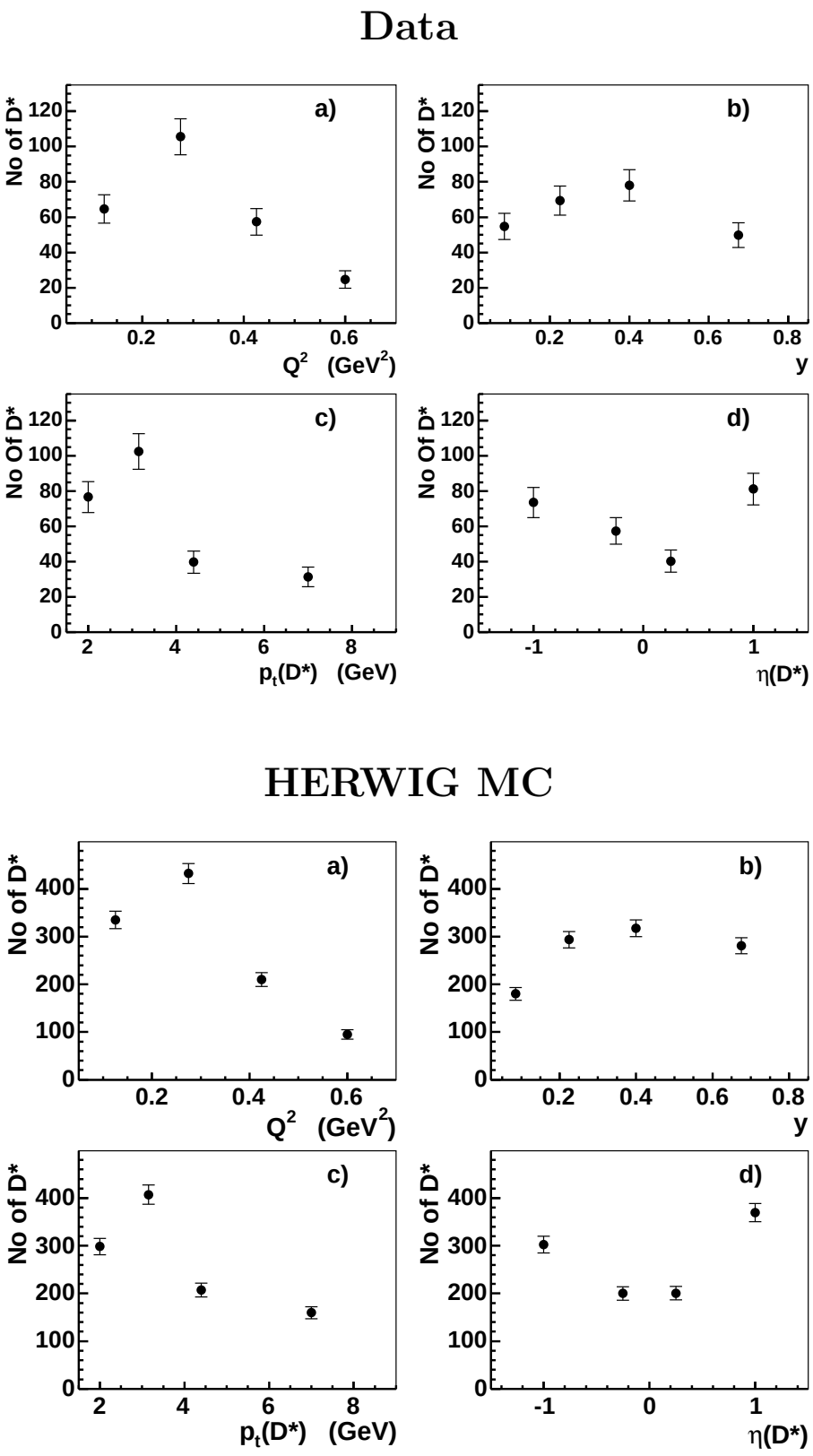

Figure 6.11: Number of D^* extracted by the unbinned likelihood fits in each analysis bin for a) Q^2_{BPC}, b) y_{BPC}, c) $p_t(D^*)$ and d) $\eta(D^*)$ of the data sample (top four) and the HERWIG signal MC sample (bottom four).

6.7.1 MC Distributions and Resolutions

The distributions of the kinematic variables Q^2, y, $p_t(D^*)$ and $\eta(D^*)$ in data and MC are shown in Fig. B.3. Q^2 and y are given by the measurement of the electron via the electron method as described in Section 2.1. The transverse momentum and the pseudo-rapidity of the D^* meson are given by the measurement of the momenta of the decay products. The mean values of these distributions for the D^* production at low Q^2 analysis are:

$$\begin{aligned} \langle Q^2 \rangle &= 0.29\,\mathrm{GeV}^2 \\ \langle y \rangle &= 0.40 \\ \langle p_t(D^*) \rangle &= 0.31\,\mathrm{GeV} \\ \langle \eta(D^*) \rangle &= 0.42 \\ (\langle x \rangle &\approx 10^{-5}) \end{aligned}$$

The correlation between the true MC and the measured kinematic variables are shown in Fig 6.12. In the low-$p_t(D^*)$ regime the momentum resolution of the CTD worsens due to two effects: one is the increase of the effect of multiple scattering. The other one is a geometrical CTD effect: Low-p_t tracks are measured predominantly only at the inner CTD superlayers because the track curvature is large. This worsens the track resolution.

Total and differential resolutions of these variables are shown in Fig. 6.13 and Fig. 6.14. The resolution is given by the σ-width of a fit of the Gaussian function to the distribution of the distance between the true and the reconstructed kinematic values. From the resolutions it can be seen that the bins of the D^* production at low Q^2 analysis are large enough to cover the resolution and therefore bin-by-bin migration can be neglected in this analysis.

6.7.2 Acceptance Corrections

The calculation of the acceptance is done in the following way:

1. D^* mesons from the HERWIG MC which were generated in the kinematic region to be measured, e.g. $0.05 < Q^2 < 0.7\,\mathrm{GeV}^2$ are counted. The values of the kinematic variables to cut on are taken from the generator. Events which pass the cut are the so-called "generated" events, N^{gen}.

2. All events undergo the same reconstruction and the same event selection as the data events (described in Section 6.6). Furthermore the same unbinned likelihood fit is used in order to extract the number of D^* (see Fig. C.2, Fig. C.3). The number of D^* mesons is extracted then for the kinematic region of interest yielding, N^{rec}.

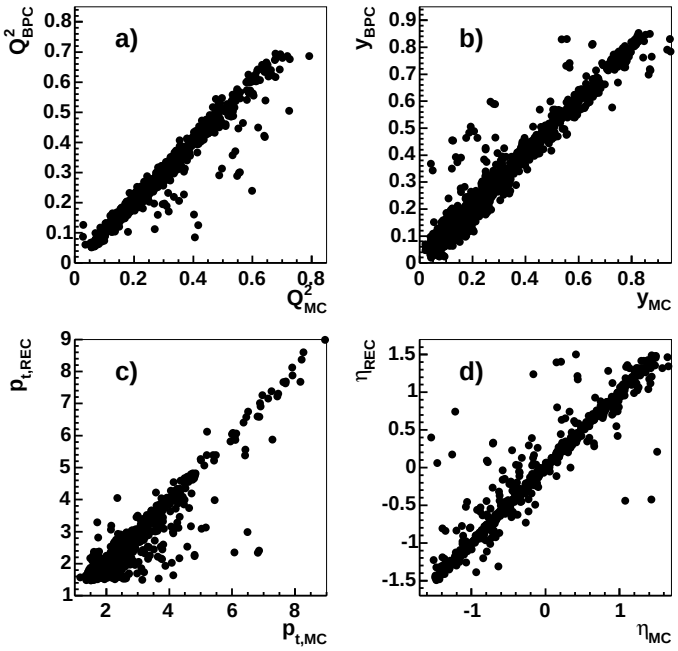

Figure 6.12: Scatter plots of the reconstructed vs. the true kinematic MC variables a) Q^2, b) y, c) $p_t(D^*)$ and d) $\eta(D^*)$ for the RC combinations in the mass difference window $m_\pi < \Delta M < 0.168\,\mathrm{GeV}$. All four variables show a reasonable correlation over the whole visible region.

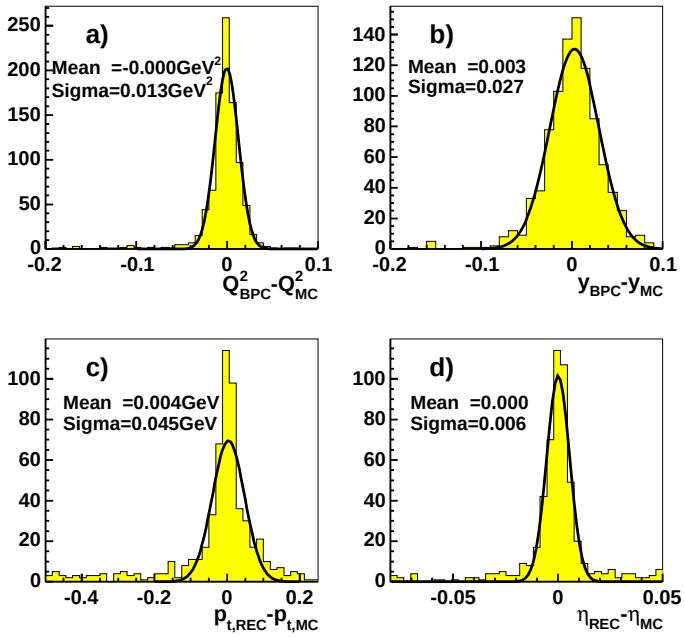

Figure 6.13: Distributions of the differences of the kinematic MC variables a) $Q^2_{MC} - Q^2_{BPC}$, b) $y_{MC} - y_{BPC}$, c) $p_{t,MC}(D^*) - p_{t,REC}(D^*)$ and d) $\eta_{MC}(D^*) - \eta_{REC}(D^*)$ for the RC combinations of the MC sample in the mass difference window $m_\pi < \Delta M < 0.168\,\text{GeV}$. The plotted differences are obtained by subtracting the reconstructed value from the true value known from MC. An estimator of the resolution of the variable is given here by the σ-width of an Gaussian function fit to the histogram. The obtained Gaussian functions are drawn and the important parameters are quoted.

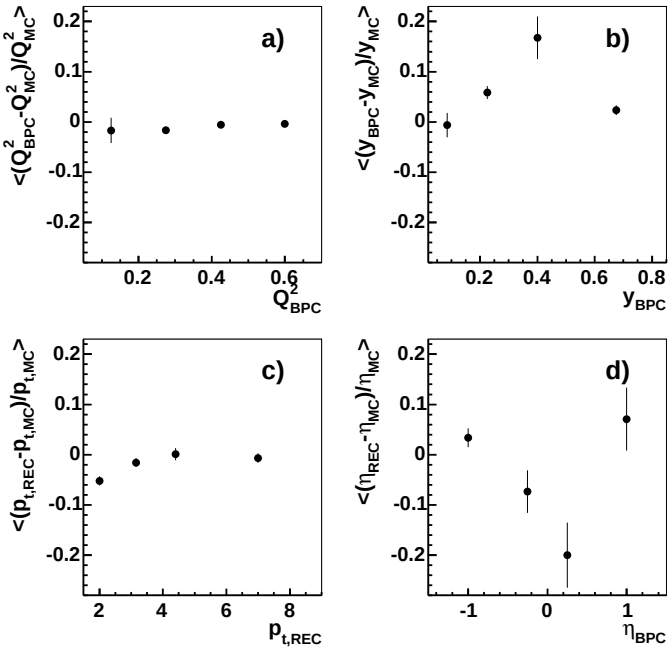

Figure 6.14: Dependency of the resolution on the reconstructed kinematic MC variables a) Q^2, b) y, c) $p_t(D^*)$ and d) $\eta(D^*)$ using the analysis binning. Only RC combinations of the MC sample in the mass difference window $m_\pi < \Delta M < 0.168\,\text{GeV}$ have been used to calculate these resolution. The points are placed in the bin centres and the error bars indicate the RMS of the distributions in the corresponding bins which can be considered as the bin resolutions. The extraction of the resolution suffers from the low statistics in the bins of the MC sample and from the few uncorrelated entries shown in Fig. 6.12. However, the bin width of this analysis is chosen wide enough to cover the RMS well in all bins. Therefore migration effects can be neglected.

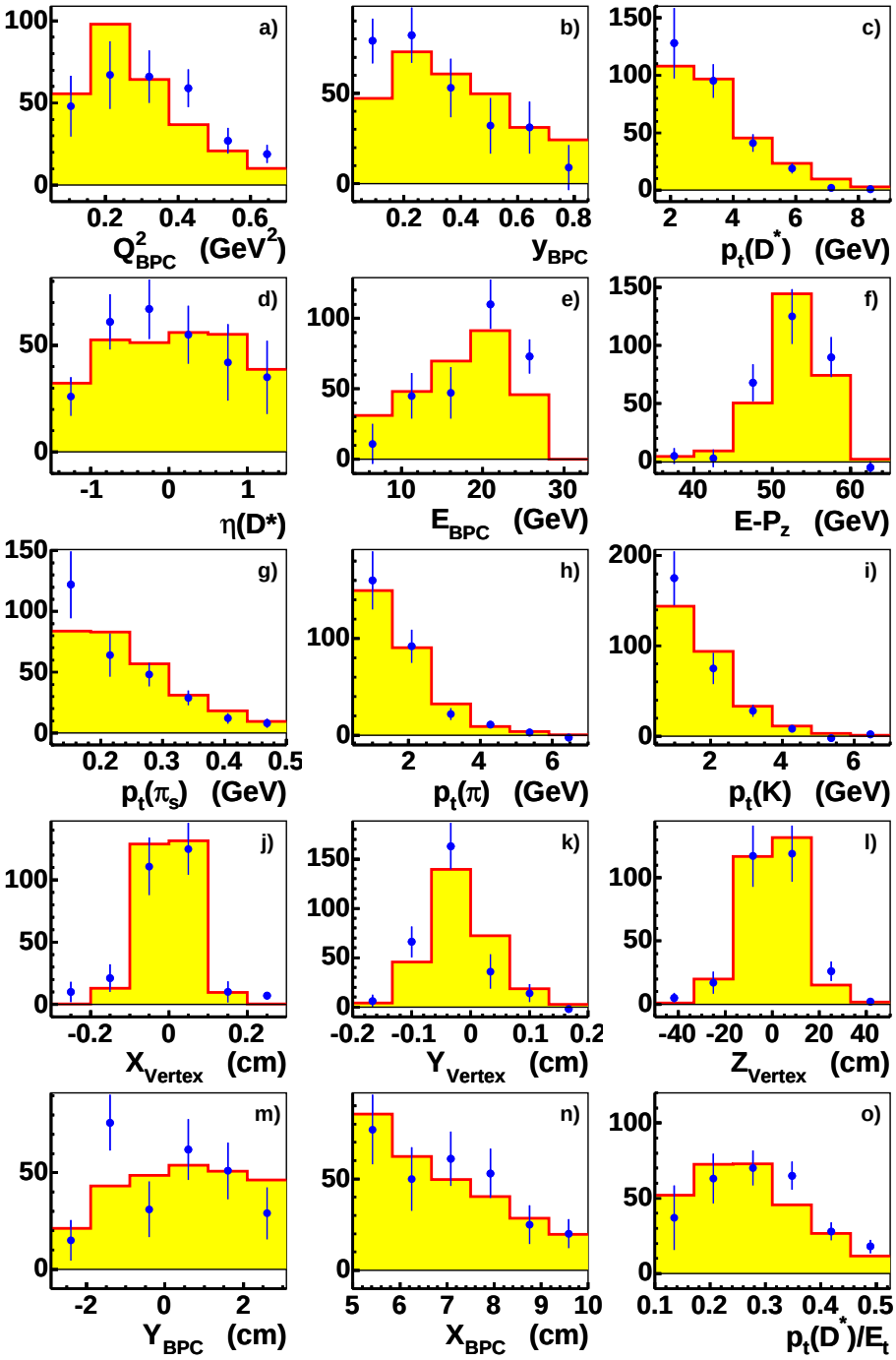

Figure 6.15: Distributions of some important variables for the analysis data sample (points) and the MC sample (shaded area) in the following order from top left to bottom right: a) Q^2, b) y, c) $p_t(D^*)$, d) $\eta(D^*)$, e) E_{BPC}, f) $\delta = (E - p_z)_{\mathrm{CAL+BPC}}$, g) $p_t(\pi_s)$, h) $p_t(\pi)$, i) $p_t(K)$, j) X_{Vertex}, k) Y_{Vertex}, l) Z_{Vertex}, m) Y_{BPC}, n) X_{BPC} and $p_t(D^*)/E_t$. In order to obtain these distributions all selection cuts of the final sample are applied except the one on the variable which the distribution shows. Additionally the WC was subtracted and only D^* events with $0.1435 < \Delta M < 0.1475\,\mathrm{GeV}$ are taken into account. The error bars indicate the statistical error. All MC distributions agree reasonably well with the data distributions.

n	$\alpha_{Q^2_n}$ [%]	α_{y_n} [%]	$\alpha_{p_{t,n}}$ [%]	α_{η_n} [%]
1	0.70 ± 0.03	2.22 ± 0.10	1.69 ± 0.10	0.82 ± 0.08
2	0.58 ± 0.04	1.13 ± 0.06	1.72 ± 0.09	1.77 ± 0.11
3	0.58 ± 0.04	1.69 ± 0.10	2.94 ± 0.18	3.49 ± 0.28
4	1.03 ± 0.05	1.33 ± 0.08	1.33 ± 0.08	1.16 ± 0.06

Table 6.5: The tabulated acceptance values for all analysis bins. The errors are given by the fit errors of function $f(\Delta M)$ (Eqn. 6.2) used to fit the ΔM distribution in the corresponding kinematic bin.

3. The acceptance α of the corresponding kinematic region is calculated as the ratio of these two numbers:

$$\alpha = \frac{N^{rec}}{N^{gen}} \tag{6.4}$$

In this analysis the acceptance is the product of two independent acceptances: the geometrical acceptance of the BPC and the acceptance of the D^* reconstruction method.

The total geometrical acceptance in the visible region of the BPC is $\approx 9\%$ [76] and typical acceptance values of the D^* reconstruction method are $\approx 14\%$ [78]. The multiplication of these values results in a acceptance value of $\alpha \approx 1.3\%$.

The calculated acceptance of the visible region of the BPC is

$$\alpha_{tot} = (1.11 \pm 0.03)\%$$

The values of the acceptance in all four kinematic variables α_{X_n} are listed in Table 6.5. Fig. 6.16 shows the graphical representation of these acceptance values.

The variation of the acceptance as a function of Q^2 and y is mainly caused by the special geometry of the BPC. The calculation of the variation as function of Q^2 can be found in Appendix D. Comparing the slope of the Q^2 dependence with the calculated variation it can be seen that the measured acceptances are distributed in agreement with the expectation.

The p_t and η dependence of the acceptance is given by the D^* reconstruction acceptance. One effect which leads to the very low acceptance values in the low-p_t regime is that a D^* with low p_t very likely contains a π_s with very low momentum, which is harder to reconstruct than one with a higher momentum. Another effect is that the water correction of the CTD, which affected the gain, results in a reduction of the acceptance in the low-p_t region (Section 6.5.3).

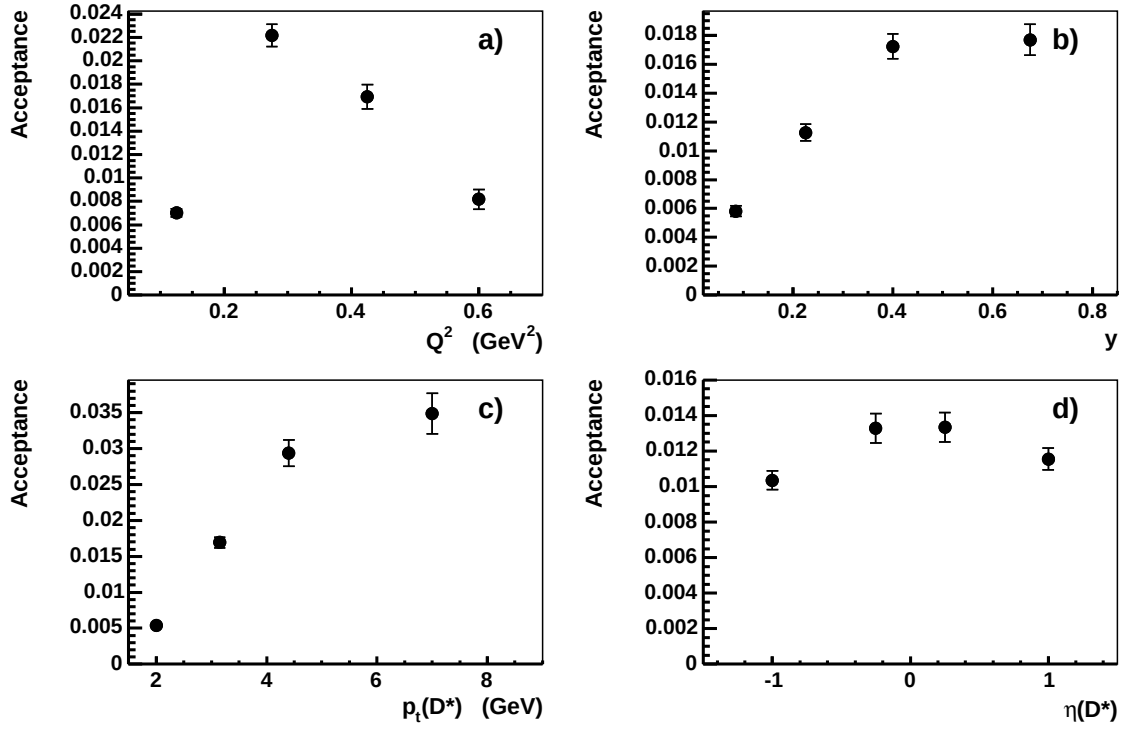

Figure 6.16: Acceptances as a function of the the kinematic variables a) Q^2_{BPC}, b) y_{BPC}, c) $p_t(D^*)$ and d) $\eta(D^*)$ using the analysis binning. The acceptance values are placed in the centre of the bins. The error bars are given by the errors of the fit to the MC.

6.8 Cross-Sections

The total visible cross-section is calculated in the full kinematic region of the BPC:

$$\sigma_{tot}(D^* \to K\pi\pi) = \frac{N_{tot}(D^*)}{\mathcal{L}_{int} \cdot \mathcal{B} \cdot \alpha_{tot} \cdot \epsilon_{BPC}} = (10.1 \pm 1.0)\,\text{nb} \tag{6.5}$$

where $N_{tot}(D^*) = 253 \pm 25$, $\mathcal{L}_{int} = (82.2 \pm 1.84)\,\text{pb}^{-1}$, $\epsilon_{BPC} = 0.97$ and $\mathcal{B} = 0.026 \pm 0.003$ are the number of total visible signal events, the integrated luminosity, the trigger efficiency and the branching ratio of the $D^* \to K\pi\pi$ decay. The acceptance in this region is $\alpha_{tot} = (1.11 \pm 0.03)\%$.

The differential cross-sections are calculated for each bin $n = 1 \ldots 4$ of the four considered kinematic variables:

$$\frac{d\sigma}{dX_n}(D^* \to K\pi\pi) = \frac{N_{X_n}(D^*)}{\mathcal{L} \cdot \mathcal{B} \cdot \alpha_{X_n} \cdot \Delta_{X_n} \cdot \epsilon_{BPC}} \tag{6.6}$$

with $X = \{Q^2, y, p_t(D^*), \eta(D^*)\}$, $N_{X_n}(D^*)$ the number of signal events in a bin, α_{X_n} the bin acceptance and Δ_{X_n} the bin width.

The results of the evaluation of the differential cross-sections using Eqn. 6.6 can be found in Table 6.6. Fig. 6.17 shows the graphical representation of these values.

The statistical error of the cross-section is given by the error of the fit in the corresponding analysis bin. The large error bars in first bins of Q^2, y and $p_t(D^*)$ are caused by the very small value of the acceptance in these bins. To calculate the errors Eqn. 6.5 and Eqn. 6.6 have to be used. It can be seen easily that therefore the fit errors are "scaled" by $1/\alpha$.

n	$d\sigma/dQ^2_n$ (nb/GeV^2)	$d\sigma/dy_n$ (nb)	$d\sigma/dp_{t,n}$ (nb/GeV)	$d\sigma/d\eta_n$ (nb)
1	$29.1 \pm 5.2^{+3.0}_{-2.8}$	$34.3 \pm 5.1^{+3.4}_{-3.2}$	$6.8 \pm 1.2^{+1.4}_{-1.4}$	$3.4 \pm 0.5^{+0.9}_{-0.9}$
2	$15.0 \pm 1.8^{+1.7}_{-1.7}$	$19.5 \pm 2.8^{+2.2}_{-2.1}$	$2.2 \pm 0.3^{+0.6}_{-0.6}$	$4.1 \pm 0.6^{+1.0}_{-1.0}$
3	$10.7 \pm 1.6^{+1.6}_{-1.6}$	$10.7 \pm 1.5^{+1.7}_{-1.6}$	$0.5 \pm 0.1^{+0.4}_{-0.4}$	$2.9 \pm 0.6^{+0.9}_{-0.9}$
4	$7.1 \pm 1.8^{+1.7}_{-1.6}$	$3.8 \pm 0.8^{+1.2}_{-1.2}$	$0.1 \pm 0.0^{+0.2}_{-0.2}$	$3.3 \pm 0.5^{+1.0}_{-0.9}$

Table 6.6: The tabulated differential cross-section for all analysis bins. The values are given in the following format: $d\sigma/dX \pm \Delta_{\text{stat}} \pm \Delta_{\text{sys}}$.

Restricted Total Visible Cross-Section

For the comparison with previous results of similar ZEUS D^* analyses in the next chapter an adjusted total visible cross-section is needed. Firstly the y region had to be restricted to $0.02 < y < 0.7$ and secondly the $p_t(D^*)/E_t$ was not applied. The result with these adjustments is:

- $N'_{tot}(D^*) = 239 \pm 27$
- $\alpha'_{tot} = (1.15 \pm 0.04)\,\%$
- $\sigma'_{tot} = (9.8 \pm 1.2)$ nb

6.9 Study of Systematic Uncertainties

In this section systematic uncertainties are studied considering only those systematic effects which contribute significantly ($> 1\%$ of the cross-section or the differential cross-sections). For an easy identification of the systematic uncertainties their indices are assigned to names in the following list:

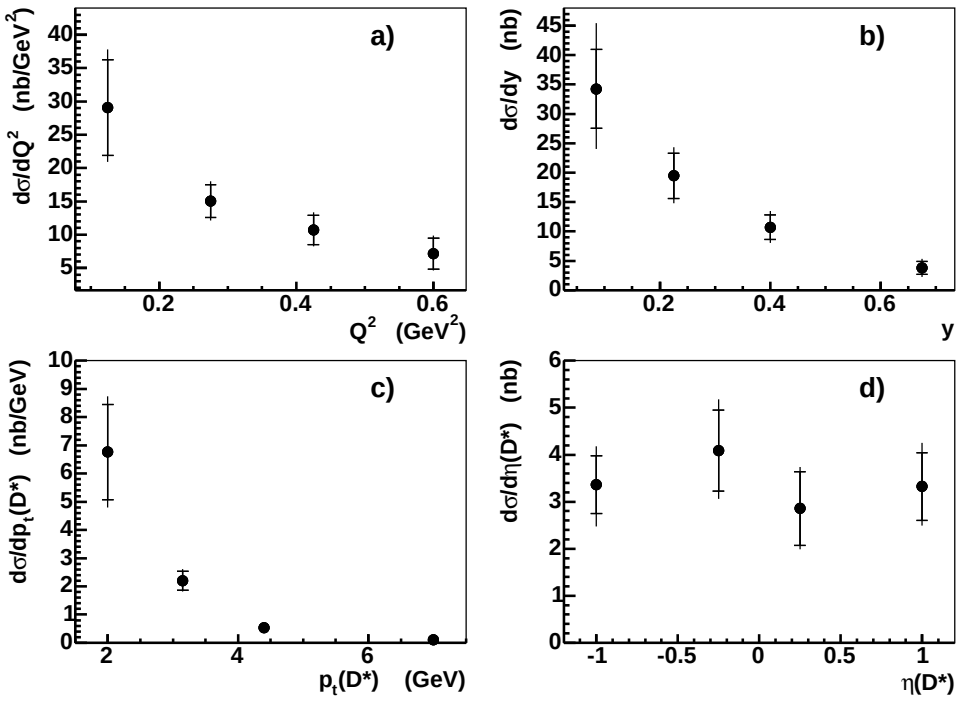

Figure 6.17: Differential cross-sections in all bins of the the kinematic variables a) Q^2_{BPC}, b) y_{BPC}, c) $p_t(D^*)$ and d) $\eta(D^*)$. The data points are placed in the centre of the bins. The inner error bars represent the statistical error of the data. The statistical and all systematic errors in the corresponding bin **are added in quadrature to obtain the outer error bars.**

0 **STD**:
The nominal cross-section value given by the standard selection cuts.

1 **RAPGAP**:
A different signal MC sample generated with RAPGAP is used.

2,3 **HW±RS∓DR**:
The HERWIG signal MC sample was composed differently of direct and resolved processes. The resolved part was increased by +30% (2) or decreased by −30% (3) constraining the integrated luminosity to be the same as the original sample. The variation of the resolved part of 30% with the above constraint results in a variation of the direct part of about 60%. These variation values are chosen because similar heavy flavour analysis at $Q^2 \approx 2.5\,\mathrm{GeV}^2$ measured the ratio of the direct to the resolved components of the BGF process with this accuracy [81].

4,5 $\boldsymbol{X_{BPC} \pm 1}$:

Shift of the BPC X position in MC by +1 mm (4) and −1 mm (5). The data are left unchanged. The variation of ±1 mm is chosen because this is the position uncertainty of the detector survey.

6,7 $\boldsymbol{Y_{BPC} \pm 1}$:
Shift of the BPC Y position in MC by +1 mm (6) and −1 mm (7). The data are left unchanged.

8,9 **±CTD-Scale**:
Variation of the CTD momentum scale by −0.3% (8) and +0.3% (9) in MC [68].

10,11 <>, >< **FidArea**:
The BPC fiducial area is extended or reduced by shifting the edges of the area by 1 mm outwards (10) or inwards (9).

12,13 ><, <> $\boldsymbol{\Delta M(D^0)}$:
The invariant mass window $\Delta M(D^0)$ to select D^0 combinations is decreased (12) or increased (13) by 10 MeV.

14,15 $\boldsymbol{\pm E_{BPC}}$**-Scale**:
Variation of the BPC energy by −1% (14) or +1% (15) in MC. This variation is chosen w.r.t. the BPC test-beam energy measurements.

16,17 $\pm\sigma$ **fixed fit**:
For the differential analysis the σ_i of the unbinned likelihood fits in each bin, which are fixed to σ of the total visible fit, are varied by $+\Delta\sigma$ (16) or $-\Delta\sigma$ (17).

18,19 **±CAL E**:
Variation of the CAL energy scale by +2% (18) or −2% (19) in MC. Data are left unchanged.

20,21 $\boldsymbol{\pm p_t(D^*)/E_t}$: Variation of the $p_t(D^*)/E_t$ cut by +20% (20) or −20% (21) in data and MC.

A graphical representation of the systematic uncertainties of the total visible cross-section is shown in Fig. 6.18. For the differential analysis the same is shown for each bin in Fig. 6.19.

The systematic error of the total cross-section is calculated by summing up the uncertainties of all studies in quadrature separately for the upper and the lower values:

$$\Delta_{tot}^{sys} = \sqrt{\sum_{n \in \Sigma^{\pm}} (\sigma_{tot} - \sigma_{tot}^{n})^2} \tag{6.7}$$

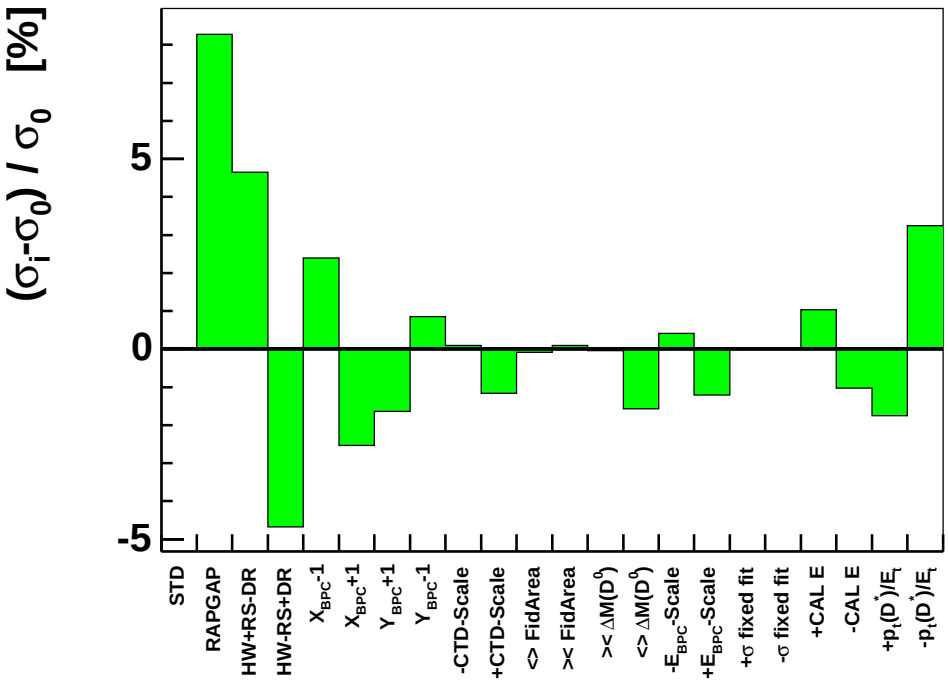

Figure 6.18: Systematic uncertainties of the total visible cross-section of the D^* production at low Q^2 analysis. Each systematic uncertainty is represented by the percentage of the deviation from the nominal total visible cross-section. Details on each uncertainty can be found in Section 6.9. The "σ fixed fit" uncertainties (16) and (17) do not affect the total visible cross-section as the width is a free parameter in this fit. Therefore the corresponding bins in this histogram are not filled.

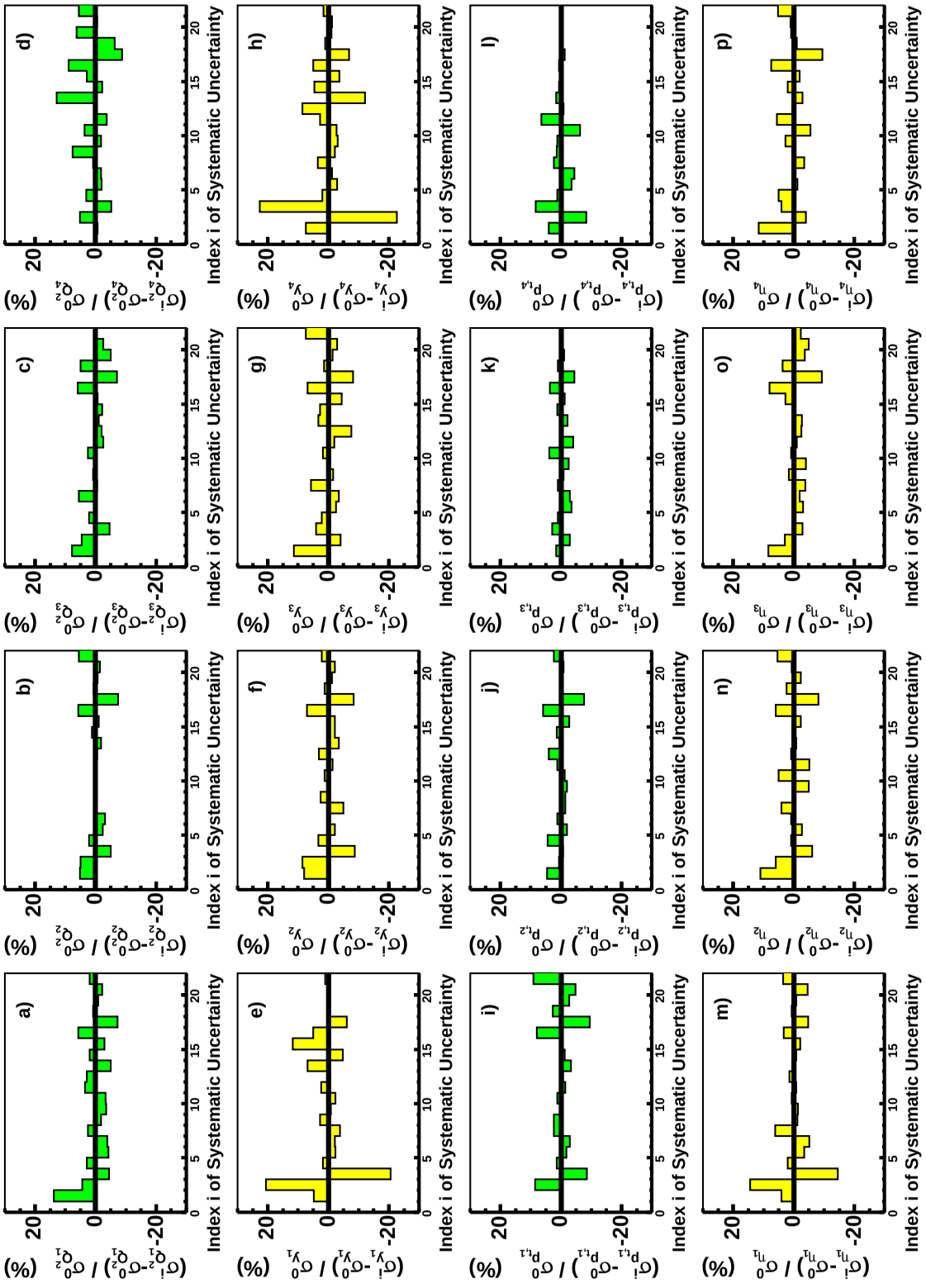

Figure 6.19: Systematic uncertainties for all differential cross-section bins of the D^* production at low Q^2 analysis. The Q^2 bins are represented by plots a)-d), y are e)-h), p_t bins are i)-l) and η bins are m)-p) in increasing order from left to right. Each systematic uncertainty is represented by the percentage of the deviation from the nominal differential cross-section in the corresponding bin. Details on each uncertainty can be found in Section 6.9.

with $\Sigma^{\pm}$ the set of variations with $\sigma_{tot} - \sigma^{n}_{tot,n} > 0$ (Σ^{+}) or $\sigma_{tot} - \sigma^{n}_{tot,n} < 0$ (Σ^{-}). Using Eqn. 6.7 and Eqn. 6.5 yields

$$\sigma_{tot}(D^{*} \to K\pi\pi) = \left(10.1 \pm 1.0\,(\text{stat.})^{+1.1}_{-0.7}\,(\text{syst.})\right)\ \text{nb} \tag{6.8}$$

The systematic errors in all kinematic bins of the analysis are calculated correspondingly and are listed in Table 6.6.

In most of the kinematic bins the statistical errors dominate the error of the measurement. In the other bins the systematic effects caused by using the RAPGAP MC sample instead of HERWIG and by the variation of the resolved and direct components in the HERWIG MC give the largest contributions.

Chapter 7

Results

This chapter starts with the comparison of the cross-section for the production of D^* mesons at low Q^2 with predictions from NLO calculation. The cross-section will then be put into the context of previous ZEUS D^* production measurements. The chapter ends with a discussion of the results.

7.1 Comparison with HVQDIS Predictions

The NLO predictions which are used to compare with the results of this analysis are obtained using the HVQDIS program described in Section 3.2.

Although the HVQDIS program was originally not designed to perform NLO calculation in the low Q^2 region it can be used at this values of Q^2 because the calculation neglects the terms of orders higher than α_s. These terms also contain $\log(Q^2/m_c^2)$ factors which can become large for $Q^2 \gg m_c$.

The nominal – or central – values of the predictions presented in Fig. 7.1 and Fig. 7.2 are calculated using the following four main parameters for the HVQDIS calculations (the complete parameter set can be found in Appendix E):

- Peterson fragmentation with $\epsilon_Q = 0.035$
- Charm quark mass $m_c = 1.35\,\text{GeV}$
- Normalisation and factorisation scale $\mu = \sqrt{Q^2 + 4m_c^2}$
- ZEUS NLO QCD fit [9] for the parametrisation of the proton PDFs

The nominal cross-section in the total visible region of the BPC calculated with those parameters is:

$$\sigma_{tot}^{\text{HVQDIS}}(D^* \to K\pi\pi) = 8.6^{+1.9}_{-1.8}\ \text{nb} \tag{7.1}$$

In order to estimate the theoretical uncertainty quoted above, four independent errors from the ZEUS NLO PDF fit and the HVQDIS calculation have been added up in quadrature. These errors are: the combined uncertainty of the ZEUS PDF fit, the

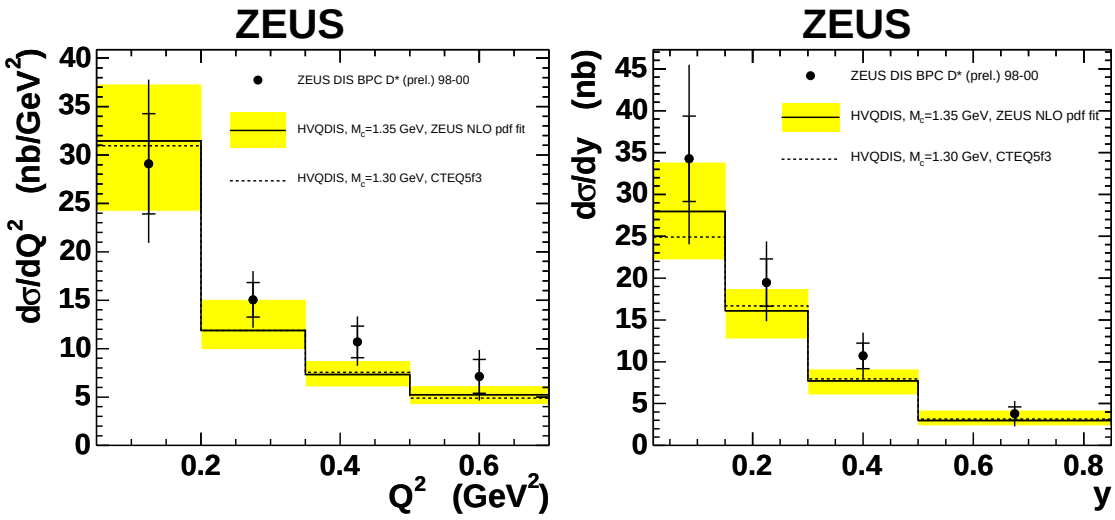

Figure 7.1: Measured differential $D^* \to K\pi\pi$ production cross-sections in bins of Q^2 (left) and y (right) compared to the NLO predictions of HVQDIS. Data are represented by points. The inner error bars are the statistical errors of the measurement while the open error bars are the sum of statistical and systematical uncertainties added in quadrature. The shaded area indicates the theoretical uncertainties obtained by variation of the HVQDIS parameters described in the text. The dashed lines represent the HVQDIS calculation for the CTEQ5f3 parametrisation of the PDF fits.

variation of the charm quark mass $1.2 < m_c < 1.5\,\text{GeV}$ in the range of the results from lattice calculations [25], the variation of the scale $(Q^2 + m_c^2) < \mu^2 < 4(Q^2 + 4m_c^2)$ [49] and the variation of the parameter ϵ_Q of the Peterson fragmentation function $0.02 < \epsilon_Q < 0.05$. The variation of the scale μ tests the m_c dependency of this scale at low Q^2. In other words, it tests, if m_c is still a hard scale at low Q^2.

The largest contributions to the theoretical uncertainty come from the charm mass variation ($\sim$ 60% of the theoretical uncertainty) and the scale variation ($\sim$ 25%). These variations are also performed for the HVQDIS calculations in each analysis bin.

Another source of uncertainty is estimated using the CTEQ5f3 parametrisation of the PDF fits instead of the ZEUS NLO QCD fit. However it is not taken into account in the theoretical uncertainty but only drawn for each bin in Fig. 7.1 and Fig. 7.2, where the measured differential cross-sections and the corresponding NLO calculations from HVQDIS as functions of Q^2, y, $p_t(D^*)$ and $\eta(D*)$ are presented. As can be seen the effect of this variation is small, except in the 1st y bin where the deviation is $\approx 10\%$ w.r.t. to the nominal value of the NLO calculation. For an easier comparison of the results the charm quark mass used in the HVQDIS calculation for the CTEQ5f3 parametrisation is the same as in [49].

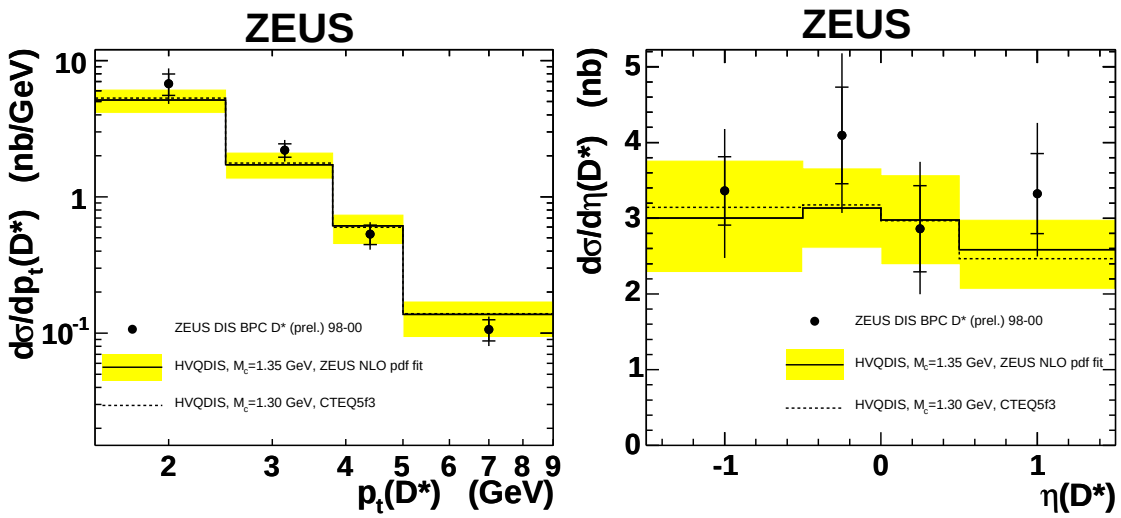

Figure 7.2: Differential $D^* \to K\pi\pi$ production cross-sections in bins of $p_t(D^*)$ (left, using a logarithmic $d\sigma/dp_t(D^*)$ scale) and $\eta(D^*)$ (right) compared to the NLO predictions of HVQDIS. The data are represented by points and the shaded area indicates the theoretical uncertainties obtained by variations of the HVQDIS parameters. The dashed lines represent the HVQDIS calculation with CTEQ5f3 parametrisation of the PDF fits.

The HVQDIS calculation for the total visible region yields then:

$$\sigma_{tot}^{\mathrm{HVQDIS,CTEQ5f3}}(D^* \to K\pi\pi) = 8.1 \text{ nb}$$

The measured cross-sections are consistent with NLO calculation of BGF charm production using the HVQDIS program and ZEUS NLO PDF fits. However, the predictions slightly underestimate the data.

7.2 Combination with previous ZEUS Results

This analysis extends previous ZEUS measurements of D^* production in DIS [49], which were made in the range $1.5 < Q^2 < 1000\,\mathrm{GeV}^2$, to the low Q^2 region.

In order to be able to compare the results the kinematic region of this analysis is restricted to the same kinematic region as the previous D^* analysis (described in Section 6.8). For this restricted analysis the differential cross-section as a function of Q^2 is calculated and presented together with the previous ZEUS measurement and the NLO prediction from HVQDIS in Fig. 7.3. The combination of both measurements shows that the slope of $d\sigma/dQ^2$ changes with Q^2. At high Q^2 the slope is steeper than at low Q^2 as predicted by HVQDIS. Therefore the analysis in this thesis extends the previous measurement in good agreement with the HVQDIS NLO calculations.

It should be mentioned that there is a small gap between $Q^2 = 0.7\,\mathrm{GeV}^2$ and $Q^2 = 1.5\,\mathrm{GeV}^2$ which is not covered by the measurements. Also it was not possible to add the corresponding PhP cross-section value to the DIS measurements because the previous ZEUS PhP analysis used incompatible kinematic cuts to be compared with the measurements of this analyses.

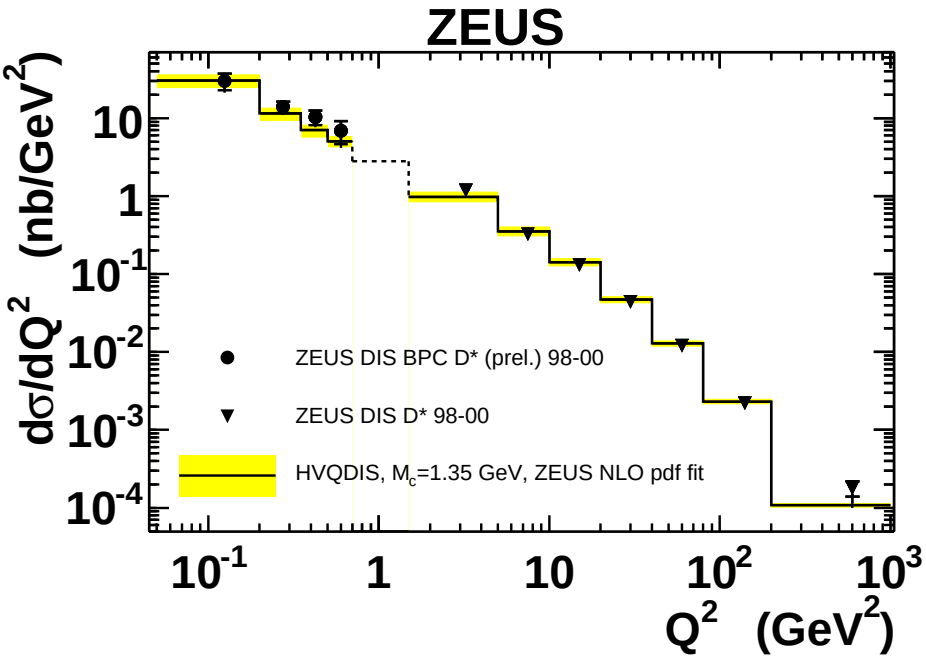

Figure 7.3: The D^* production cross-section as a function of Q^2 for the low Q^2 analysis in this thesis with slightly changed kinematic cuts (Section 6.8) and from previous results on D^* production in DIS [49] compared to NLO predictions. The results are shown using logarithmic scales. The data are represented by points. The inner error bars are the statistical errors of the measurement while the open error bars are the sum of statistical and systematical uncertainties added in quadrature. The shaded area indicates the theoretical uncertainties obtained by variations of the HVQDIS parameters. The dashed line is the prediction for the Q^2 region ($0.7 < Q^2 < 1.5\,\mathrm{GeV}^2$) where no measurements are available.

7.3 Discussion and Interpretation of the Results

The previous comparison showed that the measured differential cross-sections can be described over the complete Q^2-region of ZEUS by the NLO predictions from the HVQDIS program. However, the central total and differential D^* production cross-sections from the NLO calculation lie below the measured total and differential cross-sections in almost all bins.

The underestimate of the measured cross-sections in the low Q^2 region by the NLO calculation may have several reasons: the charm quark mass $m_c = 1.35\,\text{GeV}$ has been set too high, the effect of the charm quark mass in the factorisation and renormalisation scale $\mu = \sqrt{Q^2 + 4m_c^2}$ is underestimated or the omission of the terms of orders higher than α_s is not justified for the low Q^2 regime and inclusion of these higher order α_s terms would increase the cross-sections. The influence of the Peterson fragmentation function parameter ϵ_Q and the chosen PDF fit parametrisation is small and therefore of minor importance in this context.

The lowest charm quark mass obtained by different QCD lattice calculations for hadron composition is $m_c = 1.2\,\text{GeV}$. Comparing the measured cross-sections with the NLO calculation for $m_c = 1.2\,\text{GeV}$ it can be seen that the measurements and the NLO predictions agree within the 1σ error of the measurements. Thus, the results of this analysis would prefer a lower charm quark mass than the one which is originally used in the NLO calculation for the nominal cross-sections ($m_c = 1.35\,\text{GeV}$). However, comparing the measured and the central NLO cross-section one can see that they agree within the 2σ error. Therefore the measurement is in reasonable agreement with the NLO calculations.

Beside this, it is very likely that the omission of the higher α_s terms in the NLO calculation is not justified if the predictions are compared with the low Q^2 measurements and that the omission contribute to the underestimate of the measurements.

In general the slope of the differential cross-sections measured in this analysis is defined by the the phase space available to produce a D^* meson and the influence of the partonic structure of the proton given by its structure functions (Section 2.1.1). The differential cross-sections as functions of $p_t(D^*)$ and $\eta(D^*)$ reflect only the phase space dependency of the D^* production, because the structure functions do not depend on them.

The variation of the measured differential cross-sections as a function of Q^2 and y (Fig. 7.3 and Fig. 7.1) is strongly influenced by the proton structure functions $F_2^{c\bar{c}}(Q^2, x)$ and $F_L^{c\bar{c}}(Q^2, y)$. The slope of $d\sigma/dQ^2(Q^2)$ flattens[1] towards lower values of Q^2 because in the PhP region the Q^2 dependency of the differential cross-section is $\sim 1/Q^2$ and compensates the Q^2 dependency of $F_2 \sim Q^2(\sigma_T + \sigma_L)$. At higher values of Q^2 the variation of the differential cross-section is $\sim 1/Q^4$ coming from the photon propagator term. Therefore the cross-section falls towards higher Q^2 as $1/Q^2$. The slope of the measured $d\sigma/dQ^2(Q^2)$ is in good agreement with these predictions.

The differential cross-sections presented in this thesis are in reasonable agreement with the NLO calculation using HVQDIS. They extend the previous ZEUS measurements of $\frac{d\sigma}{dQ^2}(D^* \to K\pi\pi)$ to lower Q^2. The dependence on Q^2 of $\frac{d\sigma}{dQ^2}(D^* \to K\pi\pi)$ is in in good agreement with the theoretical expectations.

[1] For this consideration x is fixed to the mean value of this analysis, 10^{-5}.

Chapter 8

Summary and Outlook

In this thesis a measurement of charm production in deep-inelastic ep-scattering at low Q^2 in the transition region between PhP and DIS has been presented. The data were taken with the ZEUS detector during the period 1998–2000 and amount to an integrated luminosity of 82.2 pb^{-1}. The total and differential cross-sections were calculated. The low Q^2 region could be reached using the beam-pipe calorimeter which measures the scattered electron at small angles.

The reconstruction and selection of the DIS events followed the standard procedures of a high energy particle physics analysis. The selection of events with charm production was made using the decay of charmed D^* meson. Special emphasis was put on the calibration of the BPC in order to reconstruct events in the range $0.05 < Q^2 < 0.7\,\mathrm{GeV}^2$ and $0.02 < y < 0.85$. Several corrections had to be applied to get an accurate measurement of the energy and the position of the scattered electron which is needed in the calculation of the kinematic variables Q^2 and y. For the first time a special trigger designed for HFL analyses at low Q^2 was used and its performance has been investigated.

The cross-section for charm production was measured using the decay of D^* mesons into lighter mesons $D^{*+} \to K^-\pi^+\pi^+$ and the charged conjugated decay in the kinematic region $0.05 < Q^2 < 0.7\,\mathrm{GeV}^2$, $0.02 < y < 0.85$, $1.5 < p_t(D^*) < 9.0\,\mathrm{GeV}$ and $-1.5 < \eta(D^*) < 1.5$. The measured total cross-section $\sigma_{tot}(D^* \to K\pi\pi) = 10.1 \pm 1.0^{+1.1}_{-0.7}\,\mathrm{nb}$ agrees with the theoretical prediction from the NLO calculation, $\sigma_{tot}^{\mathrm{HVQDIS}}(D^* \to K\pi\pi) = 8.6^{+1.9}_{-1.8}\,\mathrm{nb}$. For the extension of previous ZEUS measurements the cross-section was additionally calculated in a restricted y range of $0.02 < y < 0.7$. This total cross-section $\sigma'_{tot} = 9.8 \pm 1.2^{+1.1}_{-0.7}\,\mathrm{nb}$ also agrees with the corresponding NLO prediction, $\sigma'^{\mathrm{HVQDIS}}_{tot}(D^* \to K\pi\pi) = 8.2^{+1.8}_{-1.8}\,\mathrm{nb}$.

Differential cross-sections as a function of Q^2, y, $p_t(D^*)$ and $\eta(D^*)$ were presented. The agreement with the theoretical predictions from NLO calculations was reasonable. For the extension of previous ZEUS measurements the differential cross-section as a function of Q^2 is calculated in the y range of previous ZEUS D^* DIS analysis. The obtained differential cross-section agree within the errors with the predictions from the NLO calculation and extend the kinematic region of the previous ZEUS

measurement towards the PhP regime.

Finally, it could be shown in this thesis that the NLO calculation which is based on the standard model of particle physics and uses the perturbative QCD ansatz is able to describe the obtained cross-sections in the transition region between PhP and DIS.

One future prospect is to extract the charm contribution to the proton structure function $F_2^{c\bar{c}}(Q^2, x)$ in the low Q^2 region of this analysis. In order to extract $F_2^{c\bar{c}}(Q^2, x)$ first the double differential cross-section $\frac{d^2\sigma}{dxdQ^2}(Q^2, x)$ has to be measured in some bins with reasonable statistics. From this double differential cross-section $F_2^{c\bar{c}}$ can be calculated using the LO MC, the NLO predictions and a standard unfolding technique. The measurement will extend previous HERA measurements of $F_2^{c\bar{c}}(Q^2, x)$ to the low Q^2 and low x region of the kinematical range where hardly any measurement has been done, except for a few measurements by fixed target experiments.

An interpolation of the differential cross-section of charm production as a function of Q^2 to the PhP regime would be very desirable. This needs a measurement from ZEUS or H1 in a consistent kinematic range.

Appendix A

BPC Calibration Sample

The following trigger conditions and cuts are applied in order to obtain the BPC calibration sample used in Chapter 5 to calibrate the energy of the BPC:

- Trigger Selection: (DST bit 90) $\vee$ (DST bit 27) $\vee$ (HFL-TLT10) $\vee$ (HFL-TLT14)
- At least one D^* candidate could be reconstructed in the event as described in Section 6.3 with following conditions:
  - $p_t(K, \pi) > 0.35\,\text{GeV}$
  - $p_t(\pi_s) > 0.10\,\text{GeV}$
  - $|\eta(K, \pi, \pi_s)| < 1.9$
  - $1.4 < M(D^0) < 2.2\,\text{GeV}$
  - $0.14 < \Delta M(D^*) < 0.17\,\text{GeV}$
  - $p_t(D^*) > 1.5\,\text{GeV}$
  - $|\eta(D^*)| < 1.5$
- Electron energy deposition in BPC with $E_{BPC}^{uncorr} > 0.1\,\text{GeV}$
- DIS event selection: $35 < \delta_{BPC} < 65\,\text{GeV}$

The calibration sample contains around 100000 D^* candidates after all cuts are applied. The signal-to-noise ratio of the D^* signal in calibration sample is ≈ 0.1.

Appendix B

Selection Cuts

In this appendix the chosen final selection cuts (see Section 6.6) will be introduced and shown.

B.1 BPC Distributions

The two most important BPC distributions – E_{BPC} and δ_{BPC} – and the cuts on them are shown in Fig. B.1. The reason for the $E_{BPC} > 4\,\text{GeV}$ cut is the decreasing efficiency of the BPC trigger used in this analysis below 4 GeV. The $35 < \delta_{BPC} < 65\,\text{GeV}$ cut is used to select DIS and reduce the background from PhP events.

B.2 D^* Distributions

Fig. B.2 shows the four distributions and cuts with the largest effect on the D^* reconstruction. The reason to use such cuts is to remove the "soft" D^* (low momentum) candidates which are most probably not D^* but (WC) background.

B.3 Distributions of the Kinematic Variables

The cuts on the kinematic event variables depend on the acceptances of the ZEUS detector components used in this analysis to reconstruct the event, namely the BPC and the CTD. The geometrical acceptance of the BPC restricts the Q^2 and y region, whereas the $p_t(D^*)$ and the $\eta(D^*)$ region is defined by the acceptance of the CTD.

B.4 Vertex Distributions

The cut on the Z_{Vertex} distribution is applied to clean the samples from non-physics background as described in Section 6.6.

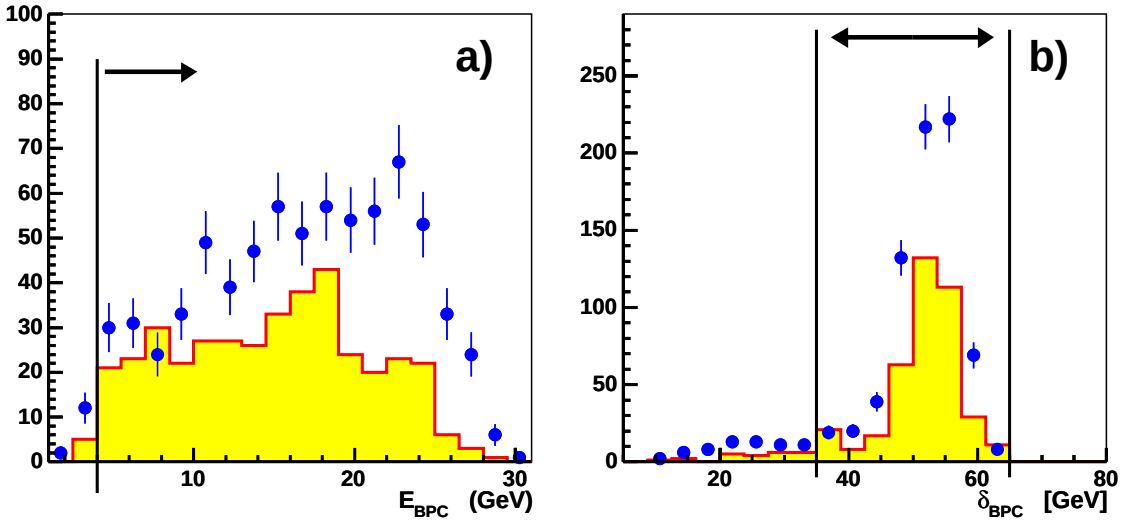

Figure B.1: Distribution of a) the reconstructed BPC energy and b) δ_{BPC} for the 1998–2000 data sample. In order to obtain these distributions all selection cuts of the final sample are applied except the one on the variable which the distribution shows. Additionally only D^* events with $0.1435 < \Delta M < 0.1475\,\text{GeV}$ are taken into account. The (right charged) signal distribution is represented by points while the error bars indicate the statistical error. The shaded area represents the wrong charge background (WC) from track combinations with sign-like charge. The vertical lines and the arrows indicate the selection cuts which are applied on the corresponding variables to select the final D^* sample.

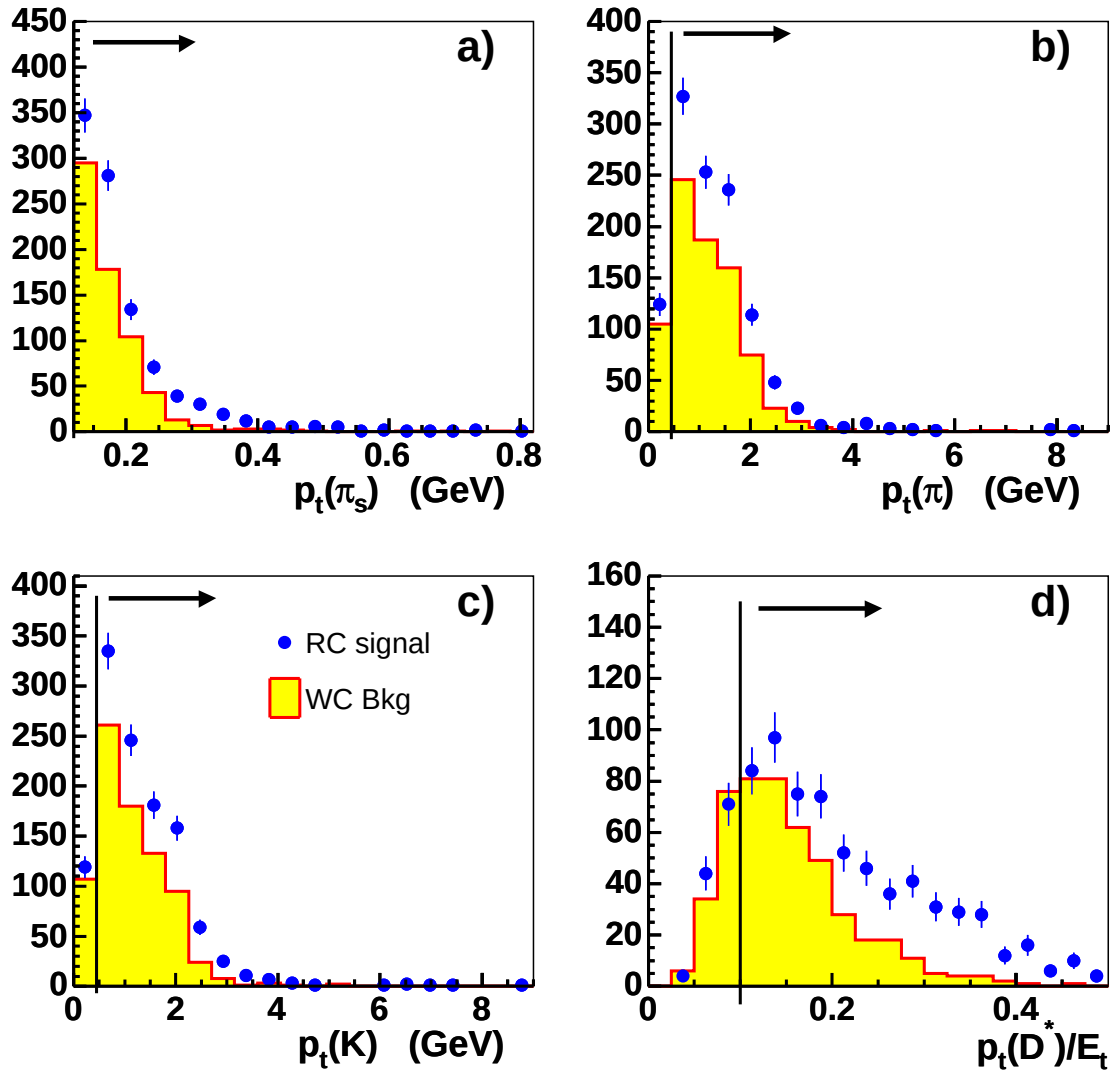

Figure B.2: Distributions of variables which are relevant for the D^* reconstruction: a) $p_t(\pi_s)$, b) $p_t(\pi)$, c) $p_t(K)$ and d) $p_t(D^*)/E_t$. The RC signal is represented by points while the error bars indicate the statistical error. The shaded area is the WC background. The vertical lines and the arrows indicate the selection cuts which are applied on the corresponding variables to select the final D^* sample.

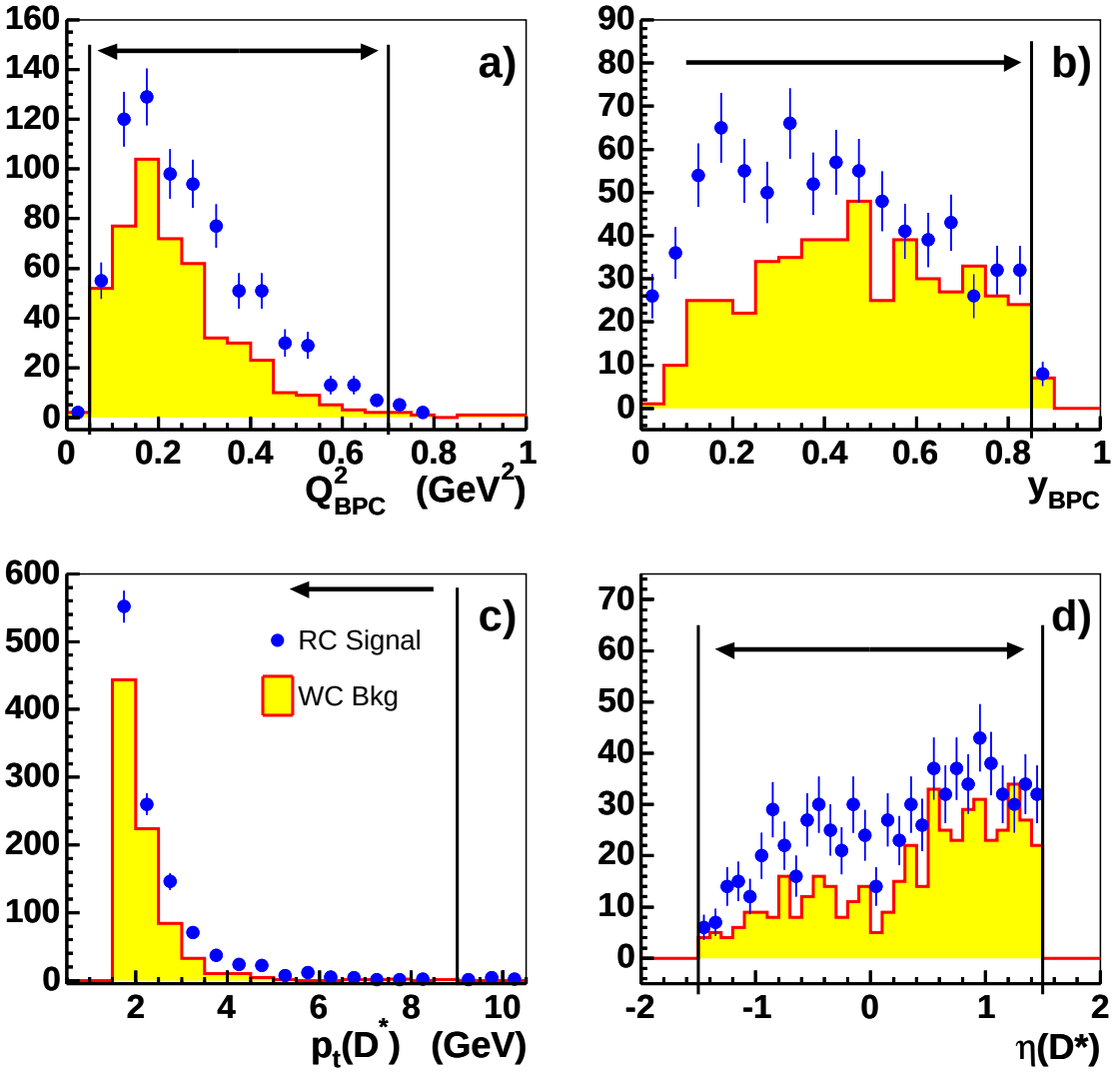

Figure B.3: Distribution of the kinematic event variables a) Q^2, b) y, c) $p_t(D^*)$, and $\eta(D^*)$ of the D^* production at low Q^2 analysis. The cuts define the kinematic region of the analysis. The RC signal is represented by points while the error bars indicate the statistical error. The shaded area is the WC background. The vertical lines and the arrows indicate the selection cuts which are applied on the corresponding variables to select the final D^* sample.

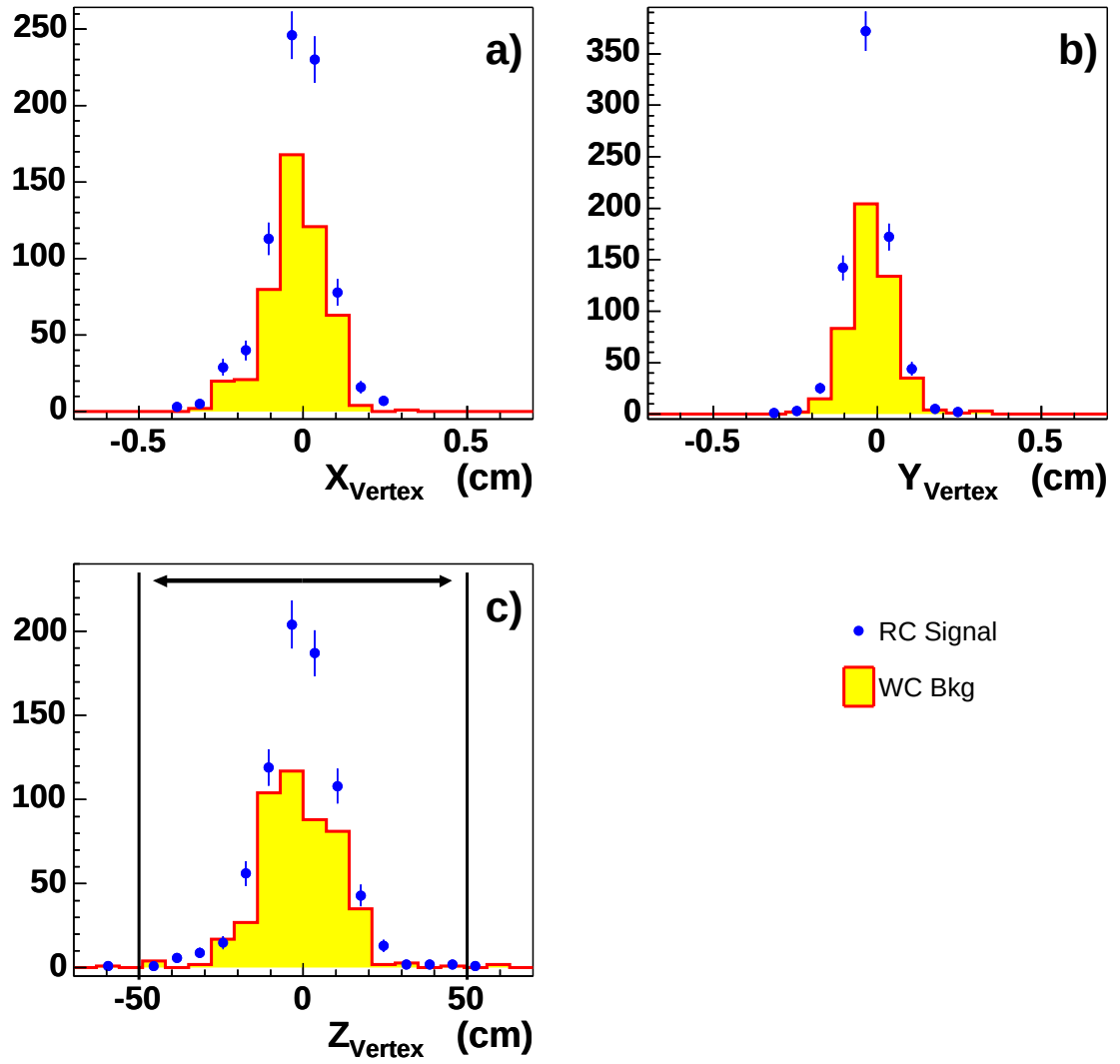

Figure B.4: Distributions of the reconstructed event vertex position in the 1998–2000 data sample. The numbers are given in the ZEUS coordinate system for the transverse directions a) X and b) Y and c) the longitudinal direction Z. Only Z is used to cut on for background reduction in the final D^* sample. The RC signal is represented by points while the error bars indicate the statistical error. The shaded is the WC background. The vertical lines and the arrows indicate the selection cuts which are applied on the corresponding variables in the final sample.

Appendix C

HERWIG MC $\Delta M(D^*)$ Fits

The ΔM distribution of the MC signal samples are fit using an unbinned likelihood method as described in Section 6.7. The only difference from the fit of the ΔM distribution of the data sample is that the initial fit parameters a_3 and a_4 are set to 0.01 which parametrise an almost flat and very low combinatoric background. This is needed because the MC is a pure signal MC and the combinations from combinatoric background are much reduced. The result of the fit for the full visible region of the BPC is shown in Fig. C.1. The results of the fits in the bins of the differential analysis are presented in Fig. C.2 and Fig. C.3. The number of D^* extracted by these fits in order to calculate the acceptance is tabulated in Section 6.7.

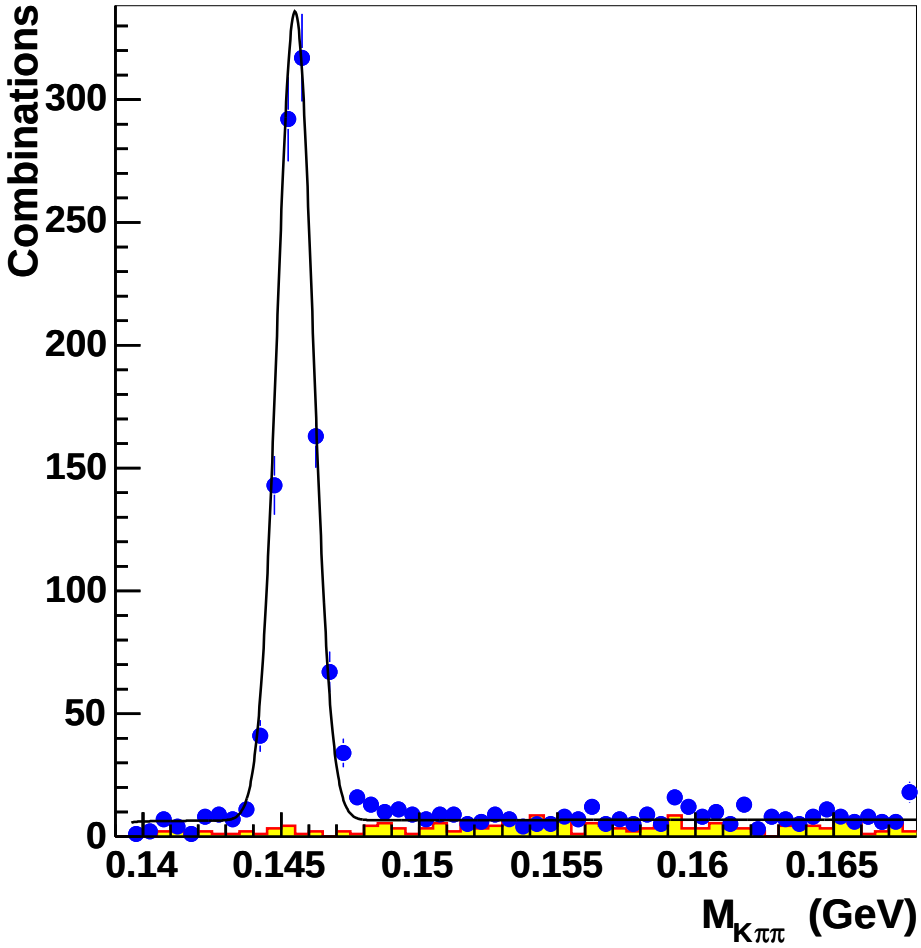

Figure C.1: The ΔM distribution for the total visible region of the HERWIG signal MC sample as described in Section 6.4. The distribution is fitted using an unbinned likelihood fit of a Gaussian signal function and a background function (see Section 6.7). The points represent the data with statistical errors, the shaded area is the background from combination of like-sign charged tracks to a D^0 candidate (WC). The number of D^* yielded by the fit is $N_{tot}^{MC}(D^*) = 1069 \pm 29$

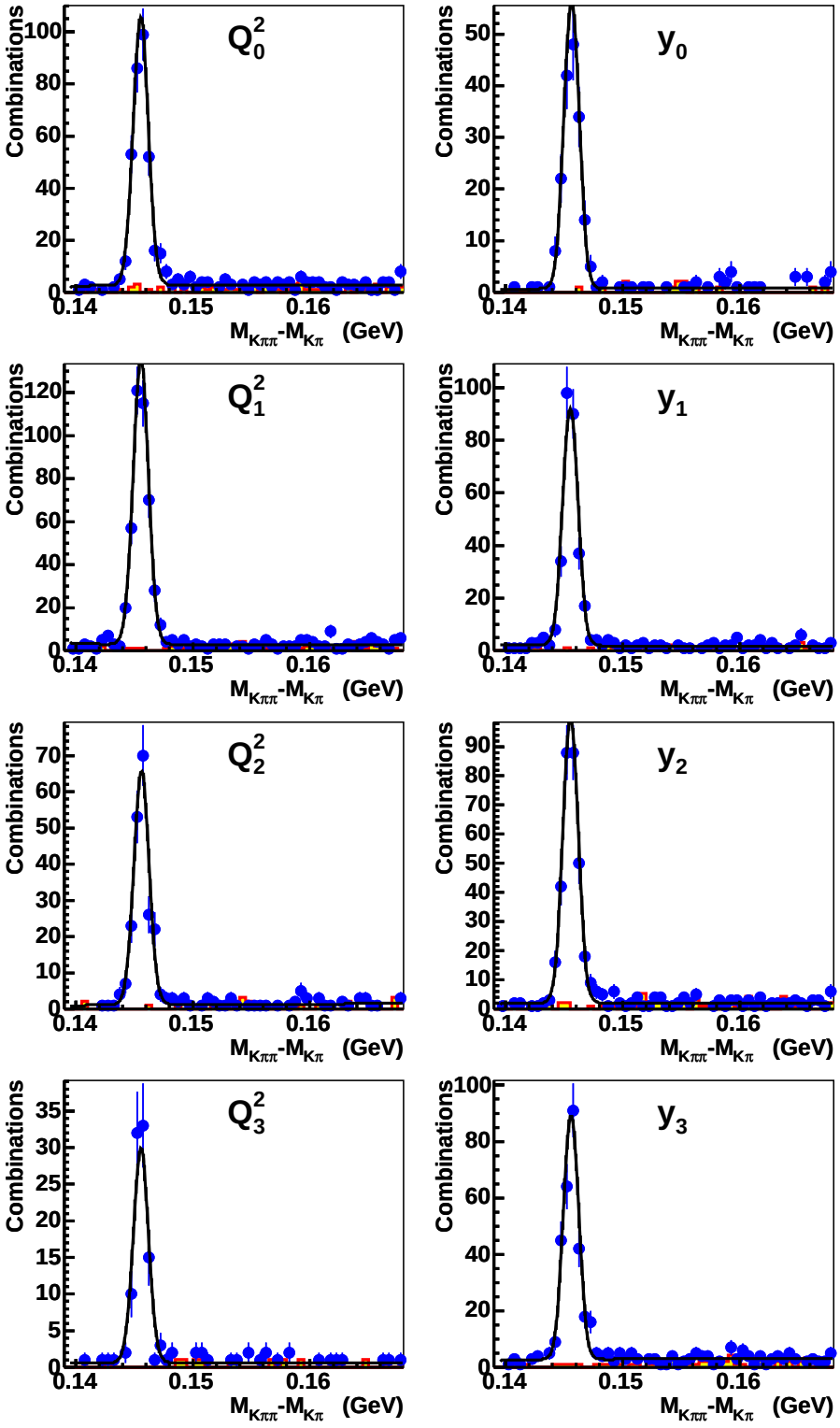

Figure C.2: The ΔM distribution for the differential analysis in each Q^2 and y bin of the HERWIG signal MC sample. The number of D^* is extracted in every bin by an unbinned likelihood fit of a Gaussian signal + a background function (see Section 6.7). MC is represented by points, the shaded area is the WC background.

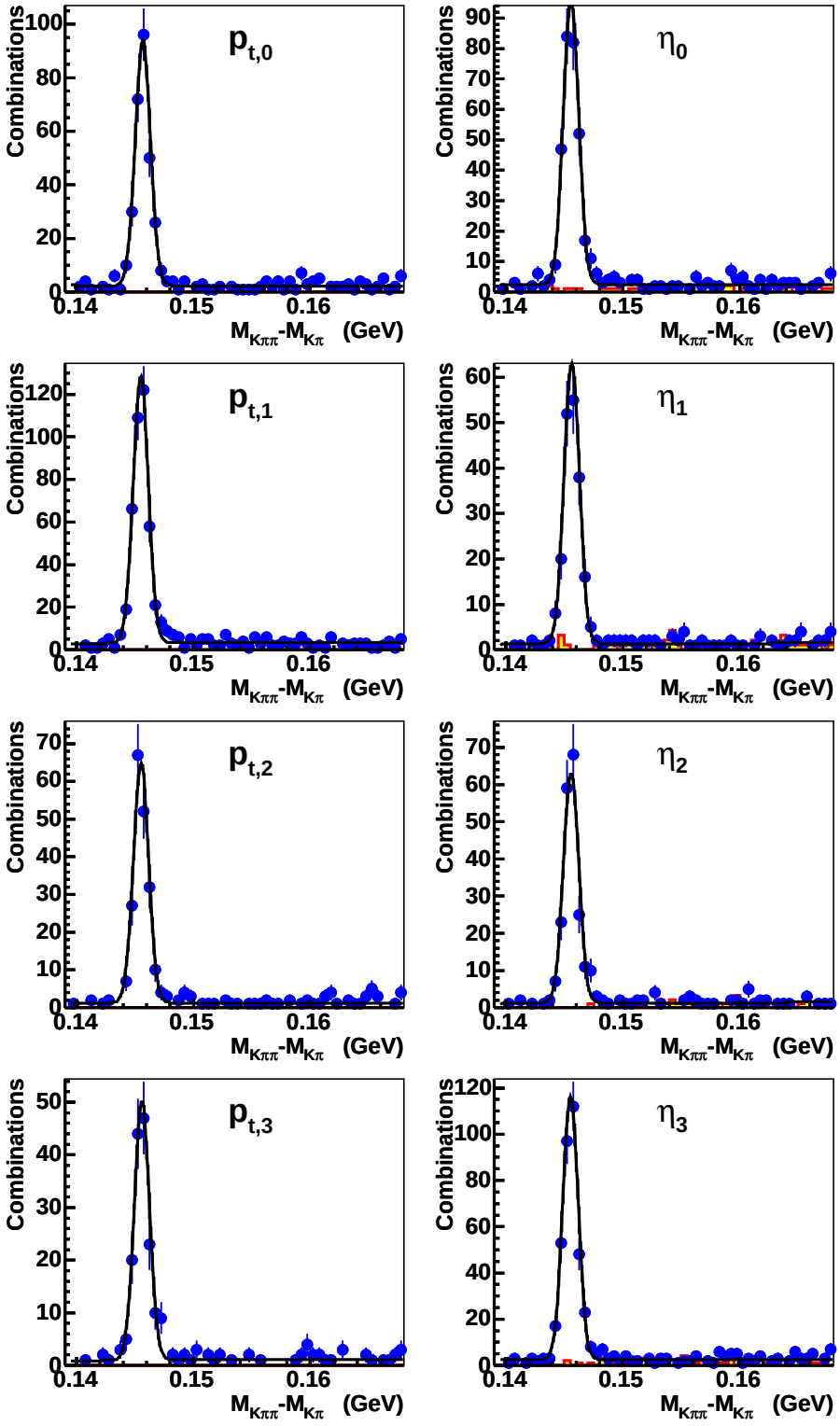

Figure C.3: The ΔM distribution for the differential analysis in each $p_t(D^*)$ and $\eta(D^*)$ bin of the HERWIG signal MC sample. The number of D^* is extracted in every bin an unbinned likelihood fit of a Gaussian signal + a background function (see Section 6.7). MC is represented by points, the shaded area is the WC background.

Appendix D

Geometrical BPC Acceptance

The acceptance of the BPC (Section 6.7.2) is the product of two independent acceptances: the acceptance given by the D^* reconstruction method, which uses CTD tracking information and depends on the CTD acceptance, and the BPC acceptance which is given by the BPC geometry.

The dependency of the acceptance on the D^* reconstruction method affects mainly the $p_t(D^*)$ and $\eta(D^*)$. In order to reduce this effect the analysis cuts are chosen well within the acceptance region of the CTD (Section 6.6).

Of special interest for this analysis is the Q^2 and y dependency of the BPC acceptance. They depend on the special geometry and position of the BPC. Therefore in the following the Q^2 dependency will be calculated explicitly and compared to the measured acceptance.

For the electron scattering angle Θ' one can write

$$\tan\Theta' = \frac{\sqrt{x^2+y^2}}{f} \tag{D.1}$$

with x- and y-position of the electron on the BPC front face and $f = 273\,\text{cm}$, the Z-distance of the BPC front face to the nominal vertex in the ZEUS coordinate system. From Fig. D.1 one obtains the relation

$$\alpha = \arctan\frac{y}{x} = \frac{\Delta\phi}{2} \tag{D.2}$$

and

$$\cos\alpha = x/\sqrt{x^2+y^2}\ . \tag{D.3}$$

The dependency of α on Q^2 can be expressed in the following way:

$$\alpha(Q^2) = \frac{\Delta\phi}{2\pi} = \frac{2\alpha}{2\pi} = \frac{1}{\pi}\arctan\frac{x}{y} \tag{D.4}$$

where x and y are depend implicitly on Q^2.

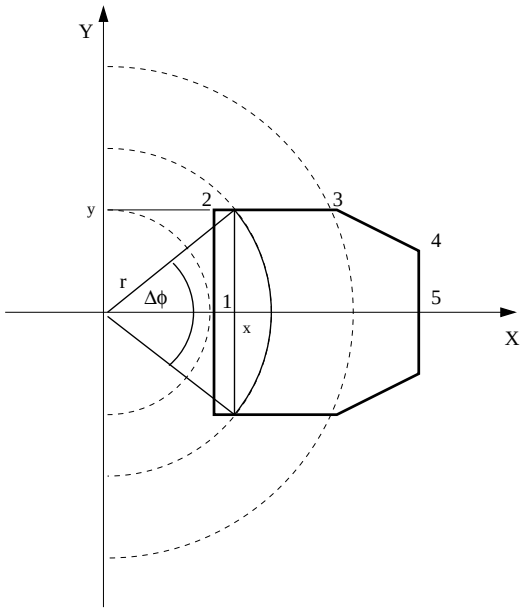

Figure D.1: Schematical view on the front face of the BPC. The numbers label the edges of the BPC front face which are defined in Tab. D.1. The dashed lines are lines of equal Q^2 or Θ' (under the assumption of fixed E' and the simplification of a symmetric front face w.r.t. the X-axis).

Edge number i	x_i/[cm]	y_i/[cm]
1	5.0	–
2	5.0	3.1 (-2.9)
3	8.5	3.1 (-2.9)
4	10.0	1.8 (-1.6)
5	10.0	–

Table D.1: X- and Y-positions of the edges of the BPC front face used in the geometrical calculation of Q^2-dependence of the acceptance. Values in brackets refer to the lower edge of the BPC front face.

Eqn. 2.2 is transformed then to an equation depending on the variables x, y and f:

$$\begin{aligned} Q^2 &= 2EE'\,(1-\cos\Theta') \\ &= 2EE'\left(1-\cos\left(\arctan\left(\sqrt{(x^2+y^2)/f}\right)\right)\right) \\ &= 2EE'\left(1-f/(\sqrt{f^2+x^2+y^2}\right) \\ &= 2EE'\left(1-f/(\sqrt{f^2+r^2}\right) \\ &= 2EE'\left(1-1/(\sqrt{1+r^2/f^2}\right) \end{aligned}$$

Using this equation we can evaluate the Q^2-dependence of the geometrical acceptance for the different edges of the BPC front face as labelled in Fig. D.1:

$$\begin{aligned} Q_1^2 &= 2EE'\left(1-1/(\sqrt{1+x_1^2/f^2}\right) \\ Q_2^2 &= 2EE'\left(1-1/(\sqrt{1+(x_1^2+y_2^2)/f^2}\right) \\ Q_3^2 &= 2EE'\left(1-1/(\sqrt{1+(x_3^2+y_2^2)/f^2}\right) \\ Q_4^2 &= 2EE'\left(1-1/(\sqrt{1+(x_4^2+y_4^2)/f^2}\right) \\ Q_5^2 &= 2EE'\left(1-1/(\sqrt{1+(x_5^2)/f^2}\right) \end{aligned}$$

where x_i and y_i denotes the coordinates of the edges of the BPC front face. These positions can be found in Tab. D.1. In order to calculate the Q^2 dependence of the acceptance one can use Eqn. D.4. As an example, this is done for the area between 1 and 2:

$$\alpha(Q^2) = \frac{1}{\pi}\arctan\left(\sqrt{r^2-a^2}/a\right) = \frac{1}{\pi}\arctan\sqrt{(r/a)^2-1}$$

$$r^2 = f^2 \left(\frac{1}{\left(1 - \frac{Q^2}{2EE'}\right)^2} - 1 \right)$$

$$\alpha(Q^2) = \frac{1}{\pi} \arctan \sqrt{\frac{f^2}{a^2} \left(\frac{1}{1 - \left(\frac{Q^2}{2EE'}\right)^2} - 1 \right) - 1}$$

This result and the results of the analogue calculations for the other areas between the labelled edges are shown in Fig. D.2.

Comparing Fig. D.2 with Fig. 6.16 we see that the shape of the measured $\alpha(Q^2)$ is very similar to the calculated $\alpha(Q^2)$. Thus the main contribution to the variation of the acceptance as function of Q^2 is just the BPC geometry.

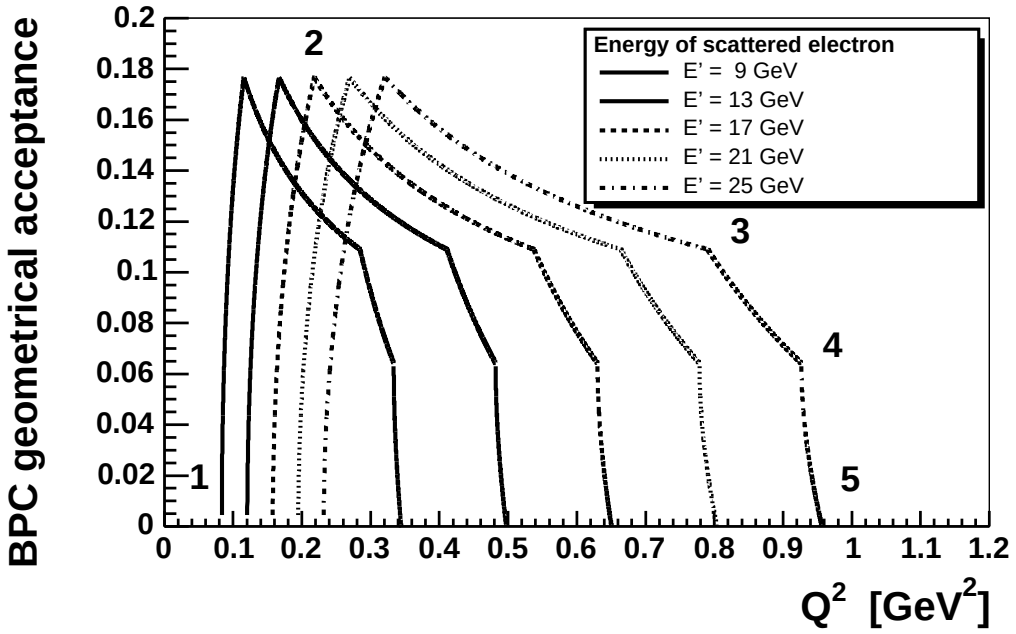

Figure D.2: Geometrical Q^2-dependence of the BPC acceptance for different energies E' of the scattered electron. The numbers indicate the edges of the BPC as used in the calculation.

Appendix E

HVQDIS Parameters

The HVQDIS NLO calculations for the central values are performed using the following configuration file:

```
2               ! 0:LO  1:NLO CORRECTIONS ONLY (NO LO)  2:FULL NLO RESULT
11              ! RENORMALIZATION SCALE (SEE SUBROUTINE MSCALE FOR DEFINITIONS)
11              ! FACTORIZATION   SCALE (SEE SUBROUTINE MSCALE FOR DEFINITIONS)
10              ! 1: CTEQ4F3  2: CTEQ5F3  3: GRV94  4: GRV98 10:ZEUS NLO pdf
50000           ! NUMBER OF VEGAS POINTS FOR LO
20              ! NUMBER OF VEGAS ITERATIONS FOR LO
1000000         ! NUMBER OF VEGAS POINTS FOR NLO
10              ! NUMBER OF VEGAS ITERATIONS FOR NLO
1               ! 1: CHARM 2: BOTTOM
1.35D0          ! QUARK MASS
920D0           ! ENERGY OF PROTON
27.5D0          ! ENERGY OF INCIDENT ELECTRON
0.05D0          ! Q2 MIN
0.7D0           ! Q2 MAX
0.D0            ! XBJ MIN
1.D0            ! XBJ MAX
0.02D0          ! Y MIN
0.85D0          ! Y MAX
1.5D0           ! |ETA| MAX
1.5D0           ! PT MIN
9.D0            ! PT MAX
1               ! 0: NO FRAGMENTATION  1: PETERSON FRAGMENTATION
0               ! 0: NO SL DECAY  1: SL DECAY (ONLY WITH IFRAG=1)
0.035D0         ! EPSION FOR PETERSON FRAGMENTATION
0.235D0         ! HADRONIZATION FRACTION (ONLY USED WHEN FRAGMENTING)
2.01D0          ! MASS OF HEAVY HADRON
```

Danksagung

Ich möchte allen herzlichst Danken, die mich während der Arbeit an meiner Promotion unterstützt und mir geholfen haben.

Mein besonderer Dank gilt meinem Doktorvater Prof. Ian Brock, der mir immer mit Rat und Tat zur Seite stand. Ich danke auch für die sehr angenehme Atmosphäre unter der diese Arbeit in der ZEUS-Gruppe der Uni-Bonn entstanden ist und die Prof. Brock, Prof. Paul und Prof. Hilger zu verdanken ist.

Ich danke meinen Kollegen und Ex-Kollegen aus der ZEUS-Gruppe, von denen ich namentlich besonders Joachim Tandler, Kai Voss, Oliver Kind, Holger Wessoleck, Henning Schnurbusch und Roger Renner erwähnen möchte. Sie haben meine vielen Fragen – nicht immer physikalischer Natur – gerne diskutiert und beantwortet und darüber hinaus auch manchen schönen Abend in Hamburg oder Bonn mit mir verbracht.

I am very grateful for the opportunity to work together with excellent international physicist at DESY in the heavy flavour group of ZEUS. I received kind and strong support especially from Richard Hall-Wilton and Sergey Fourletov and many other member of the group. I would also like to thank all other members of ZEUS and DESY, who provided the infrastructure and knowledge making this analysis possible in the first place.

Mein besonders herzlicher Dank gilt weiterhin allen Personen außerhalb meiner Arbeitsgruppe, die dieser Arbeit auf mehr oder weniger direkte Art und Weise ihre individuelle Prägung verliehen haben.

An erster Stelle möchte ich dabei meine Familie nennen, d.h. meine Mutter und meinen Vater, meine Geschwister Brigitte und Uwe und ihren Familien und vor allem meine liebe Ehefrau Karoline und meine Kinder Lilith und Ben. Ohne die Unterstützung und das Vertrauen meiner Eltern hätte es diese Arbeit nie gegeben. Meine Frau Karoline hat mich in den letzten Jahren durch die Höhen und Tiefen begleitet, die während des Fortschritts der Arbeit auftraten und dabei oft mit unter dem Promotionsstress zu leiden gehabt. Und in diesem Sinne möchte ich auch meinen Kindern danken, die es geschafft haben, mich vom Promotionsalltag abzulenken und dadurch neue Kraft zu gewinnen.

Last but not least geht mein herzlicher Dank an alle Freunde und Bekannten, die dazu beitragen haben, einen entspannten Ausgleich zwischen Promotion und den anderen interessanten Dingen des Lebens zu schaffen.

References

[1] M. Gell-Mann, Phys. Lett. **8**, 214 (1964).

[2] G. Zweig, Preprint CERN-8182/TH. 401, CERN-8419/TH. 402, 1964.

[3] F. Halzen and A.D. Martin, *Quarks and Leptons: An Introductory Course in Modern Particle Physics*. John Wiley & Sons, Inc, 1984.

[4] J.D. Bjorken, Phys. Rev. **179**, 1547 (1969).

[5] J. C. Collins, D. E. Soper and G. Sterman, Nucl. Phys. **B 261**, 104 (1985).

[6] G. Altarelli and G. Parisi, Nucl. Phys. **B 126**, 298 (1977).

[7] Yu.L. Dokshitzer, Sov. Phys. JETP **46**, 641 (1977).

[8] V.N. Gribov and L.N. Lipatov, Sov. J. Nucl. Phys. **15**, 438 (1972).

[9] ZEUS Coll., S. Chekanov et al., Phys. Rev. **D67**, 012007 (2003).

[10] A.D. Martin et al., Eur. Phys. J. **C23**, 73 (2002).

[11] CTEQ Coll., J. Pumplin et al., JHEP **07**, 012 (2002).

[12] ZEUS Coll., S. Chekanov et al., Eur. Phys. J. **C 21**, 443 (2001).

[13] CTEQ Coll., H.L. Lai et al., Eur. Phys. J. **C 12**, 375 (2000).

[14] L.N. Hand, Phys. Rev. **129**, 1834 (1963).

[15] J.J. Sakurai, Phys. Rev. Lett. **22**, 981 (1969).

[16] P.D.B. Collins, *An Introduction to Regge Theory and High Energy Physics*. Cambridge University Press, 1977.

[17] V. Barone and E. Predazzi, *High-Energy Particle Diffraction*. Springer, 2001.

[18] J.J. Sakurai and D. Schildknecht, Phys. Lett. **B 40**, 121 (1972).

[19] Geoffrey F. Chew and Steven C. Frautschi, Phys. Rev. **8**, 41 (1961).

[20] Bonino, R. and others, Phys. Lett. **B211**, 239 (1988).

[21] Brandt, A. and others, Phys. Lett. **B297**, 417 (1992).

[22] ZEUS Coll., M. Derrick et al., Phys. Lett. **B 315**, 481 (1993).

[23] H1 Coll., T. Ahmed et al., Nucl. Phys. **B 429**, 477 (1994).

[24] ZEUS Coll., J. Breitweg et al., Phys. Lett. **B 487**, 53 (2000).

[25] Particle Data Group, K. Hagiwara et al., Phys. Rev. **D 66**, 10001 (2002).

[26] Song, X., Phys. Rev. **D65** (2002).

[27] F.I. Olness, Preprint hep-ph/9906295, 1999.

[28] ZEUS Coll., J. Breitweg et al., Phys. Lett. **B 407**, 402 (1997).

[29] ZEUS Coll., J. Breitweg et al., Eur. Phys. J. **C 12**, 35 (2000).

[30] H1 Coll., C. Adloff et al., Z. Phys. **C 72**, 593 (1996).

[31] H1 Coll., C. Adloff et al., Nucl. Phys. **B 545**, 21 (1999).

[32] M. Buza et al., Phys. Lett. **B 411**, 211 (1997).

[33] C. Amelung, *Measurement of the Proton Structure Function F_2 at Very Low Q^2 at HERA*. Ph.D. Thesis, Universität Bonn, Bonn, (Germany), Report BONN-IR-99-14, DESY-THESIS-2000-002, 1999.

[34] B. W. Harris and J. Smith, Phys. Rev. **D**, 2806 (1998).

[35] C. Peterson et al., Phys. Rev. **D 27**, 105 (1983).

[36] ARGUS Coll., H. Albrecht et al., Z. Phys. **C 52**, 353 (1991).

[37] CLEO Coll., D. Bortoletto et al., Phys. Rev. **37**, 1719 (1988).

[38] L. Gladilin, Preprint hep-ex/9912064, 1999.

[39] OPAL Coll., R. Akers et al., Z. Phys. **C 67**, 27 (1995).

[40] Particle Data Group, K. Hagiwara et al., Phys. Rev. **D 66**, 010001 (2002).

[41] ZEUS Coll., S. Chekanov et al., *Proceedings of the 11th International Workshop Deep Inelastic Scattering and QCD*. World Scientific, Singapore (2003).

[42] G. Marchesini et al., Comp. Phys. Comm. **67**, 465 (1992).

[43] G. Corcella et al., Journal of High Energy Phys. **01**, 010 (2001).

[44] B. R. Webber, Nucl. Phys. **B 238**, 492 (1984).

[45] H. Jung, Comp. Phys. Comm. **86**, 147 (1995).

[46] A. Kwiatkowski, H. Spiesberger and H.-J. Möhring, Comp. Phys. Comm. **69**, 155 (1992). Also in *Proc. Workshop Physics at HERA*, 1991, DESY, Hamburg.

[47] Sjostrand, Torbjorn, Comput. Phys. Commun. **82**, 74 (1994).

[48] G. Ingelman, A. Edin and J. Rathsman, Comp. Phys. Comm. **101**, 108 (1997).

[49] ZEUS Coll., S. Chekanov et al., Phys. Rev. **D69** (2004).

[50] B. W. Harris and J. Smith, ITP-SB **08** (1995).

[51] ZEUS Coll., S. Chekanov et al., Phys. Rev. **D 67**, 012007 (2003).

[52] M. Wing. Private communication.

[53] R. Brun et al., GEANT3, Technical Report CERN-DD/EE/84-1, CERN, 1987.

[54] HERA, *A Proposal for a Large Electron-Proton Colliding Beam Facility at DESY*. DESY-HERA-81/10, 1981.

[55] HERMES Coll., *Technical Design Report*, 1993.

[56] HERA-B Coll., *Technical Design Report*. DESY-PRC 95/01, 1995.

[57] HERA-B Coll., *Report on Status and Prospects*. DESY-PRC 00/04, 2000.

[58] H1 Coll., I. Abt et al., Nucl. Inst. Meth. **A 386**, 310 (1997).

[59] U. Schneekloth (ed.), Preprint HERA-98-05, DESY, 1998, available on `http://www.desy.de/~ahluwali/HERA-98-05`.

[60] B. Foster, *ZEUS at HERA II*. Hep-ex/0107066, 2001.

[61] ZEUS Coll., U. Holm (ed.), *The ZEUS Detector*. Status Report (unpublished), DESY (1993), available on `http://www-zeus.desy.de/bluebook/bluebook.html`.

[62] I. Kudla et al., Nucl. Inst. Meth. **A 300**, 480 (1991).

[63] H. Abramowicz et al., Nucl. Inst. Meth. **A 313**, 126 (1992).

[64] G. Abbiendi et al., Nucl. Inst. Meth. **A 333**, 342 (1993).

[65] ZEUS Coll., M. Derrick et al., Z. Phys. **C 73**, 253 (1997).

[66] ZEUS Coll., FNC group, S. Bhadra et al., Nucl. Inst. Meth. **A 394**, 121 (1997).

[67] N. Harnew et al., Nucl. Inst. Meth. **A 279**, 290 (1989);
B. Foster et al., Nucl. Phys. Proc. Suppl. **B 32**, 181 (1993);
B. Foster et al., Nucl. Inst. Meth. **A 338**, 254 (1994).

[68] R. Hall-Wilton et al., *The CTD Tracking Resolution* (unpublished). ZEUS-99-024, internal ZEUS-note, 1999.

[69] M. Derrick et al., Nucl. Inst. Meth. **A 309**, 77 (1991);
A. Andresen et al., Nucl. Inst. Meth. **A 309**, 101 (1991);
A. Caldwell et al., Nucl. Inst. Meth. **A 321**, 356 (1992);
A. Bernstein et al., Nucl. Inst. Meth. **A 336**, 23 (1993).

[70] ZEUS Luminosity Group, J. Andruszków et al., Preprint DESY-01-041, 2001. Reference **desy-01-041** is outdated. Use **acpp:b32:2025** instead.

[71] ZEUS Coll., J. Breitweg et al., Phys. Lett. **B 407**, 432 (1997).

[72] B. Surrow, *Measurement of the Proton Structure Function F_2 at Low Q^2 and Very Low x with the ZEUS Beam Pipe Calorimeter at HERA*. Ph.D. Thesis, Universität Hamburg, Germany, Report DESY-THESIS-1998-004, 1998.

[73] R. Deffner, *Measurement of the Proton Structure Function F_2 at HERA Using the 1996 and 1997 ZEUS Data*. Ph.D. Thesis, University of Bonn, 1999, available on `http:///www-zeus.physik.uni-bonn.de/german/phd.html`.

[74] U. Fricke, *Precision Measurement of the Proton Structure Function F_2 at Low Q^2 and Very Low x at HERA*. Ph.D. Thesis, Universität Hamburg, Hamburg, Germany, Report DESY-THESIS-1999-043, 1999.

[75] ZEUS Coll., *BPRECON* (unpublished). ZEUS-98-081, internal ZEUS-note, 1998.

[76] J. Tandler, *Exclusive Production of J/Ψ Mesons in the ZEUS Detector*. Ph.D. Thesis, Universität Bonn, Germany, Report BONN-IR-03-06, 2003.

[77] P. Billoir and S. Qian, Nucl. Inst. Meth. **A 311** (1992).

[78] Richard Hall-Wilton, *Diffractive and Non-Diffractive Charm Production in Deep Inelastic Scattering at HERA*. Thesis, University of Bristol, Report RAL-TH-1999-013, 1999.

[79] Particle Data Group, C. Caso et al., Eur. Phys. J. **C3**, 1 (1998).

[80] ZEUS Coll., *A Systematic Method for Unbinned Fitting and Statistical Analysis* (unpublished). ZEUS-97-096, internal ZEUS-note, 1997.

[81] L. Gladilin. Private communication.